

Production of Λ Hyperons at Forward Rapidity
in d+Au Collisions at $\sqrt{s_{NN}} = 200$ GeV

Frank Simon

Max-Planck-Institut für Physik, Munich, Germany

January 2005

Technische Universität München

MAX-PLANCK-INSTITUT FÜR PHYSIK
WERNER-HEISENBERG-INSTITUT

Production of Λ Hyperons at Forward Rapidity
in d+Au Collisions at $\sqrt{s_{NN}} = 200$ GeV

Frank Simon

Vollständiger Abdruck der von der Fakultät für Physik
der Technischen Universität München zur Erlangung
des akademischen Grades eines Doktors der Naturwissenschaften
genehmigten Dissertation.

Vorsitzender: Univ.-Prof. Dr. Manfred Lindner

Prüfer der Dissertation:

1. Hon.-Prof. Dr. Norbert Schmitz
2. Univ.-Prof. Dr. Stephan Paul (schriftliche Beurteilung)
Univ.-Prof. Dr. Reiner Krücken (mündliche Prüfung)

Die Dissertation wurde am 11.01.2005 bei der
Technischen Universität München eingereicht und durch die
Fakultät für Physik am 17.02.2005 angenommen.

Abstract

The radial–drift forward TPCs of the STAR experiment at the Relativistic Heavy Ion Collider are used to reconstruct Λ and $\bar{\Lambda}$ hyperons produced at forward and backward rapidity in d+Au collisions at $\sqrt{s_{NN}} = 200$ GeV. For the efficiency corrections a simulation framework that merges simulated particle tracks with real data was developed. The resulting Λ and $\bar{\Lambda}$ particle yields are used to study baryon transport in the asymmetric collision system. The comparison to a variety of model calculations demonstrates that stopping on the deuteron side is well described by a superposition of individual nucleon–nucleon reactions while on the gold side, the inclusion of initial or final state nuclear effects is necessary. The rapidity loss of baryons on the deuteron side shows that the nuclear stopping power in d+Au collisions is larger than in Au+Au reactions.

Zusammenfassung

Mit Hilfe der Vorwärts-Spuredriftkammern des STAR Experimentes am Relativistic Heavy Ion Collider werden Λ und $\bar{\Lambda}$ Hyperonen bei hohen Rapiditäten in d+Au Kollisionen bei $\sqrt{s_{NN}} = 200$ GeV rekonstruiert. Zur Durchführung der Effizienzkorrekturen wurde ein Simulationsprogramm entwickelt, das simulierte Teilchenspuren in echte Ereignisse einbettet. Die damit gewonnenen Λ und $\bar{\Lambda}$ Teilchendichten werden zur Untersuchung des Baryonentransports in dem asymmetrischen Kollisionssystem genutzt. Der Vergleich mit verschiedenen Modellrechnungen zeigt, dass der Baryonentransport auf der Deuteron-Seite gut durch eine Überlagerung einzelner Nukleon–Nukleon Reaktionen beschrieben wird, während auf der Gold-Seite die Berücksichtigung von Kerneffekten notwendig ist. Der Rapiditätsverlust von Baryonen auf der Deuteron-Seite zeigt, dass das Bremsvermögen der Kernmaterie in d+Au Kollisionen grösser ist als in Au+Au Reaktionen.

Contents

| | | |
|----------|--|-----------|
| 1 | Introduction | 1 |
| 2 | Nuclear Matter under Extreme Conditions | 3 |
| 2.1 | Early Universe and Neutron Stars | 3 |
| 2.2 | The Strong Interaction: Confinement and Asymptotic Freedom | 4 |
| 2.3 | The Phase Diagram of Hadronic Matter | 5 |
| 2.4 | Relativistic Heavy Ion Collisions | 6 |
| 2.4.1 | Evolution of the Collision | 6 |
| 2.4.2 | Stopping and Baryon Transport | 7 |
| 2.4.3 | Experimental Observables | 8 |
| 3 | Experimental Setup | 9 |
| 3.1 | The Accelerator Complex | 9 |
| 3.1.1 | Heavy Ion Experiments | 11 |
| 3.1.2 | RHIC performance in 2003 | 12 |
| 3.2 | The STAR Experiment | 12 |
| 3.2.1 | Tracking Detectors | 12 |
| 3.2.2 | Calorimeters | 14 |
| 3.2.3 | Trigger Detectors and Data Acquisition | 14 |
| 3.3 | The STAR Forward TPCs | 15 |
| 3.3.1 | The Principle of Time Projection Chambers | 15 |
| 3.3.2 | Design Considerations | 16 |
| 3.3.3 | Field Cage and Sensitive Volume | 17 |
| 3.3.4 | Detector Readout | 18 |
| 3.3.5 | Calibration and Reconstruction | 19 |
| 3.4 | d+Au Collisions | 20 |
| 3.4.1 | Properties of the Beam Nuclei | 21 |
| 3.4.2 | Charged Particles | 22 |
| 3.4.3 | d+Au Collisions at STAR | 23 |
| 3.4.4 | Models | 26 |
| 3.4.5 | Model Results | 28 |
| 4 | Detector Simulations | 31 |

| | | |
|----------|--|-----------|
| 4.1 | Pure Simulations | 32 |
| 4.1.1 | HIJING Simulations | 32 |
| 4.2 | Embedding | 33 |
| 4.2.1 | Gain Tables | 33 |
| 4.2.2 | The Embedding Procedure | 34 |
| 4.2.3 | Comparison to Data | 35 |
| 4.3 | Tracking Efficiency and Momentum Resolution | 37 |
| 4.3.1 | Matching of Reconstruction and Simulation | 37 |
| 4.3.2 | Tracking Efficiency | 38 |
| 4.3.3 | Momentum Resolution | 39 |
| 4.4 | Limitations | 40 |
| 5 | Data Analysis and Corrections | 43 |
| 5.1 | Properties of Λ Particles and their Decay Signatures | 43 |
| 5.2 | Analysis Method | 44 |
| 5.2.1 | Analysis Cuts | 45 |
| 5.2.2 | Background Subtraction | 49 |
| 5.3 | Expected Performance | 50 |
| 5.4 | Acceptance | 50 |
| 5.5 | Invariant Mass Distributions | 51 |
| 5.6 | Corrections | 53 |
| 5.6.1 | Efficiency | 54 |
| 5.6.2 | Feeddown | 55 |
| 5.7 | Mean Life | 58 |
| 5.8 | K_S^0 Analysis | 59 |
| 5.8.1 | Kaon Properties and Decay | 59 |
| 5.8.2 | Analysis and Cuts | 60 |
| 5.8.3 | Acceptance | 61 |
| 5.8.4 | Invariant Mass | 62 |
| 5.8.5 | Mean Life | 63 |
| 5.8.6 | K_S^0 yield | 63 |
| 6 | Results on Λ Hyperons | 67 |
| 6.1 | Particle Yields | 67 |
| 6.1.1 | Yield and Temperature Determination | 68 |
| 6.1.2 | Minimum Bias Spectra | 69 |
| 6.1.3 | Systematic Errors | 70 |
| 6.1.4 | Minimum bias yields | 71 |
| 6.2 | Temperature Parameter | 72 |
| 6.3 | $\bar{\Lambda}/\Lambda$ Ratio | 73 |
| 6.4 | Centrality Dependence | 74 |
| 6.5 | ZDC Neutron Tagged Events | 77 |

| | |
|--|------------|
| 7 Discussion | 79 |
| 7.1 The Influence of the Medium | 79 |
| 7.2 Strangeness Production | 82 |
| 7.2.1 Centrality Dependence of the Particle Yields | 82 |
| 7.2.2 Centrality Dependence of the Temperature Parameter | 84 |
| 7.3 Baryon Transport and Stopping | 86 |
| 7.3.1 Model Comparisons | 86 |
| 7.3.2 Mechanisms of Baryon Transport | 89 |
| 7.3.3 Rapidity Loss and Stopping | 90 |
| 8 Conclusion and Outlook | 97 |
| Appendix | |
| A Kinematic Variables | 99 |
| B The STAR Coordinate System | 101 |
| Bibliography | 102 |

List of Figures

| | | |
|------|---|----|
| 2.1 | Phase diagram of hadronic matter | 5 |
| 3.1 | The RHIC accelerator complex | 10 |
| 3.2 | The STAR detector at RHIC | 13 |
| 3.3 | Layout of the forward TPCs | 17 |
| 3.4 | Grids in the FTTPC | 19 |
| 3.5 | Illustration of a d+Au collision | 22 |
| 3.6 | $dN_{ch}/d\eta$ in d+Au by PHOBOS | 22 |
| 3.7 | Vertex distribution for d+Au minimum bias events | 23 |
| 3.8 | Impact parameter | 25 |
| 3.9 | Number of participants | 25 |
| 3.10 | TPC Reference Multiplicity | 26 |
| 3.11 | $dN_{ch}/d\eta$ in models | 29 |
| 4.1 | Flow chart of the FTTPC simulation chain | 32 |
| 4.2 | Cluster size in time and pad (r and φ) direction | 35 |
| 4.3 | Cluster charge in real data and embedding | 36 |
| 4.4 | Number of hits on track | 37 |
| 4.5 | Efficiency from embedding | 39 |
| 4.6 | Resolution of transverse momentum | 40 |
| 4.7 | DCA of simulated and real tracks | 41 |
| 5.1 | Simulated Λ decay | 44 |
| 5.2 | DCA of daughter particles of Λ decays | 45 |
| 5.3 | DCA of decay daughters at decay vertex | 46 |
| 5.4 | Distance of closest approach of reconstructed Λ to the primary vertex. | 46 |
| 5.5 | Opening Angle of decay daughters | 47 |
| 5.6 | Decay length of simulated Λ . Values which are rejected by the cut are shaded. | 48 |
| 5.7 | Illustration of cut parameters | 48 |
| 5.8 | Simulated Λ invariant mass | 50 |
| 5.9 | Rapidity resolution for Λ | 50 |
| 5.10 | Acceptance for Λ candidates. | 51 |

| | | |
|------|--|-----|
| 5.11 | Invariant mass distribution for Λ and $\bar{\Lambda}$ candidates | 52 |
| 5.12 | Background subtracted invariant mass plots for both FTPCs | 53 |
| 5.13 | Comparison of Λ candidate dca | 56 |
| 5.14 | Ξ^-/Λ and $\bar{\Xi}^+/\bar{\Lambda}$ ratios as a function of rapidity | 58 |
| 5.15 | Life time of Λ candidates in FTPC W | 59 |
| 5.16 | Acceptance for K_S^0 candidates | 61 |
| 5.17 | Invariant mass distribution of K_S^0 | 62 |
| 5.18 | Life time of K_S^0 candidates in FTPC West | 63 |
| 5.19 | m_t distribution of K_S^0 candidates | 64 |
| 5.20 | dN/dy of K_S^0 in d+Au minimum bias | 65 |
| | | |
| 6.1 | Λ and $\bar{\Lambda}$ spectra for d+Au minimum bias | 69 |
| 6.2 | Λ and $\bar{\Lambda}$ spectra for d+Au 40% – 100% | 74 |
| 6.3 | Λ and $\bar{\Lambda}$ spectra for d+Au 20% – 40% | 75 |
| 6.4 | Λ and $\bar{\Lambda}$ spectra for d+Au Top 20% | 75 |
| 6.5 | Invariant mass for ZDC neutron tag events | 78 |
| | | |
| 7.1 | Nuclear modification factor for d+Au and Au+Au at mid-rapidity | 80 |
| 7.2 | R_{cp} for Λ | 81 |
| 7.3 | Centrality dependence of Λ | 83 |
| 7.4 | Centrality dependence of $\bar{\Lambda}$ | 83 |
| 7.5 | Λ yield ratio | 84 |
| 7.6 | Temperature parameter of Λ and $\bar{\Lambda}$ | 85 |
| 7.7 | Λ particle yield dN/dy | 86 |
| 7.8 | $\bar{\Lambda}$ particle yield dN/dy | 87 |
| 7.9 | Net Λ yield dN/dy | 88 |
| 7.10 | $\bar{\Lambda}/\Lambda$ ratio | 89 |
| 7.11 | Net baryon yield with a pol6 fit in d+Au minimum bias events | 92 |
| 7.12 | Net baryon yield and pol6 fit as a function of centrality | 93 |
| | | |
| B.1 | The STAR coordinate system | 101 |

Chapter 1

Introduction

The primary goal of relativistic heavy ion collisions is the study of nuclear matter at extremely high temperatures and densities. Under these conditions a phase transition to a deconfined state of quarks and gluons, the Quark Gluon Plasma (QGP), is expected.

No individual discovery signatures of this state of matter are known today, so that only a combination of different experimental observables can lead to the proof of its existence. It is therefore crucial to study a variety of aspects of heavy ion collisions. In addition, a base of references that exhibit the effects introduced by the beam particles in the absence of a QGP has to be provided. This calls for the study of proton–nucleus or deuteron–nucleus collisions, in which no QGP is created but nuclear effects are present.

The Forward Time Projection Chambers (FTPCs) in the STAR experiment at the Relativistic Heavy Ion Collider (RHIC) open up the unique possibility to study the production of neutral strange particles at forward and backward rapidity. Strange-ness production plays a central role in heavy ion physics. Thus a comprehensive study of strange particles in d+Au collisions is of importance.

The measurement of forward and backward Λ and $\bar{\Lambda}$ production gives access to the study of baryon transport. The degree of stopping in the collision determines the amount of energy available for particle production and the creation of possible new states of matter. It is expected that nuclear effects and multiple collisions of reaction participants influence baryon transport. By exploiting the asymmetry of d+Au collisions, these contributions can be investigated. Baryon transport on the deuteron side is dominated by multiple collisions of the deuteron constituents with gold participants while on the gold side it is affected by nuclear effects.

This thesis presents the first measurement of Λ and $\bar{\Lambda}$ production at forward and backward ($y = \pm 2.75$) rapidity in d+Au collisions at an energy of $\sqrt{s_{NN}} = 200$ GeV at RHIC. The analysis procedure as well as the simulation tools developed to obtain

the necessary efficiency corrections are described. Corrected spectra for Λ and $\bar{\Lambda}$ in minimum bias events and three centrality classes are obtained on both sides of the collision. From these the net Λ yield ($\Lambda - \bar{\Lambda}$) is determined. The $\bar{\Lambda}/\Lambda$ ratio is calculated and clearly shows the asymmetry of the d+Au events.

The effects of the nuclear matter on particle production and a possible strangeness enhancement are studied with the centrality dependence of the particle yields. By comparing the measurements of the net Λ dN/dy and the $\bar{\Lambda}/\Lambda$ ratio as a function of rapidity to a wide range of model calculations the different contributions to baryon transport are investigated. Together with mid-rapidity measurements, the forward net Λ results are used to obtain an estimate of the mean rapidity loss of baryons on the deuteron side of the collision.

Chapter 2

Nuclear Matter under Extreme Conditions

The atomic nucleus has been the subject of experimental studies since its discovery in 1911, resulting in constant improvement of our understanding of the building blocks of matter and the forces that govern their behavior. It is now well established that the nucleus is made up of protons and neutrons, which in turn contain quarks, that are currently thought to represent the lowest layer in our hierarchical picture. The quarks interact via the exchange of gluons, the mediators of the strong force.

Free quarks are not observed, they always form strongly interacting particles called hadrons which are either baryons consisting of three valence quarks or mesons made up of one valence quark and one valence antiquark, in addition to the quark – antiquark pairs present in the sea. This observation is explained by a feature of the strong interaction called confinement that makes isolated quarks energetically prohibitive.

The nuclear matter that surrounds us is in its ground state at low temperatures and a density of $\sim 2.5 \times 10^{14}$ g/cm³, which corresponds to 0.16 nucleons per fm³. However in the early universe nuclear matter existed under very different conditions, and still might do so today in neutron stars.

2.1 Early Universe and Neutron Stars

In most current models, the universe is thought to have been created in a Big Bang approximately 15 billion years ago. As it expanded and cooled, matter underwent several phase transitions. About $1 \mu\text{s}$ after the Big Bang, the temperature was around 1 GeV. Matter is believed to have been a hot, dense state composed of free-roaming quarks and gluons, a state called the Quark Gluon Plasma (QGP). The

QGP of the early universe was characterized by low baryon density due to almost equal numbers of quarks and antiquarks.

Present neutron stars might represent another extreme of nuclear matter. They are formed when a heavy star has spent all its fusionable fuel and collapses under its own gravity. Due to the high pressure it becomes energetically favorable to absorb electrons in protons to create neutrons and neutrinos. The latter escape. Some models predict that this can result in cold matter at about 5 times the density of normal nuclear matter where the nucleons merge together and lose their identity.

2.2 The Strong Interaction: Confinement and Asymptotic Freedom

In addition to the electric charge, the quarks possess an additional charge called color. This charge of the strong interaction exists in three kinds, conventionally designated red, green and blue. The force between the quarks is mediated by massless particles called gluons that couple to the color charges. This is analogous to the photon that couples to the electric charge and mediates the electromagnetic force. However, contrary to the photon, gluons themselves carry color, and thus can also interact with each other.

This feature of the strong interaction leads to an increase of the interaction strength with distance. The potential between two quarks may therefore be written as

$$V(r) = -\frac{4\alpha_s}{3r} + kr, \quad (2.1)$$

where α_s is the strong coupling constant, k is a constant of the order of 1 GeV/fm and r is the separation of the quarks. Due to the linear term in equation 2.1, an infinite amount of energy is needed to separate two color charges. In practice, the field energy will lead to the creation of a quark – antiquark pair out of the vacuum to form two separate colorless objects. This is described as the phenomenon of confinement, as it is impossible to observe isolated color charges.

However, it is observed that the strong coupling constant α_s decreases with increasing momentum transfer, and thus with decreasing distance. Thus the force between color charges vanishes at small distances, a process called asymptotic freedom.

The discovery that non-abelian gauge theories can reproduce the experimentally observed asymptotic freedom of the strong interaction [1, 2] led to the formulation of a quantum field theory of the interaction called quantum chromodynamics (QCD). Since the coupling parameter α_s of the interaction is much smaller than unity only at small distances which correspond to interactions with large momentum transfer, only these processes can be computed perturbatively. In the soft regime at larger

distance scales perturbative QCD (pQCD) is not applicable. Here, calculations that solve the field equations on a four-dimensional euclidean lattice are used [3].

In an environment of high hadronic density, quarks will interact with other quarks belonging to different hadrons. In this process referred to as Debye screening the association of quarks to hadrons is lost, resulting in free movement of color charges within the volume of the high-density matter.

2.3 The Phase Diagram of Hadronic Matter

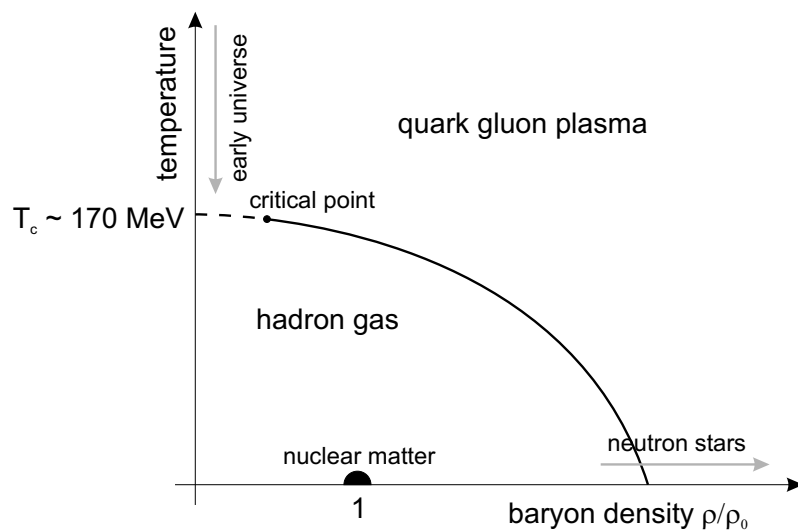


Figure 2.1: Simplified phase diagram of hadronic matter. Due to the finite quark masses, calculations predict the existence of a critical point where the phase transition changes from first order to a smooth crossover. From recent theoretical studies a number of distinct phases at high baryon density and low temperature are expected.

Figure 2.1 shows a schematic phase diagram of hadronic matter, where the temperature is plotted against the net baryon density divided by the density of normal nuclear matter. There are two distinct phases apart from nuclear matter in its ground state, namely a hadron gas of free hadrons, and the quark gluon plasma with deconfined quarks and gluons. Additional phases at high baryon density, such as color superconductors have been suggested. A detailed discussion of the nuclear phase diagram may be found in [4].

The location of the phase transition is estimated from lattice QCD calculations. A mixed phase might exist near the phase boundary. Extrapolations to realistic quark masses suggest the existence of a critical point as shown in the phase diagram. The exact location of this point depends mainly on the mass of the strange quark. In the region of small baryon density left of the critical point a smooth crossover phase transition is expected, while at higher baryon densities a first order transition is

predicted. The two cases for a QGP in nature mark the extreme points in the diagram: neutron stars with low temperature and high net baryon density, and the early universe almost net-baryon free at high temperature.

Relativistic heavy ion collisions are used to study the phase diagram experimentally. Depending on the species of the collision partners and their energy, different regions can be explored.

2.4 Relativistic Heavy Ion Collisions

To study nuclear matter under extreme conditions, it is necessary to create hot and dense nuclear matter in the laboratory. This can be achieved by colliding nuclei, either by shooting accelerated ions at a stationary target, or by head-on collisions of two ion beams. In order to achieve the biggest volume of excited nuclear matter, very heavy nuclei such as gold (Au) or lead (Pb) are used. To disentangle effects stemming from the creation of large volumes of high energy density from normal effects of high energy nucleon-nucleon collisions and from simple nuclear effects, comparisons to reference measurements are crucial. For studying the effects of high energy nucleon-nucleon collisions, proton-proton collisions are used as a reference. The influence of nuclear effects is investigated in nucleon-nucleus collisions, such as p+Pb collisions, or collisions of a very small nucleus with a much larger nucleus, such as deuteron-gold (d+Au) collisions.

Currently there are four major facilities where such experiments are carried out. At the Schwerionen-Synchrotron (SIS) at the Gesellschaft für Schwerionenforschung (GSI) nucleus-nucleus collisions at beam energies of up to 1 GeV per nucleon (for Uranium) are studied. Higher energies are reached at the Alternating Gradient Synchrotron (AGS) and the Relativistic Heavy Ion Collider (RHIC) at Brookhaven National Laboratory (BNL), and the Super Proton Synchrotron (SPS) at the European Center for Particle Physics (CERN). SIS, AGS and the SPS have fixed-target experimental programs, while RHIC, which began operation in 2000, collides two ion beams, thus reaching much higher center-of-mass energies.

2.4.1 Evolution of the Collision

The time evolution of a heavy ion collision can be divided into several stages. The existence of some of these stages and the total duration depends on the available energy. The nuclei collide, creating a volume of high energy density between them. The baryon density of this hot region, called fireball, is quite low at the highest accessible energies at RHIC, since the nuclei are almost transparent at relativistic energies. Full transparency has been suggested by Bjorken [5], but recent experimental results show that this is not reached at RHIC [6]. The amount of stopping in

the collision can be studied by measuring antibaryon to baryon ratios, as the baryon number in the system is conserved. When the fireball expands and cools, quarks form stable hadrons, which, after more expansion, cease to interact inelastically, thus fixing the abundances of the various particle species. This point is called chemical freezeout. At even later stages, elastic collisions cease, fixing also the momentum distributions. This is referred to as the thermal freezeout.

2.4.2 Stopping and Baryon Transport

Since the baryon number is a conserved quantity, the distribution of net baryons, given by the difference of baryons – antibaryons, provides information about the collision dynamics. Initially, the total baryon number is contained in the projectile and the target, while after the collision, non-vanishing net-baryon yields are observed far from beam rapidity. This is a consequence of stopping and baryon transport. The rapidity loss of the incoming baryons determines the available energy for particle production.

Microscopically, there are three processes in nucleon–nucleon collisions that lead to a transport of baryons away from beam rapidity [7], in which either one, two or all three valence quarks are stripped off. In the first case, the final-state baryon is produced from a valence diquark, which picks up a sea quark to form a baryon. The diquark is created in the initial collision by the fragmentation of an incoming baryon into quark and diquark. In the second process also the diquark is broken up, and the final-state baryon forms out of one valence and two sea quarks. In both these cases, the baryon number remains associated to a specific quark throughout the collision. However, it is also possible that gluonic structures, referred to as string or baryon junctions, can trace the baryon number through the collision [8]. This structure dresses up with three sea quarks to form the final-state baryon.

In all three cases, the final-state baryon can have a quark composition which differs from that of the initial baryon. Depending on the creation mechanism, it contains two, one or no quarks of the initial baryon.

Any process which involves a common diquark cannot lead to large baryon transport, since the newly formed baryon contains a large fraction of the initial nucleon momentum. However the junction mechanism can lead to large stopping in a single collision because no valence quarks of the incoming nucleon are retained.

In nucleon–nucleus or nucleus–nucleus collisions, participating nucleons can suffer multiple collisions with constituents of the reaction partner. This will naturally lead to larger stopping, since several baryon transporting reactions can take place. In addition, modifications of the parton distributions in nuclear matter and scattering in the final state of the reaction might contribute.

2.4.3 Experimental Observables

Since most particles detected in the experiment carry information mainly from the chemical or thermal freezeout, the properties of the early stages of the collision can only be determined indirectly. The study of the momentum distribution allows the determination of the thermal freezeout temperature, while the study of particle abundances yields the chemical freezeout parameters.

The study of strange particles offers interesting possibilities since strangeness is not present in the incoming nuclei, but is produced in the collision. Strange hadrons are produced in hard initial interactions and in subsequent softer collisions. In the presence of a QGP, additional production channels are available, such as the thermal production of strange quarks and antiquarks from gluons. Since the quark masses are lower than the hadron masses, this leads to a lower threshold energy and higher abundance of strangeness, as only the quarks and not the hadrons have to be produced in the deconfined phase. Thus, an enhancement of strange particle production in nucleus–nucleus collisions with respect to simple nucleon–nucleon collisions is expected if a QGP is created, as proposed by Rafelski [9]. It is expected that the enhancement increases with strangeness content, being most prominent for the triple strange Ω^- .

An emerging field is the study of highly energetic particles created in hard parton–parton collisions which become measurable at RHIC energies. In the absence of a hadronic medium, such a hard collision always produces two azimuthally back-to-back sprays of particles, so-called jets, providing a unique signature. However, it is observed that when one selects a jet in central Au+Au collisions, the expected away side jet is highly suppressed. This is attributed to the fact that the highly energetic parton loses energy when traveling through a dense and strongly interacting medium, such as a QGP, and thus only the jet that is emitted toward the near surface of the medium retains its original properties. A d+Au reference experiment in which both jets are observed [10] demonstrates that the suppression of the away–side jet is not a nuclear initial state effect.

Given the complicated nature of most of these and many other signatures (see for example [11, 12]) and their indirect link to the possible QGP phase in the collision, most observations can also be explained in different scenarios not involving the creation of a QGP. Only with the combination of many experimental observations will it be possible to establish convincing evidence for the existence of this new state of matter.

Chapter 3

Experimental Setup

In a collider experiment the accelerator and the detector setup are intimately connected. The accelerator complex delivers the colliding particle beams. STAR is one of the two big heavy ion experiments at the Relativistic Heavy Ion Collider (RHIC). The Forward Time Projection Chambers (FTPCs) of the STAR arrangement are described in detail since they provide the measurements for the present analysis.

3.1 The Accelerator Complex

RHIC is the final stage of a chain of mutually injecting accelerators. It is designed to accelerate and collide different particle species with a rigidity of more than 800 Tm. For fully stripped gold ions (79+) in collision this corresponds to a maximum center of mass energy ($\sqrt{s_{NN}}$) of 200 GeV per nucleon pair. This energy is more than an order of magnitude higher than the energy reached in previous heavy ion experiments. In addition to the heavy ion research program, RHIC is also used to study collisions of polarized protons to investigate the spin structure of the nucleon.

In order to be able to collide positively charged heavy ions RHIC comprises two separate concentric superconducting synchrotrons with 3.8 km circumference. Collisions can take place at the crossing points of the two rings. Six such interaction points exist around the RHIC ring, four of which are currently used by experiments.

RHIC needs other accelerators to provide a fully stripped ion beam. The complex is illustrated in figure 3.1. In the case of gold, negative ions are created in a pulsed sputter ion source, then accelerated with a tandem accelerator to 1 MeV/A and ionized to a positive charge state by passing through stripper foils. Next, the ions are accelerated to 100 MeV/A in the AGS Booster, and ionized to 77+, leaving only the two innermost electrons of the gold atom. These highly charged ions are injected into the Alternating Gradient Synchrotron (AGS) and accelerated to 10.8 GeV/A.

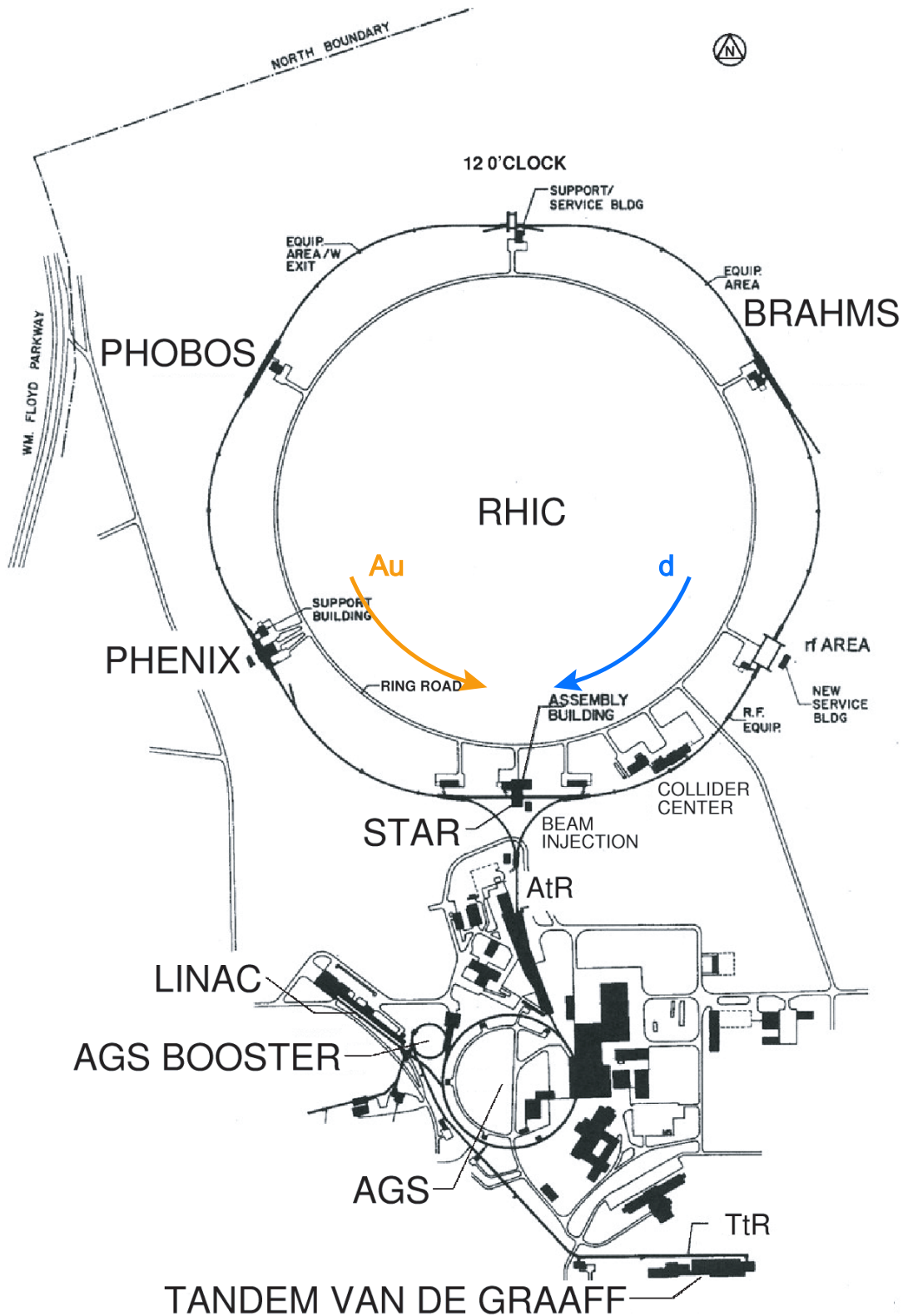


Figure 3.1: The RHIC accelerator complex at Brookhaven. Ions are accelerated in the Tandem, the Booster and the AGS before injection into RHIC and acceleration to full energy. The arrows inside the ring indicate the flight direction of deuterons and gold ions in the 2003 run.

After stripping to full ionization (79+), the Au ions are injected into RHIC, where they are accelerated to their final energy, and then kept there for the duration of a store, typically 5 to 10 hours. The second collision partner, deuterons, are produced in a sputter source from TiD. These negatively charged deuterium ions follow the same path as the gold.

A technical overview of the RHIC project can be found in [13], and a detailed description of the accelerator itself in [14].

3.1.1 Heavy Ion Experiments

There are four heavy ion experiments at RHIC, occupying four interaction points. These are BRAHMS (Broad Range Hadron Magnetic Spectrometers), PHOBOS, PHENIX (Pioneering High Energy Nuclear Interaction eXperiment) and STAR (Solenoidal Tracker At RHIC). The experiments focus on different aspects of the heavy ion collisions, and together yield a comprehensive picture, with sufficient overlap to allow the verification of crucial results by several experiments.

BRAHMS [15], the first of the two small setups, specializes on measuring hadrons over a wide rapidity range. This is accomplished by a movable spectrometer arm of narrow acceptance that can cover forward angles and a small TPC at mid rapidity. In addition, particle identification is provided by a RICH¹ and a TOF² system.

PHOBOS³ [16] is the other small heavy ion experiment at RHIC. It uses silicon detectors in a two-arm magnetic spectrometer and is capable of reaching very high trigger rates. The setup has a wide acceptance for particle counting.

PHENIX [17] is one of the two large RHIC experiments. It focuses on leptonic and photonic probes, and specializes in reconstructing light and heavy vector mesons (ϕ , J/Ψ , ...) via their decay products. It consists of multiple detectors to cover a wide range of observables. PHENIX has two central arms that measure hadrons, electrons and photons, and two arms in forward and backward direction for the measurement of muons. There are additional detectors for event characterization, such as multiplicity determination.

STAR [18], the second large experiment, also consists of multiple detector systems. Here, the aim is the coverage of a large phase space and the simultaneous measure-

¹**Ring Imaging Cherenkov** counter. This detector measures the particle velocity via the opening angle of photons emitted when particles pass through matter at a velocity which exceeds the velocity of light in that medium.

²**Time Of Flight**. The particle velocity is obtained by a precise measurement of the time of flight from the interaction vertex to the detector. Together with momentum information, the particle mass can be measured.

³Originally, a large experiment named MARS was proposed, but reduced in size and versatility due to budget constraints. The new, smaller experiment was named PHOBOS after one of Mars' moons.

ment of a multitude of different hadronic observables, ranging from single particle spectra (including strange, multi strange and charmed particles), event-by-event fluctuations and particle correlations to particle jets with high transverse momentum.

3.1.2 RHIC performance in 2003

In RHIC, the ions are arranged in bunches around the ring, with a maximum number of 120 bunches, some of which have to remain unfilled to facilitate the dumping of the beam at the end of a store. For the d+Au run in 2003, patterns of 56 and 110 bunches have been used. In the 110 bunch pattern, there is a bunch crossing every 107 ns in each of the interaction points, leading to an interaction frequency of close to 10 MHz. The bunch length in colliding beams is around 3 ns, corresponding to an overlap region of about 2 m in the interaction zones.

The number of ions per bunch depends on the particle species. Typical values in 2003 were 8×10^8 gold ions per bunch and 1×10^{12} deuterium ions per bunch. The average luminosity in the 2003 d+Au run was around $2 \times 10^{28} \text{ cm}^{-2} \text{ s}^{-1}$, with typical peak luminosities after injection of around $5 \times 10^{28} \text{ cm}^{-2} \text{ s}^{-1}$. In total, an integrated luminosity of 19.85 nb^{-1} was delivered to the STAR experiment during the d+Au run.

3.2 The STAR Experiment

The STAR detector [19] consists of a number of detector systems, most of which are enclosed inside a large solenoidal magnet at room temperature that provides a uniform magnetic field of up to 0.5 T parallel to the beam axis.

Figure 3.2 shows a schematic sketch of the STAR experiment. The major subsystems serve tracking and particle identification, calorimetry for energy determination and event triggering. Recent additions to the setup are not included in the drawing. They comprise a time of flight (TOF) system based on multiple resistive plate chambers, a segmented photon multiplicity detector (PMD) of alternating proportional counters and lead converters at $\eta = 3.5$ and a forward π^0 detector consisting of a finely segmented lead-glass calorimeter which permits the reconstruction of π^0 s from their two-photon decay.

3.2.1 Tracking Detectors

The tracking detectors in STAR are used to determine the charge and the momentum of charged particles produced in the observed heavy ion collisions. The charge is

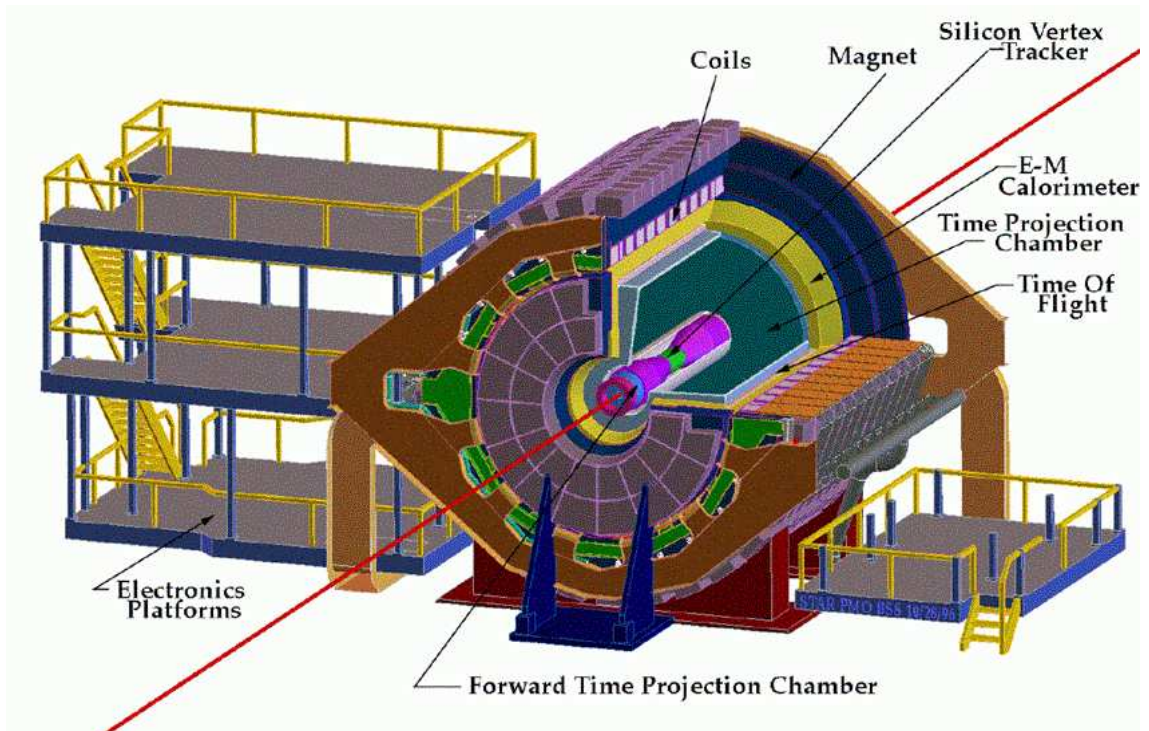


Figure 3.2: Sketch of the STAR detector at RHIC. The beam axis is illustrated by the red line. Not all subsystems are included.

determined via the sign of the curvature of the particle track in the magnetic field. The transverse momentum p_t (the momentum perpendicular to the beam axis) is given by

$$p_t = 0.3 q B \rho \text{ (GeV/c)} \quad (3.1)$$

where q is the charge of the particle, B is the magnetic field in T parallel to the beam axis and ρ is the helix radius of the trajectory of the particle in m.

The main tracking detector in STAR is the Time Projection Chamber (TPC). With a length of 4.2 m and a diameter of 4 m it is the world's largest TPC currently in operation. The acceptance of the detector is ± 1.5 units in pseudorapidity η around mid-rapidity. The gas used in the drift volume is P10, a mixture of 90% Ar and 10% CH₄. The readout is situated at both ends of the TPC and is at ground potential, the drift field is created by applying -31 kV at a thin cathode membrane in the center of the TPC. This causes the electrons created by the passage of an ionizing particle to drift toward the readout plane. The readout plane is segmented into a total of $\sim 137\,000$ readout channels which are read out in 382 timebins. The detector achieves a two-track resolution of 2 cm. In favorable cases the particles can be identified via their specific energy loss in the detector volume.

Inside the TPC, tracking close to the interaction point is provided by the Silicon Vertex Tracker (SVT), which consists of 216 silicon drift detectors operated at room

temperature and arranged in three cylindrical layers 7, 11 and 15 cm from the beam axis. Currently, a fourth layer outside the SVT, the Silicon Drift Detector (SSD) is being added to the inner tracking system. SVT and SSD cover $|\eta| \leq 1$ with complete azimuthal symmetry.

On both ends of the detector, the forward time projection chambers (FTPCs, see section 3.3) extend the acceptance of STAR. The FTPCs cover $2.5 < |\eta| < 4$ in pseudorapidity and the full azimuthal angle. These detectors provided the data presented in this work.

3.2.2 Calorimeters

The STAR calorimeters are electromagnetic calorimeters designed to measure the energy of photons and electrons. They consist of two subsystems providing full azimuthal coverage over 3 units in pseudorapidity. The barrel electromagnetic calorimeter (BEMC) provides full azimuthal coverage in $-1 < \eta < +1$ and the endcap electromagnetic calorimeter (EEMC) extends the coverage on one side to $\eta = 2$.

Both calorimeters are sampling calorimeters, where only a small fraction of the shower energy is detected in scintillator layers sandwiched between lead plates used as conversion material. The calorimeters operate with shower maximum detection in order to enhance hadron rejection and improve electron–photon separation.

The calorimeters feature short readout times and are used in the trigger system to select rare events, such as high transverse momentum jets or J/ψ and Υ candidates.

For the deuteron–gold run in 2003, half of the BEMC modules were installed, covering 2π in azimuth and $0 < \eta < 1$. Also half of the EEMC was present.

3.2.3 Trigger Detectors and Data Acquisition

The trigger detectors in STAR are used to characterize the event and to decide whether it should be recorded or not. They are all fast detectors, fully pipelined with short readout times. There is a central trigger barrel (CTB) around the TPC at $|\eta| < 1$, the beam–beam counters (BBCs) at both sides of the STAR detector and the zero degree calorimeters (ZDC) in the accelerator tunnel on both sides of the interaction area.

The CTB and the BBC consist of plastic scintillators read out via photomultipliers. They are used to register charged particles and to provide a first estimate of the multiplicity of the event. The ZDCs detect neutrons that did not participate in the collision and thus fly in beam direction. The ZDCs are located behind the first set of magnets in the accelerator tunnel where all charged particles are deflected

by the magnetic field. By forming a coincidence between both ZDCs, the vertex position can be derived from flight time differences. However, this is only possible if neutrons are detected on both sides of the interaction region. In d+Au collisions, this is usually not the case, so a vertex determination with the ZDCs is in general not possible in these events.

The trigger system supports different trigger setups simultaneously, so that events meeting a variety of trigger conditions can be recorded in the same run. By down-scaling trigger conditions that are fulfilled frequently, triggers for rare events can be enriched in the data stream. During the d+Au data run in 2003, typical trigger rates of 70 Hz were achieved. Upgrades of detector electronics, the trigger and the data acquisition system will increase this number to over 100 Hz for central Au+Au events in the short term and to several kHz in the long term.

The data acquisition system DAQ is designed to handle the data generated by the different detectors and to send it to mass storage. This task requires zero suppression on the detector frontends, since the raw data volume is in the order of 200 MB per event and thus much too large to be transmitted to the DAQ system at normal trigger rates. The data transfer from the detectors to the DAQ system proceeds via optical fibers and reaches volumes of up to 300 MB/s, with typical data rates around 120 MB/s during data taking. The data rate to the HPSS storage facility is of the order of 80 MB/s. Thus extensive buffering capability is provided to take advantage of periods with low data rate and the time between collider stores to move data from the DAQ system to mass storage.

Online cluster finding for the TPC has been developed to increase the sustainable trigger rate. A Level 3 trigger system provides the capability for real time reconstruction of events, and is used to flag events with special signatures.

3.3 The STAR Forward TPCs

Time Projection Chambers have been used in several earlier heavy ion experiments because they are capable of providing reconstruction and momentum measurement for large numbers of tracks in high multiplicity environments with a moderate number of electronic readout channels. They have a high granularity over large active volumes, which is mandatory for particle identification via the specific energy loss.

3.3.1 The Principle of Time Projection Chambers

The Time Projection Chamber (TPC), first proposed by David Nygren in the late 1970s, exploits the fact that particles traversing a gas volume will ionize some of the gas atoms or molecules, thus creating positive ions and electrons. In an electric

field, the electrons and ions will drift along the electric field lines. The electrons are collected with readout devices that measure two-dimensional position information. By measuring the time difference from the passage of the particle to the arrival of the charge at the readout, the third coordinate can be determined. Thus a three-dimensional reconstruction of particle trajectories is possible with a single readout plane. The time when the particles passed through the TPC has to be provided by external detectors, typically by the trigger system of the experiment.

Most TPCs operate in a constant electric field, which leads to a linear dependence of the drift distance on the time. This facilitates the track reconstruction and the calibration of the detector. More complicated geometries are possible and have been successfully applied, for example in the TPC of the CERES experiment at CERN [20].

3.3.2 Design Considerations

The two FTPCs in STAR cover the pseudorapidity range $2.5 < |\eta| < 4.0$ in STAR, which corresponds to track angles with respect to the beam axis from 2° to 9.3° . In this region of high particle density, a two-track resolution in the order of 2 mm is necessary. To get good momentum resolution for the tracks that have a small angle with the solenoidal magnetic field, high spatial resolution is needed. To fulfill both requirements, a novel design was adopted to achieve high particle detection efficiency in an environment of very high track density while meeting severe space constraints imposed by the other STAR components. To meet both these criteria a drift toward the detector endcaps, as in a classical TPC, is not practical, since the long drift path leads to cluster broadening which reduces the two-track separation. Moreover the short projected length of low-angle tracks on the endcap makes the resolution of individual hits difficult.

To overcome these difficulties, a radial drift design was adopted. In this geometry, the electrons drift radially towards the outer surface of the detector. Due to the magnetic field parallel to the detector axis and thus perpendicular to the electric field, the drifting charge clouds get deflected by the Lorentz force ($\vec{E} \times \vec{B}$). The radial drift spreads clusters originating from near the inner radius of the detector apart, thus leading to improved two-track separation in the area with the highest track density. The short drift distance in the radial geometry permits the use of a slow gas mixture with small diffusion, which is important for good cluster separation. The chosen Ar(CO₂) 50%/50% mixture fulfills this requirement, and in addition has small $\vec{E} \times \vec{B}$ effects, which facilitates reconstruction.

For sampling particle tracks at several positions along their trajectory through the detector, the outer surface has rings of padrows which read out the amplified signal, as described in subsection 3.3.4. The momentum resolution improves with the num-

ber of hits on a track, so the highest possible number of such padrows is desirable. However, the available space for the readout electronics and the cooling capabilities limit this number to ten. This limits the momentum resolution to the order of 15% for primary tracks coming from the collision vertex.

3.3.3 Field Cage and Sensitive Volume

Figure 3.3 illustrates the detector setup, including the aluminum support structure, the field cage and the readout chambers.

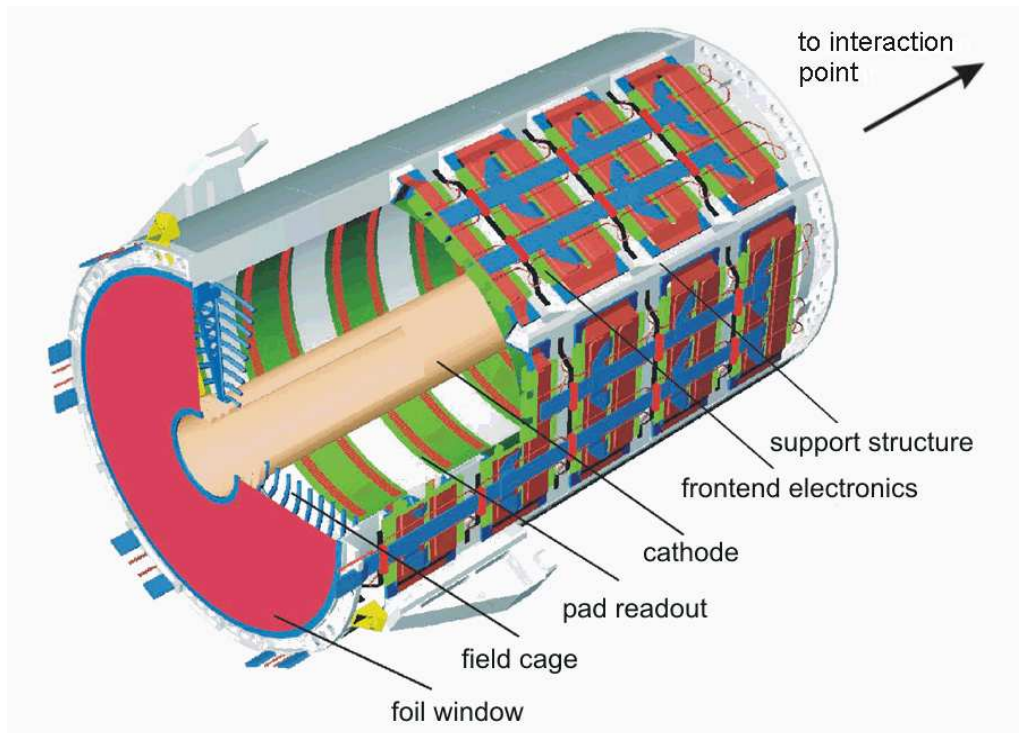


Figure 3.3: Layout of the forward TPCs. The field cage with potential rings at the endcaps, the padrows on the outer surface of the gas volume and the front end electronics are shown. The readout boards which are situated at the left end of the detector are not included in the drawing.

To ensure a radial electric field with the smallest possible corrections, a high precision field cage is needed to define the field in the readout volume. Negative high voltage (-10 kV) is applied to the cathode, a metal coated plastic tube. This cathode is mounted in the center of the detector. At both ends of the detector, the potential is defined by a field cage of concentric rings connected by a resistor chain. At the outer radius, ground potential is provided by the Frish grid.

During the calibration of the detector, mechanical imperfections in the field cage, especially a small displacement of the central cathode of approximately $300 \mu\text{m}$, have been detected by an azimuthal dependence of the maximum drift time. These effects

can be corrected for to a large extent, but underline the importance of mechanical precision in the detector design.

The detector body is 1.2 m long, starting 1.5 m from the nominal interaction point. The sensitive volume of the detector is 94 cm along the beam axis ($162.75 \text{ cm} < |z| < 256.75 \text{ cm}$), with an inner radius of 7.73 cm and an outer radius of 30.05 cm. The cathode voltage leads to a radial electric drift field which increases from 240 V/cm to 930 V/cm towards the cathode. This field results in electron drift velocities from 0.3 cm/ μs to 1.4 cm/ μs in the Ar(CO₂) mixture. Over the total drift length, the deflection due to the Lorentz force in the magnetic field is around 5°.

3.3.4 Detector Readout

The number of electrons produced by the ionizing particles in a charge cluster is much too small to be detected with fast electronics, so an amplification is needed. This is done by exploiting avalanche multiplication in gases in strong electric fields. Several methods are available to achieve this such as multiwire proportional chambers and GEM foils.

The avalanche amplification leaves positive ions that drift into the detector volume. Since the ions drift much slower than the lighter electrons, it would take very long until they get neutralized at the cathode. The positive charge leads to a distortion of the electric field, and has to be eliminated as much as possible. This is achieved by introducing a gating grid in the detector. When open, the gating grid is transparent to charge, while in the closed position, it prevents ions from drifting into the detector volume. To achieve that, power supplies that can switch voltages in very short time are needed. As soon as the detector receives a trigger the gating grid is opened, and closed after the readout time, determined by the maximum possible drift time.

The STAR FTPCs use multiwire chambers, which amplify the charge near thin wires at high positive potential which are stretched over pads, see the schematic drawing in figure 3.4. The wire chambers are operated at voltages around 1800 V, resulting in gas amplifications of about 2000. An increase of the amplification voltage by 100 V leads to a doubling of the gain. The electron avalanche induces signals on the pads of the readout plane which are read out by the detector electronics.

The readout chambers are bent to maintain an exactly radial electric field in the detector. This poses a construction challenge. To achieve optimal charge sharing over several readout pads, the anode wires should cross the pads at a 90° angle, which is not possible in a curved geometry. Studies showed that a crossing angle of 9° gives very good results. Here the change of the distance of the wires to the pads is negligible over the length of the pads, and good charge sharing is achieved. The wires are positioned 1.5 mm above the readout pads. Figure 3.4 illustrates the readout setup with gating and Frish grid and the amplification wires.

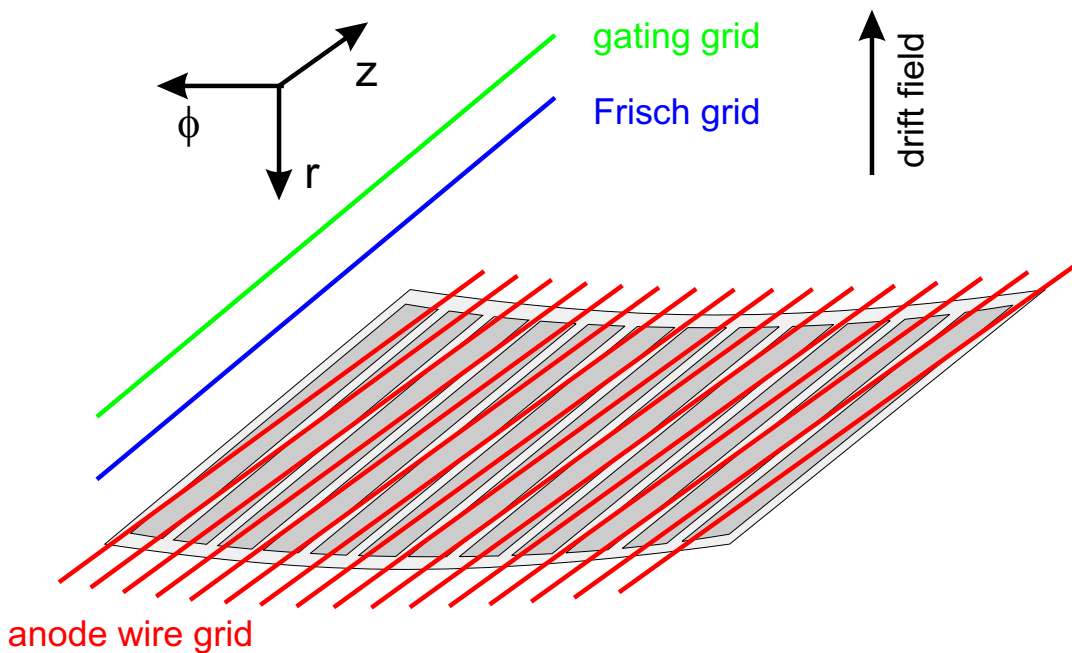


Figure 3.4: Arrangement of potential defining and amplification grids in the detector. The anode wires cross the pads at an angle of 9° , the gating grid and the Frisch grid are parallel to the pads and the beam axis. For better visibility, only one wire each of these grids is shown. The readout electrode with the pads is bent to achieve a perfectly radial drift field.

Each readout chamber covers 60° in azimuth, and has two padrows with 160 pads each. The pads are 1.9 mm by 20 mm in size. One FTPC has a total of 10 padrows, so there are 30 readout chambers per detector.

The signal on the pads is read out with front-end electronics comprising a preamplifier/shaper stage and a digitization unit (ADC). The electronics sample the signal in 256 consecutive time bins. Since the length of a time bin is given by the RHIC clock, its length depends on the beam energy. At full RHIC energy, a time bin corresponds to 213.15 ns. Five so-called FEE cards are necessary to read out all 320 pads of one readout chamber. The FEE cards pass their data on to the readout boards located on the outside ends of the FTPCs, where further processing of the data, such as zero suppression, takes place. The readout boards send the data via optical fibers to the STAR data acquisition system, where it is combined with data from other detectors and written to mass storage.

3.3.5 Calibration and Reconstruction

In order to use the recorded data for physics analysis, the particle tracks in the detector have to be reconstructed. This requires a calibration of the detector parameters and an understanding of effects caused by mechanical and electronic imperfections. In this process, detector simulations (see chapter 4) are used to investigate the con-

sequences of detected imperfections and to develop corrections that can be used in the reconstruction.

The FTPCs have a laser system that is used to measure the drift velocity. This determines the relation between the measured time and the radial position of the particle track. Also the deflection angles due to the Lorentz force are determined this way. For a detailed description of the laser system and the detector calibration refer to [21].

Faulty electronics are determined by using pulsers, which send a rectangular pulse to the Frish grid (normally at ground potential). The rising edge of the pulse induces a signal on the pads that is picked up by the electronics. The amplitude of these signals is used to map the gain of the front-end electronics and to localize dead pads. This information is needed for a realistic detector simulation, see section 4.2, and to locate broken electronics for replacement during maintenance periods.

The reconstruction of particle tracks proceeds in two steps, namely the finding of charge clusters, which is done for each padrow, and the combination of clusters from all rows into tracks. The employed methods are extensively documented in [21, 22], while a complete summary of the detector parameters can be found in [23].

3.4 **d+Au Collisions**

The focus of this work is on the analysis of d+Au collisions at a center of mass energy per nucleon pair $\sqrt{s_{NN}}$ of 200 GeV. This energy corresponds to a beam rapidity of $y_{beam} = \pm 5.37$. The dataset was recorded from January through April 2003. This section presents an introduction to these collisions.

An important use of this dataset is as a reference measurement for comparison to results obtained in Au+Au collisions. Due to the small system size it is expected that no QGP is created in d+Au collisions. However, due to the presence of the Au nucleus, nuclear effects will still contribute, in contrast to p+p collisions. This opens up the possibility to disentangle initial-state effects originating from the Au nucleus and final-state effects from the dense matter created in the collision. Results from d+Au collisions have been used to establish that the disappearance of away-side jets in Au+Au collisions (see section 2.4.3) is a final-state effect.

At the SPS, the reference measurements were done with p+Pb collisions. RHIC chose d+Au for a variety of reasons. Deuterons have the technical advantage that their charge to mass ratio is similar to that of gold, which relaxes constraints on the collider beam optics. The properties of the deuteron, discussed further down, can be exploited for a variety of studies.

3.4.1 Properties of the Beam Nuclei

In d+Au reactions, two very different nuclei collide. While the gold nucleus is heavy and tightly bound, the deuteron is a light and rather loosely bound system of only two nucleons.

The used gold isotope ^{197}Au is the only stable gold isotope. It has a binding energy of 7.92 MeV per nucleon. Its radius can be calculated from the formula

$$r = r_0 A^{\frac{1}{3}}, \quad (3.2)$$

where A is the mass number and $r_0 = 1.2$ fm. This yields a radius of 7 fm for the gold nucleus.

The deuteron has a binding energy of 1.11 MeV per nucleon and consists only of two nucleons. Thus the definition of the nuclear radius is not straight forward, and the empirical formula for the nuclear radius is not applicable. The radius of the deuteron can be obtained by measuring the wavelength shift of a spectral line when comparing hydrogen to deuterium. This gives a structure radius of 1.98 fm [24]. The wave function of the deuteron stretches out to much bigger radii, as illustrated in [25].

Due to these properties of the deuteron, collisions with very big impact parameters⁴ are possible. This is also confirmed by the calculations discussed in section 3.4.3. In a significant portion of the interactions only one of the two deuteron nucleons will participate in the reaction. The cross section for this type of process is around 40% of the total hadronic cross section. In STAR, such processes are only identifiable when the neutron from the deuteron did not participate in the collision. In that case, a beam momentum neutron is detected in the zero degree calorimeter in the deuteron direction, see section 3.2.3. These events are mostly peripheral p+Au collisions. For the selection of processes with a spectator proton, a device for the detection of the beam momentum proton would be necessary. Currently, such a device does not exist in STAR.

Given the different size and binding strength of the two reaction partners, d+Au collisions are characterized by an asymmetry between the projectile (d) and target (Au) side. A nucleon from the deuteron usually participates in several collisions with Au participants on its way through the tightly bound gold nucleus. On the other hand, most participating Au nucleons will only suffer one single collision with one of the deuteron's nucleons.

Figure 3.5 illustrates this asymmetry in d+Au collisions. It is expected that this asymmetry leads to differences in particle production and baryon transport on the two collision sides.

⁴The impact parameter is defined as the distance of closest approach of the centers of the two colliding nuclei.

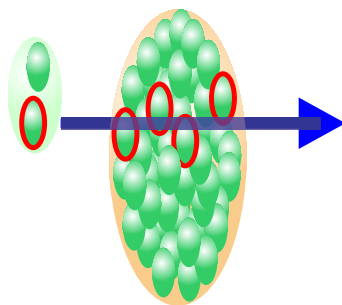


Figure 3.5: Illustration of a $d+Au$ collision. A nucleon from the deuteron participates in several collisions on its way through the gold nucleus. Each participating gold nucleon only suffers one collision.

3.4.2 Charged Particles

The pseudorapidity distribution of charged hadrons in $d+Au$ collisions illustrates the asymmetry of the particle production caused by the asymmetry of the collision system. The experiment with the most complete pseudorapidity coverage at RHIC is PHOBOS (see section 3.1.1). Thus the charged particle density as a function of pseudorapidity measured by the PHOBOS experiment for minimum bias collisions [26] is shown in figure 3.6. The acceptance of the STAR TPC and the two FTPCs is marked by the shaded bands in the plot. By definition, the flight direction of the gold beam is toward negative z , thus negative rapidity. In the STAR coordinate system (see appendix B) this corresponds to East.

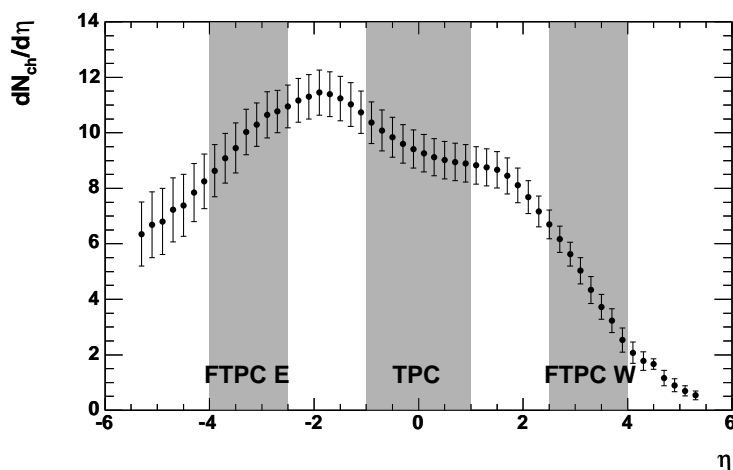


Figure 3.6: Pseudorapidity distribution of charged particles $dN_{ch}/d\eta$ in $d+Au$ minimum bias collisions measured by PHOBOS [26]. The acceptance of the STAR TPCs is highlighted.

3.4.3 d+Au Collisions at STAR

For the d+Au data taking, the STAR trigger system was operated with multiple triggers. In addition to the standard minimum bias trigger, special triggers to enrich events with high transverse momentum particles and other special properties were used. The minimum bias trigger required at least one beam-rapidity neutron in the ZDC in the gold beam direction. This condition is met for all collisions that lead to a breakup of the gold nucleus. The ZDC based minimum bias trigger accepts $95\% \pm 3\%$ of the d+Au hadronic cross section [10].

Event Cuts

For the present analysis of d+Au events taken with the STAR detector, not all events are of interest, since multiple trigger conditions are used. Here only the minimum bias triggers are selected.

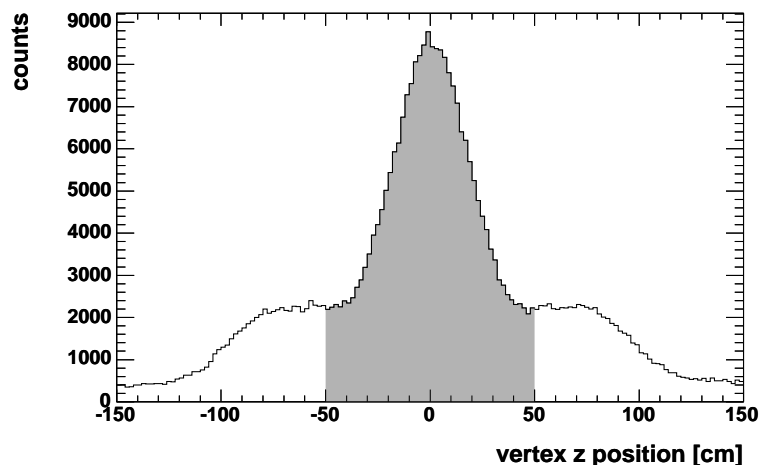


Figure 3.7: Typical vertex distribution for d+Au minimum bias events. For this figure, about 400 000 events are used. The shape of the distribution changes with time since it depends on collider parameters. The shaded area shows the events used for analysis, with a primary vertex within 50 cm of the center of the TPC.

Because the particle beams in the STAR interaction region are parallel, the distribution of collision vertices is very broad along the beam axis. It is determined by the length of the beam bunches, which was around 3 ns (corresponding to an overlap region of 2 m) in the d+Au run. Since the minimum bias trigger is based on a single detector, a restriction of the accepted vertex range due to cuts on flight time differences is not possible. This leads to a very wide distribution of the accepted event vertices along the beam axis, as shown in figure 3.7. For vertices displaced far

from the center of the interaction region, the efficiency of the detectors changes significantly. To assure uniform performance in the used event sample, a cut restricting the vertex position to ± 50 cm from the nominal interaction point is applied. This cut, together with the implicit requirement that a primary vertex was reconstructed leads to a rejection of about half of the recorded events. The usable data sample in which the FTPCs operated without significant loss of readout channels contains 10 401 530 events.

Centrality Selection

For some parts of the analysis, it is necessary to select specific collision centralities, which are defined by the impact parameter b of the collision. Since this quantity is not directly measurable, a related quantity has to be used. It is expected that the number of particles produced in a collision increases with decreasing impact parameter. To avoid autocorrelations in the analysis, the centrality is determined from the particle multiplicity at mid-rapidity in the main TPC.

This TPC reference multiplicity is defined as the number of charged particle tracks that have more than 10 points, a distance of closest approach to the primary vertex of less than 3 cm and are within a pseudorapidity window of ± 0.5 from mid-rapidity.

In most cases, the interesting parameter is either the number of participating nucleons or the number of binary collisions. Their relationship with the observed particle multiplicities can be determined by so-called Glauber calculations. These can either be implemented as an analytical calculation based on overlapping nuclei or as Monte Carlo simulations based on a billiard-like collision model. An example of a Monte Carlo implementation is included in the HIJING event generator. For a detailed discussion of Glauber studies in Au+Au and d+Au collisions refer to [27].

Since the impact parameter is known in model calculations, comparisons of the predicted multiplicities to data can be used to estimate the average impact parameter for a given collision centrality. For the analysis of the d+Au data, STAR uses three centrality classes, namely the 20% most central events, 20% to 40% and 40% to 100%, as proposed in [28]. Figure 3.8 shows the impact parameter distribution for these centrality classes in d+Au events obtained from HIJING. There is some overlap between the three classes, but there is a clear correlation of particle multiplicity and impact parameter.

The distribution of the number of participating nucleons is given in figure 3.9. The large number of events with only two participating nucleons, one each from target and projectile, is apparent. Table 3.1 summarizes the mean impact parameter, the number of participants (total, projectile, target) and the number of binary nucleon-nucleon collisions for the three centrality classes and the events with a spectator neutron from the deuteron.

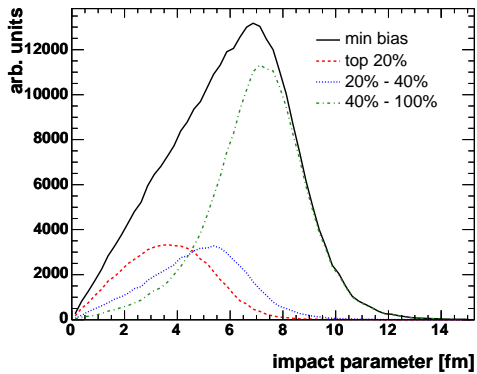


Figure 3.8: Impact parameter distribution for centrality classes selected on mid-rapidity multiplicity, taken from HIJING.

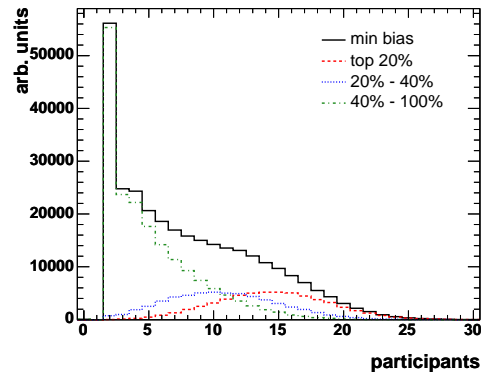


Figure 3.9: Number of participants for the d+Au centrality classes.

| centrality class | $\langle b \rangle$ | $\langle n_{part} \rangle$ | $\langle n_{part,d} \rangle$ | $\langle n_{part,Au} \rangle$ | $\langle n_{bin} \rangle$ |
|------------------|---------------------|----------------------------|------------------------------|-------------------------------|---------------------------|
| minimum bias | 5.9 fm | 8.0 | 1.6 | 6.4 | 7.5 |
| top 20% | 3.7 fm | 14.5 | 2.0 | 12.5 | 15.0 |
| 20% - 40% | 4.7 fm | 10.8 | 1.9 | 8.9 | 10.2 |
| 40% - 100% | 7.0 fm | 5.1 | 1.4 | 3.7 | 4.0 |
| ZDC neutron tag | 7.9 fm | 3.5 | 1.0 | 2.5 | 2.7 |

Table 3.1: Impact parameter, number of participants and binary collisions for the three centrality classes taken from HIJING.

Apart from the centrality selection based on multiplicity, the STAR zero degree calorimeters (ZDCs, see section 3.2.3) offer the possibility of identifying events where only the proton in the deuteron nucleus participated in the collision. Events of this type are characterized by a beam momentum neutron that continues in the deuteron direction and hits the ZDC. These events are referred to as ZDC neutron tag events. They mostly have large impact parameters, and open up the possibility to study peripheral p+Au collisions with the recorded d+Au dataset.

Figure 3.10 shows the reference multiplicity distribution in the main TPC for d+Au minimum bias events. The band marks the borders of the three centrality classes, the most peripheral bin ranging from 100% to 40%, the mid central bin from 40% to 20% and the most central bin containing the top 20% of all events.

When dividing the data sample into centrality classes, the vertex finding efficiency has to be taken into account. For events with a low multiplicity, the vertex is not always found. These events are ignored in the analysis, as a valid vertex is required for the Λ analysis, but they still contribute to the cross section. The correction for the vertex finding efficiency is required only in the peripheral bin. The overall

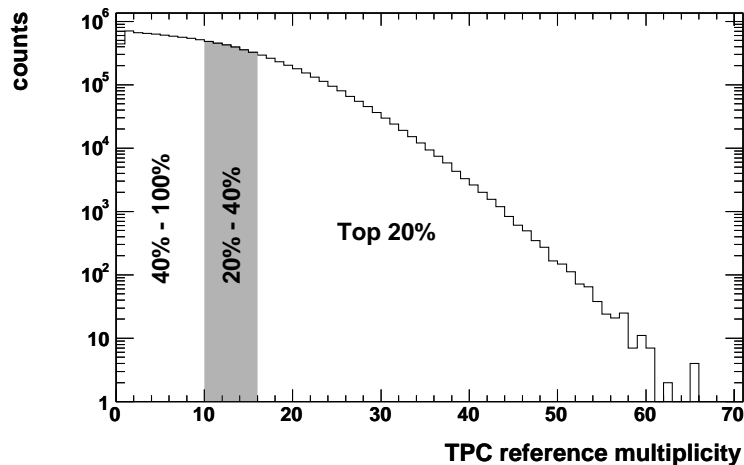


Figure 3.10: TPC Reference Multiplicity. The *d+Au* minimum bias dataset is divided into three multiplicity classes. In addition, a selection on the ZDC on the deuteron side can be used.

vertex finding efficiency in minimum bias events was determined to be 92.5% for events with a collision vertex within 50 cm of the nominal interaction point. Thus, the 10 401 530 recorded events with a reconstructed vertex correspond to 11.245 million minimum bias events.

With this corrected event number and the distribution of reference multiplicity, the borders of the three centrality bins can be determined. Since the reference multiplicity is an integer, these borders are shifted slightly from their nominal value. Table 3.2 summarizes the parameters of the used centrality classes.

| centrality class | multiplicity | centrality | events (corrected) |
|------------------|--------------|---------------|--------------------|
| minimum bias | 0 — 100 | 0% — 100% | 11.245 M |
| top 20% | 16 — 100 | 0% — 18.5% | 2.085 M |
| 20% — 40% | 10 — 15 | 18.5% — 40.2% | 2.433 M |
| 40% — 100% | 0 — 9 | 40.2% — 100% | 6.726 M |

Table 3.2: Parameters of the three centrality classes.

3.4.4 Models

For the interpretation of experimental results, model calculations are crucial. Since experimental observables are in most cases only linked indirectly to basic physical parameters and effects, the connection has to be established by theory.

There is a large variety of models that are based on different assumptions. By comparison of model predictions to experimental results, these assumptions can be

validated or falsified. Here some models that will be used to discuss results are introduced and their main features presented. All these models are event generators based upon Monte Carlo methods. They provide output which includes momenta and identities for all particles produced in a simulated event as well as information on the collision. This information can be used as input for detector simulations, or to extract predictions from the models for specific observables.

HIJING

HIJING [29] is the most widely used model for heavy ion collisions at RHIC. It is quite successful at reproducing the measured particle multiplicities and pseudorapidity distributions in Au+Au and d+Au collisions. However, weaknesses in the strange particle sector and problems with momentum distributions are known.

The HIJING model is a microscopic model that combines perturbative QCD inspired models for multiple jet production with phenomenological string models for soft particle production. Nucleus-nucleus collisions are treated as a superposition of binary nucleon-nucleon collisions. Glauber geometry for multiple collisions is used to describe the impact parameter dependence of the number of inelastic processes. Baryon transport is performed via the diquark conserving and the diquark breaking mechanism discussed in section 2.4.2. Jet quenching is introduced by energy loss in the dense medium created in the collision.

HIJING/B \bar{B}

HIJING/B \bar{B} [30] is based on HIJING but includes increased baryon number transport and hyperon production by baryon junctions (see section 2.4.2) in addition to the standard string model mechanisms of HIJING. The individual collisions in HIJING are not sufficient to explain the transport of baryon number over more than five units in rapidity necessary to reproduce the non-vanishing net baryon number at mid-rapidity in heavy ion collisions at SPS and RHIC. A precursor model was used by PHENIX to compare to Λ results in Au+Au collisions at $\sqrt{s_{NN}} = 130$ GeV [31]. Based on the new data available, an improved version of HIJING/B \bar{B} was introduced recently [32]. This version is used here. The calculations were done by V. Topor-Pop with a string tension constant $k = 1.5$ and are still preliminary.

AMPT

AMPT [33, 34] is a multi-phase model that uses different mechanisms for different phases of the collision. It starts from perturbative QCD motivated initial conditions and incorporates a subsequent partonic and hadronic space-time evolution.

HIJING is used to generate the initial parton distribution, then the parton rescattering is simulated by parton cascades. The hadronization of the partonic matter is treated with a HIJING - inspired fragmentation scheme. The evolution of the formed hadrons is described by a relativistic transport model. AMPT successfully describes different aspects of d+Au collisions [26]. Due to the multi-phase approach, better performance than for HIJING is expected for soft particle production, especially in the presence of nuclear effects.

NeXus / EPOS

NeXus [35] is designed to provide a unified treatment of nuclear reactions in the GeV and TeV energy range. It focuses on soft interactions using string theory and parton cascades. It is based on a universality hypothesis that assumes that the behavior of high-energy interactions is universal, e.g. does not depend on the particle type. The energy sharing between parallel processes is treated rigorously. A new version of the model, now called EPOS [36] was developed to study d+Au collisions at RHIC. It uses four components for particle production, namely projectile remnants, target remnants, soft and hard Pomerons (parton ladders). These components are treated in a multiple scattering formalism. Like in HIJING, there is no hadronic rescattering phase in the model.

RQMD

RQMD [37] is a transport model that focuses on the propagation of particles in the dense medium throughout the whole evolution of the reaction. It starts with the formation of strings and color ropes, which are created out of overlapping strings. Hadrons are then produced from the fragmentation of strings and ropes. The trajectories of all particles in the collision are followed, with thorough treatment of inelastic and elastic two-body reactions in the dense medium. RQMD has no mechanisms for jet and mini-jet production, but in contrast to HIJING, it provides a thorough treatment of soft multi-particle production and collective behavior of the produced particles.

3.4.5 Model Results

The results of the model calculations have either been obtained with the publicly available model codes (EPOS, HIJING, RQMD) or have been supplied by the authors of the models (AMPT and preliminary HIJING/B \bar{B}). The model curves in plots are always drawn by connecting the calculation results at different rapidities by straight lines.

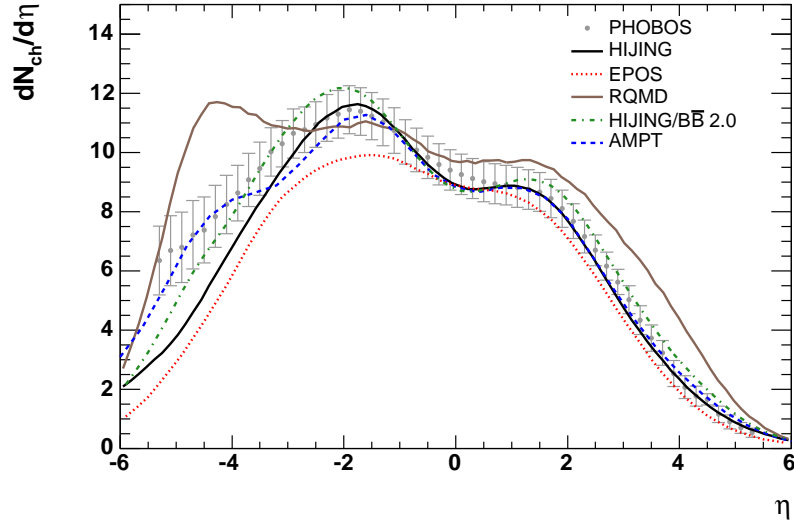


Figure 3.11: Pseudorapidity distribution of charged particles $dN_{ch}/d\eta$ in minimum bias d+Au collisions obtained by different models. The PHOBOS data [26] is shown as a reference.

Figure 3.11 shows the pseudorapidity dependence of the charged particle density $dN_{ch}/d\eta$ predicted by the five models discussed here. As a reference, the measurements by PHOBOS (see figure 3.6) are overlaid. This shows that AMPT provides the best description of the data [26]. The HIJING models agree with the measurements above $\eta \sim -3$. EPOS underpredicts the data especially on the gold side, but still reproduces the general shape. RQMD fails to reproduce the data and also shows too little pseudorapidity asymmetry.

Chapter 4

Detector Simulations

For complex detectors, simulations play an important role. They are necessary during the design phase to predict the performance of the system, and they are equally necessary during the later operation phase where one has to optimize analysis strategies and where simulations often are the only means of obtaining the necessary correction factors.

In STAR, this is achieved with a dedicated software framework, in parts specialized for FTPC simulation. It is grouped into three parts. First, the physics of particles traveling through the detector has to be simulated. For this, GEANT¹ is used together with a detailed model of the STAR detector. The results of GEANT, the location of charge clusters on particle trajectories, are then passed to simulation tools for the individual detector components. For the FTPC, the drift of the electrons in the detector gas and the response of the electronics to the charge arriving on the readout pads has to be simulated. This is done by a program package called *FtpcSlowSimulator*. The output of this tool can be passed through the normal reconstruction chain, and can be treated just like real data. However, for some studies, it is desirable to merge simulated information with real data to study effects under more realistic conditions, a process called embedding. For this, a program package called *FtpcMixerMaker* was developed by the author.

Figure 4.1 shows a flow chart that illustrates the software framework used for the simulation of the FTPCs. Especially the embedding framework is described in detail, since it was newly developed.

¹GEANT is a program package that simulates the passage of particles through matter. It has a variety of applications in high energy physics as well as in medical applications of radiation. A detailed description can be found at <http://wwwasd.web.cern.ch/wwwasd/geant/>.

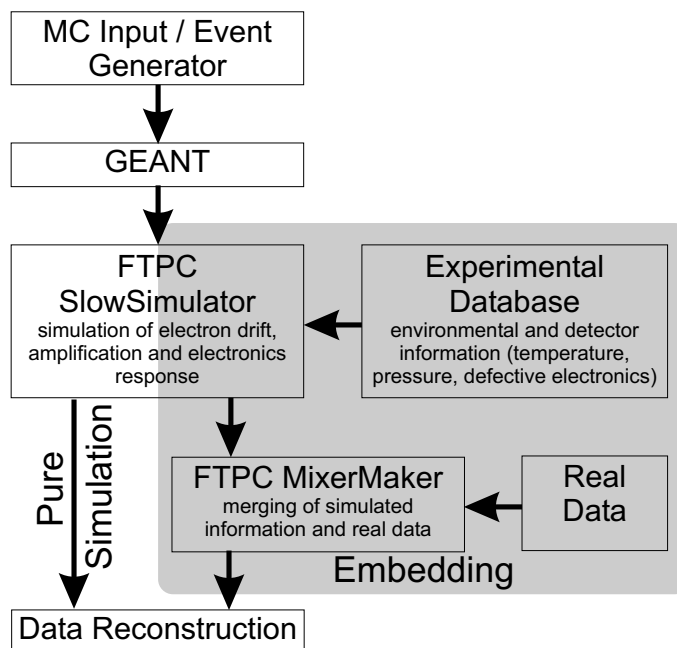


Figure 4.1: Flow chart of the FTPC simulation chain. For embedding simulations, the environmental parameters and possible defective electronics channels in the detector have to be taken into account.

4.1 Pure Simulations

Pure simulations do not merge simulated information with real data. They were used to study the detector performance in its design phase, and are still used to study physics performance with simulated events created by event generators such as HIJING, see section 3.4.4. They were also employed to investigate the consequences of geometric imperfections such as a displacement of the inner cathode. For a detailed discussion of the *FtpcSlowSimulator* framework and the simulation parameters used to describe the electron drift and the electronics response, refer to [38]. Within the scope of this thesis, the simulation of a displacement of the inner cathode, as observed in real data [21], and the correct treatment of temperature variations were included in the framework. In addition, a one-to-one reproduction of the zero suppression applied in the readout boards was added.

4.1.1 HIJING Simulations

HIJING is the most commonly used event generator for simulations of the STAR detector. For a more detailed description refer to section 3.4.4. It is a very useful tool to estimate detector performance since the particle multiplicity and the rapidity distribution generated by HIJING were found to be very realistic.

These simulation results have been used to study the efficiency and the momentum

resolution of the FTPCs as well as to estimate the influence of secondary interactions in the detector material on the particle spectra. They are also important for the determination of appropriate cuts for the search for neutral strange particles, see section 5.2.1.

4.2 Embedding

Without other detectors covering the same phase space as the FTPC, there is no direct measurement of detector parameters such as the efficiency and the momentum resolution. However, to be able to interpret the results, this information is necessary. The best way of obtaining these detector parameters is the embedding of simulated tracks into real events, thus creating tracks with known properties, but still affected by detector background.

The loss of electronics is expected to have a significant impact on the detector performance, so it is mandatory to include this information in the embedding simulation. Thus, the simulations use the same so-called gain table that is used for the reconstruction of the real data. The gain table contains information of the relative gain of each channel, and allows to deactivate dead and noisy channels in the analysis.

Depending on the nature of the effects under investigation, different particle and event types are embedded. For efficiency studies, the respective particle (π , Λ , K_s^0 , Ξ) is embedded into minimum bias events. To study the influences from beam background and track pileup from other events, HIJING events are embedded into zero bias data. This zero bias data is taken with a random trigger while beams are stored in RHIC and produce collisions in the interaction region. Thus there is no correlation between the trigger time and the time an interaction took place. Zero bias events are a good representation of background not originating from the triggered event.

4.2.1 Gain Tables

The gain tables are determined in two steps. First, the relative gain of the different channels has to be measured. For this, pulser runs are analyzed. In these runs, the Frish grid of the detector is pulsed with a rectangular signal. The rising edge of the signal induces charge in the readout pads. The response of the electronics to this signal is recorded. By comparing the pulse height of the induced pulse on one channel with the mean of all channels, the relative gain is determined. Dead channels show no response, so they can also be identified.

Typically, the pulse induced by the pulser is a short, high pulse, corresponding to several minimum ionizing particles. It was observed that often the noise introduced

by a faulty chip is not visible in these runs. To identify channels that have a high noise and thus should be excluded in the data analysis, real data is used. By summing up the entries over all time bins for each channel and forming an average over many events, noisy channels show up via significantly higher counts. This method is especially reliable in low multiplicity events, such as d+Au collisions, but was also successfully applied to Au+Au collisions. The threshold for noisy channels changes from run to run, since the average count rate depends on the beam parameters, so it has to be adjusted for each run that is used to create a gain table. So far, this is not done automatically, since correct performance has to be insured by inspecting the noise level for each analyzed run. Channels above the threshold are deactivated in the gain table, and thus will be ignored for the reconstruction.

Apart from this main application of the gain tables, they are also used to localize defective front end chips. The front end cards hosting these chips are then replaced during shutdown periods. Currently, front end cards with more than 8 defective channels (out of a total of 64, distributed over 4 chips) are replaced. In the future, more broken channels might have to be tolerated, because of the limited number of spare cards and front end chips available for replacement.

4.2.2 The Embedding Procedure

The production of embedding files is carried out by a highly complex software framework at the PDSF computing facility in Oakland, California. Here, the basic steps in that process are described, highlighting the FTPC specific tasks.

In order to obtain all necessary parameters for creating the Monte Carlo tracks, such as the position of the event vertex and the event multiplicity, a full reconstruction of the used data is necessary as a first step. Then, a file containing the simulated information of all events for embedding is created. In this second step, tracks that originate from the reconstructed primary vertex are simulated. In order not to change the event characteristics in a significant way by the addition of the simulated particles, 5% of the real event multiplicity, but at least one track per detector, is embedded. In the case of zero bias events usually no primary vertex exists. Into these events, complete HIJING events are embedded, as discussed above. The event vertex is given by the vertex of the HIJING event which is randomly distributed. The embedded multiplicity is given by the event generator. The simulated tracks are passed through the GEANT detector simulation to obtain the charge deposited in the detector.

To produce the output, namely the reconstructed tracks, the reading of the real data and the simulation of the detector response to the charge deposit given by GEANT have to be handled simultaneously. This ensures that the data base information

on relevant detector and environmental parameters such as the correct gain table, the gas temperature and the pressure are available for the simulation. Then, the already mentioned *StFtpcMixerMaker* merges the simulated charge with the real data information for each pad timebin by timebin. After the merge, the zero suppression parameters used in the readout boards are applied. The output of this program can be treated just like real data, and passed to the standard reconstruction chain. Here, the primary vertex is fixed to the position obtained in the previous reconstruction pass to avoid possible shifts due to the added simulated tracks. In addition to the reconstructed information, data from the Monte Carlo input is written out to allow matching of simulated and reconstructed tracks, and thus a study of the momentum resolution and the efficiency, described further down.

4.2.3 Comparison to Data

To judge whether the detector parameters obtained with embedding are realistic enough for the correction of results, some basic properties of embedded data have to be compared to real data.

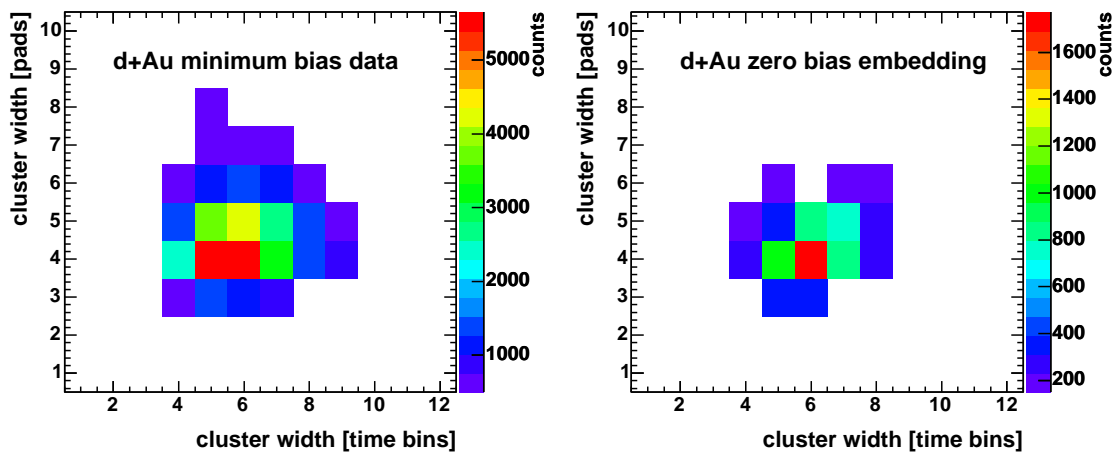


Figure 4.2: Cluster size in time and pad (r and φ) direction for real data (left) and d+Au HIJING zero bias embedding (right) from FTPC W.

Figure 4.2 shows the size of the reconstructed charge clusters in the time (radial) and pad (azimuthal) direction for both real data and embedding. Here, the embedding of HIJING events into zero bias data is used to get mainly simulated charge clusters with a realistic background. It is apparent that while the embedding reproduces the mean size of the clusters quite well, the variations in both pad and time direction are underestimated. This leads to an overestimation of the position resolution for individual hits in the simulation. It is expected that this does not affect the track

reconstruction efficiency significantly, but might lead to an underestimation of the distance of closest approach (dca) to the primary vertex for the simulated tracks.

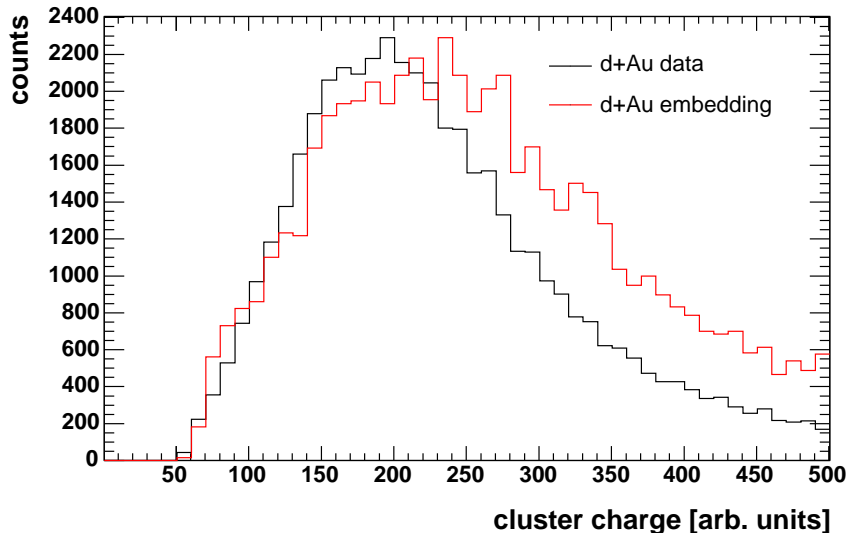


Figure 4.3: Cluster charge in real data and zero bias embedding, shown for FTPC W. The histogram with the embedding data is scaled to reach the same maximum as the real data histogram.

Figure 4.3 shows the reconstructed cluster charge for real data compared to that for d+Au zero bias HIJING embedding. In general, there is quite good agreement between real data and simulation. The mean charge of simulated hits is about 10% higher than the real one. This is due to slightly high amplification values in the simulation.

From the two comparisons of cluster properties it is apparent that while the embedding simulation shows a fair overall agreement with real data, there are nevertheless some discrepancies. The cluster shape does not vary enough, pointing to a "too perfect" shape in the simulations. The charge is slightly too high, a consequence of an overestimation of the amplification parameters.

For a comparison of the properties of simulated and real tracks the number of hits on track is studied, as shown in figure 4.4.

For this comparison, FTPC W in the pseudorapidity range $3.0 < \eta < 3.5$ is used. This excludes areas at the edge of the detector acceptance where hits might get lost. For the real data, tracks with a dca to the primary vertex smaller than 3 cm are selected. For the embedding dataset, π^- embedded into d+Au minimum bias events are used.

It is apparent that the simulations overestimate the percentage of tracks that reach the maximal possible number of hits of 10. This is probably caused by an incomplete exclusion of dead and noisy detector areas and the overestimation of the cluster

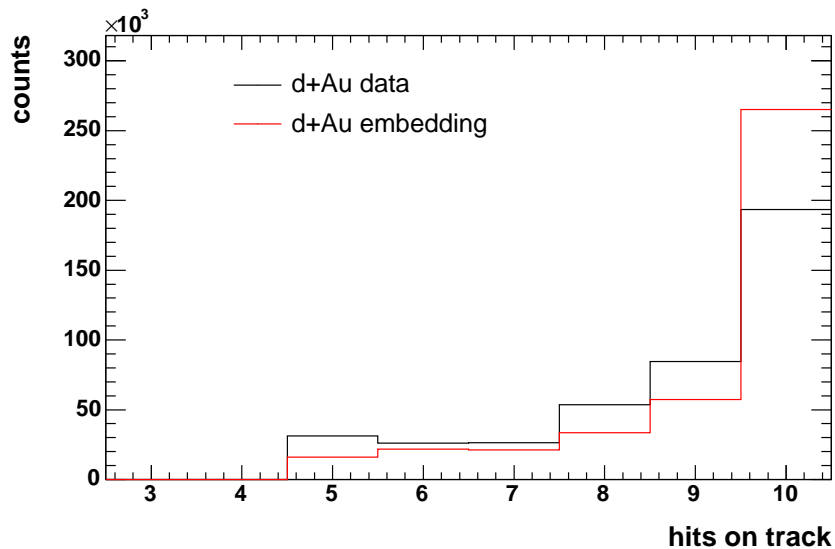


Figure 4.4: Number of hits on track for real data and for embedded π^- . Tracks in the pseudo-rapidity range $3.0 < \eta < 3.5$ in FTPC West are used. The histogram for the embedding data is normalized to the integral of the histogram for real data.

quality discussed above. Consequently, the amount of tracks with less than 10 hits is underestimated. However, the general shape of the distribution of the number of hits on track is still reproduced.

Again, the general trend of the behavior of tracks in real data is reasonably reproduced in the simulations. However, the track quality is overestimated. A consequence of this is that additional corrections for the track quality have to be applied to correction factors determined using simulated data, as discussed in section 4.4.

4.3 Tracking Efficiency and Momentum Resolution

4.3.1 Matching of Reconstruction and Simulation

To study the efficiency and the momentum resolution of the detectors with the simulations, a matching of the simulated and the reconstructed tracks is necessary. This is done by a tool called *StAssociationMaker*. The matching happens in two steps. First, for each reconstructed hit, all Monte Carlo hits within a detector dependent window are associated to that hit. Then, for all hits on a reconstructed track, the simulated hits associated with their respective mother tracks are analyzed. If a Monte Carlo track has more than a detector specific number of hits in common with

the reconstructed track, it is stored as an associated track. Note that one reconstructed track can have more than one associated track. Likewise, one simulated track can be associated to more than one reconstructed track. Table 4.1 summarizes the parameters used for the association of FTPC Monte Carlo information.

| | |
|---|----------------|
| radial distance (mc hit - reconstructed hit) | ≤ 3 mm |
| azimuthal (φ) distance (mc hit - reconstructed hit) | $\leq 2^\circ$ |
| number of common hits of mc and reconstructed track | ≥ 3 |

Table 4.1: Association parameters for simulated FTPC information.

The table of associations is then used by the *StFtpcMcAnalysisMaker*, developed by the author. This program filters out the FTPC relevant information and resolves ambiguities due to multiple associations. For the study of hits, only the best association, defined as the closest Monte Carlo hit, is used. Likewise, for the tracks the association with the highest number of common hits is chosen. Care has to be taken to avoid selection of the same track more than once. In addition to the association of individual tracks, the *StFtpcMcAnalysisMaker* also associates reconstructed daughter tracks of selected particle decays to the respective original particle. Thus, a link from the reconstructed tracks to the not directly detectable mother particle is established. The resulting FTPC specific association information is stored in a separate file for fast subsequent analysis.

4.3.2 Tracking Efficiency

The tracking efficiency of the detectors is determined by dividing the number of reconstructed tracks within a certain kinematic (η , p_t) window by the number of Monte Carlo tracks that were simulated in that same window. Figure 4.5 shows the efficiency for both FTPCs obtained from embedding positive pions with a flat p_t spectrum into d+Au minimum bias events. A cut on the position of the event vertex along the beam line of ± 50 cm from the nominal interaction point is applied to ensure a reasonable uniformity of the detector response.

In the region $2.8 < |\eta| < 3.8$ the detectors reach a fairly constant efficiency which exceeds 80%. This includes the contribution from the dead areas at the sector boundaries. Above 0.2 GeV/c the efficiency is constant as a function of transverse momentum.

In general, the detector efficiency depends on the particle multiplicity of the event. In higher multiplicity environments, the hit and track reconstruction becomes increasingly difficult, leading to a decrease in the efficiency. In d+Au collisions, the multiplicity is so low that these effects do not come into play. In Au+Au collisions on the other hand, the multiplicity dependence of the efficiency has to be taken into

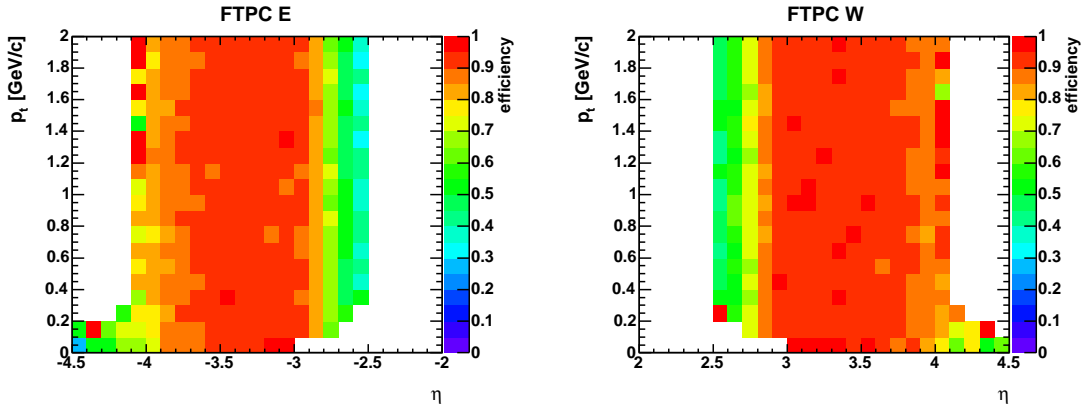


Figure 4.5: Efficiency obtained from embedding π^+ into d+Au minimum bias events. It is apparent that the efficiency in FTPC W is slightly higher than in FTPC E. This is due to more defective electronics on the East side.

account. In addition, for the Au+Au data taking in 2001/2002 the detectors were operated at lower amplification voltages and thus lower gain. This led to further decrease in reconstruction efficiency. By adjusting the amplification parameters used in the simulation this decrease in efficiency can be reproduced. Thus embedding simulations can be used to obtain the necessary correction factors, as discussed in detail in [21].

Efficiency corrections obtained by using the embedding procedure described here have been used to correct the charged hadron spectra in Au+Au collisions and in d+Au collisions at $\sqrt{s_{NN}} = 200$ GeV, presented in [21]. The charged hadron spectra show good agreement with the results from two other RHIC experiments, BRAHMS and PHOBOS. This demonstrates that the embedding procedure provides a good description of effects influencing the track reconstruction efficiency.

4.3.3 Momentum Resolution

The momentum resolution Δp_t of the detectors is defined here as the width σ of a gaussian fit to the distribution of the difference of reconstructed and simulated p_t divided by the simulated p_t ,

$$\Delta p_t = \sigma \left(\frac{p_{t, reco} - p_{t, mc}}{p_{t, mc}} \right).$$

Figure 4.6 shows the p_t resolution obtained from embedding as a function of pseudorapidity and transverse momentum for primary tracks, where the event vertex is included in the fit. Tracks from FTPC West with $2.8 < \eta < 3.8$ and $p_t < 2$ GeV/c are used. The resolution deteriorates with increasing pseudorapidity and increasing p_t . Since these one dimensional plots average over the other coordinate (either

p_t or η), they show a mean resolution. At low η and p_t , a resolution as good as 10% is achieved. At high momentum and high η , tracks where the charge sign was not correctly determined start to contribute. For these tracks, the momentum reconstruction fails completely.

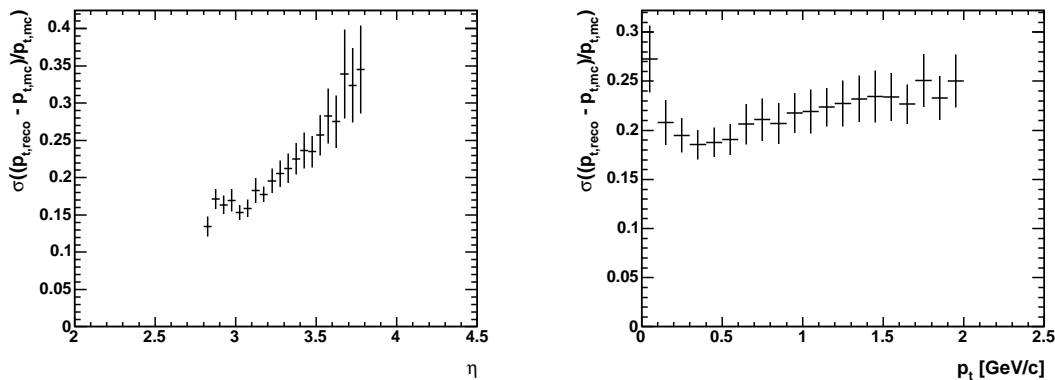


Figure 4.6: Resolution of transverse momentum as a function of η and p_t from embedding of π^+ with a flat p_t spectrum into d+Au minimum bias events in FTPC West.

A detailed discussion of simulation studies on momentum resolution and detector efficiency using HIJING generated events can be found in [22].

4.4 Limitations

Although simulations with correct treatment of faulty electronics channels reproduce the angular track distributions and the overall tracking efficiency quite well, there are limitations in the accuracy that affect analysis.

Geometric imperfections in the detector such as a shift of the inner cathode are observed and corrected for in first order in the reconstruction. In simulations, these distortions (and possibly other undetected effects) are not present. It has been shown that the influence of these distortions on momentum resolution is quite small on average. However, distortions will lead to less precision in the track reconstruction, and thus to a broadening of the distribution of the distance of closest approach dca to the primary vertex.

It is also observed that the cluster geometry in simulations is closer to a perfect shape than in reality. Again, this leads to a higher track precision in simulations compared to real data. Also the average number of hits on a track is overestimated in the simulations. This overestimation of the track precision influences the dca to the primary vertex and the distance of tracks of decay daughters at the decay vertex.

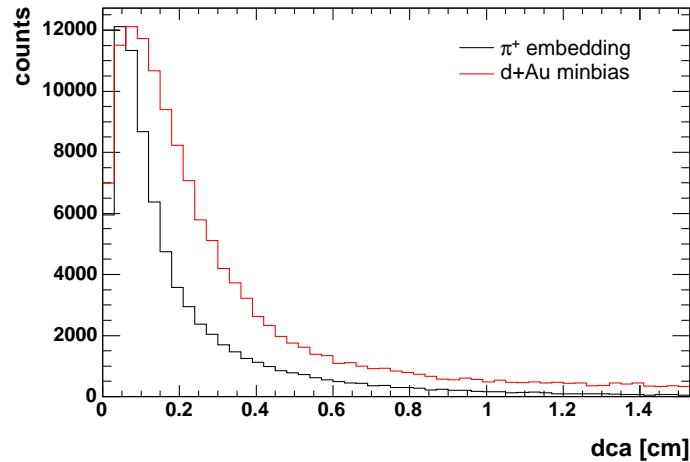


Figure 4.7: Distance of closest approach of tracks to the primary vertex for embedded π^+ and real data. The histogram for real data has been scaled to reach the same maximum as the histogram from simulation. The mean dca for real data is about twice the mean of the dca for embedded tracks. However, the real data also contain secondary particles, while in simulations, only particles originating from the primary vertex are present.

Figure 4.7 shows the dca to the primary vertex in the FTPCs for positive pions from embedding and charged hadrons from real data. It is apparent that the dca distribution for data is considerably wider. However, it has to be taken into account that in the embedding simulations, all particles originate from the primary vertex, while the data also contains secondary particles that naturally have a larger dca.

As a consequence, when dca cuts are applied in the analysis, the effects of these cuts on the simulation and on data have to be compared. If differences due to an underestimation of the dca in simulations are apparent the embedding results used for efficiency determination have to be corrected for this dca broadening. This is illustrated in section 5.6.1.

Chapter 5

Data Analysis and Corrections

Specialized analysis tools have been developed to identify neutral strange particles at forward rapidity via their displaced decay vertices. In addition, a simulation framework based on the embedding of simulated particles into real events was devised to determine the corrections for reconstruction efficiency and detector acceptance. The analysis discussed here uses the tracks from the two FTPCs. The main aim is the reconstruction of Λ and $\bar{\Lambda}$ particles on both sides of the asymmetric d+Au collisions. Since background contributions from K_S^0 decays are taken from HIJING simulations, the reconstruction of K_S^0 on the deuteron side is used to verify the HIJING predictions.

5.1 Properties of Λ Particles and their Decay Signatures

The Λ is a singly strange baryon with the quark composition uds . It decays weakly, the predominant and detectable decays into charged particles being

$$\Lambda \rightarrow p \pi^- \qquad \bar{\Lambda} \rightarrow \bar{p} \pi^+$$

with a branching ratio of 64%. Other decay modes include the decay into neutron and π^0 and much rarer semi-leptonic decays. The lifetime is 2.6×10^{-10} s, corresponding to a $c\tau$ of 7.9 cm.

These properties lead to a distinct signature of Λ decays in the detector, namely two oppositely charged tracks originating from a common point which is displaced from the event vertex. This is exploited for Λ detection and applies also to other neutral particles such as the K_S^0 . Conventionally, particles with these signatures are called V0.

5.2 Analysis Method

To extract a sample of Λ candidates, all positive tracks are combined with all negative tracks in the same event. This is done for both FTPCs independently, since the small opening angle of the decay daughters excludes the possibility that one decay daughter ends up in one FTPC while the other one is recorded in the other. As it is not possible to identify particles via their specific energy loss in the FTPCs, all positives are assumed to be protons and all negatives are assumed to be pions for the case of Λ , while for $\bar{\Lambda}$ all positives are treated as pions and all negatives as anti-protons.

In order to reduce the number of possible pairs, some cuts are applied to the tracks that go into the analysis, as discussed in subsection 5.2.1. These pairs are treated as possible Λ candidates, and additional properties are determined, such as the invariant mass, the decay length, the distance to the primary vertex and the rapidity. To improve the signal to background ratio, cuts are applied to some of these variables.

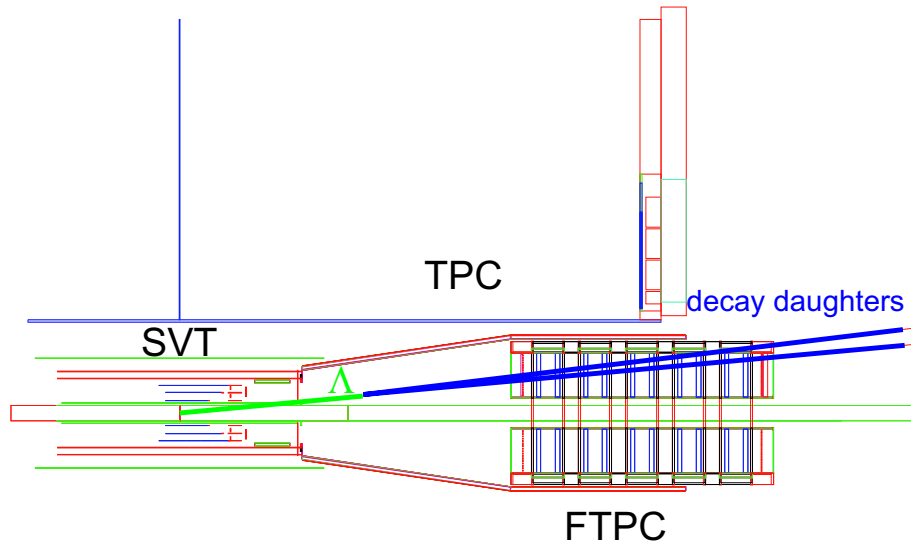


Figure 5.1: Simulated Λ decay in the forward rapidity region. Both daughter tracks are within the acceptance of the FTPC. In addition, part of the main TPC and of the SVT as well as the beam pipe are shown.

Figure 5.1 shows a simulated Λ decay in the forward TPC without any other tracks from the event. The Λ originates from the nominal interaction point and decays before reaching the active volume of the detector. Both charged decay daughters are within the active volume of the FTPC and can be reconstructed.

5.2.1 Analysis Cuts

Here, an overview is given over the cuts that are applied in the analysis. Most are geometric cuts that exploit the decay signature of the Λ . The distributions of the variables for which cuts are applied are illustrated for Λ decays taken from HIJING simulations. The simulations are used to obtain a reasonable range for the cuts. With studies on real data and on HIJING simulations an optimized set of cuts is determined.

The track quality is determined by the number of hits on a given track, so only tracks above a minimum number of hits are used in the analysis. On the other hand, defective electronics reduce the number of hits, so a compromise has to be found between quality and efficiency. The comparison of embedding simulations and real data presented in section 4.2.3 suggests that a minimum of 8 hits per track should be an acceptable choice.

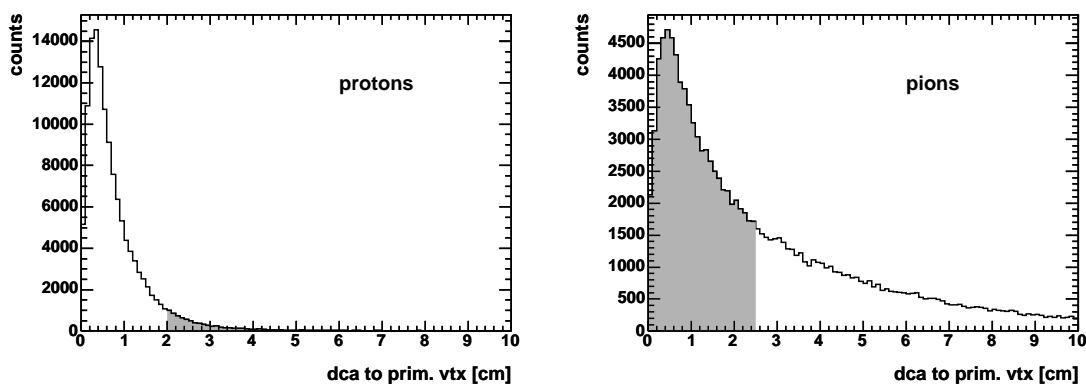


Figure 5.2: Distance of closest approach to the primary vertex for daughter particles of Λ decays, taken from HIJING simulations. The asymmetry of the decay is apparent in the dca distributions. The region rejected by the cut is shaded. Note that on the pion dca, a stricter cut is applied for FTPC East.

Since the proton is much heavier than the pion ($m_p = 938 \text{ MeV}/c^2$, $m_\pi = 140 \text{ MeV}/c^2$), the proton carries most of the momentum after the decay. Thus, it still points roughly in the same direction as the original Λ . The pion however receives a smaller fraction of the Λ momentum and will in general be emitted at an angle to the Λ direction. As a consequence, when extrapolating the track helices back towards the primary vertex, the proton seems to originate from the event vertex, while the pion does not. This can be exploited by cutting on the distance of closest approach to the primary vertex, the dca of the daughter tracks. For proton candidates a dca smaller than a certain value is required, while for pion candidates, a dca bigger than a threshold is requested. These cuts are very important in reducing the number of tracks that go into the analysis, and thus provide a powerful tool for background

rejection. The dca distributions of protons and pions from simulated Λ decays are shown in figure 5.2.

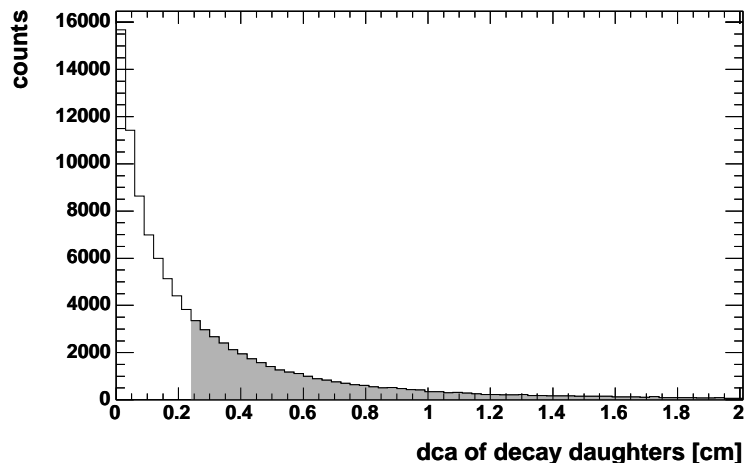


Figure 5.3: Distance of closest approach of decay daughters at the decay vertex in simulated Λ decays. The shaded area marks the entries rejected by the cut.

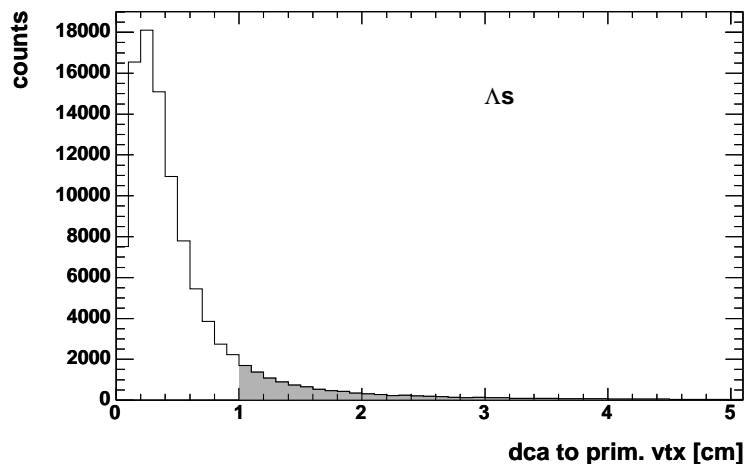


Figure 5.4: Distance of closest approach of reconstructed Λ to the primary vertex.

The two decay particles originate from one common point, so the tracks should meet when extrapolated back toward the decay vertex. In reality however the spatial resolution of the detector and the extrapolation lead to a finite distribution of the distance of closest approach of the two tracks, referred to as the daughter dca. Its distribution is shown for simulated Λ in figure 5.3. A cut helps to reject random pairs of tracks and is especially important in high multiplicity environments. The

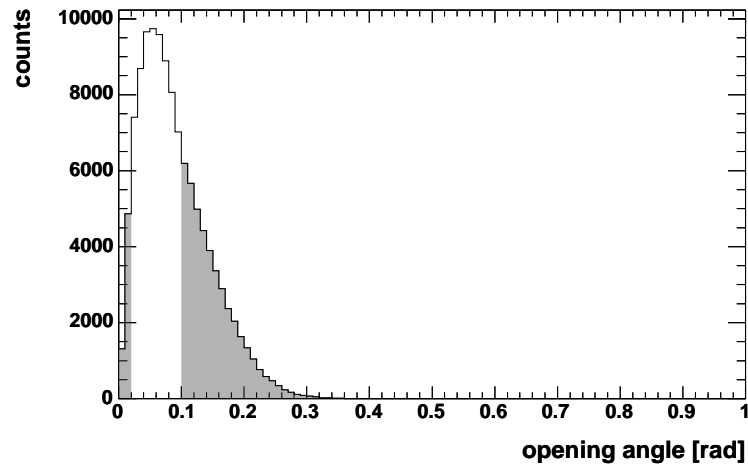


Figure 5.5: Opening angle of Λ and $\bar{\Lambda}$ decay daughters in HIJING simulations. The ranges rejected by the cut are shaded.

decay vertex is defined as the point halfway between both tracks at their points of closest proximity.

If the two tracks in a Λ candidate pair originate from the decay of a primary particle, their combined momentum has to point back to the event vertex. By cutting on a maximum candidate dca, background from false pairs can be reduced. Figure 5.4 shows the dca distribution of reconstructed primary Λ hyperons taken from HIJING simulations.

Background tracks that pass the dca cuts often originate from interactions in the beam pipe or in detector material. These tracks usually have a low transverse momentum and a large angle to other tracks in the events. By cutting on the opening angle of the particle pair, defined as the angle between the two decay daughters, this background can be largely eliminated. Also tracks that are almost parallel and form a random pair in an environment of high particle density can be rejected by requiring a minimum opening angle for a V0 decay. Figure 5.5 shows the opening angle of all reconstructed Λ and $\bar{\Lambda}$ in HIJING simulations.

As most tracks in an event originate from the primary vertex, demanding a clear separation of the decay vertex from the primary vertex by requiring a minimum decay length of the Λ candidate can help to reduce background. However, the dca cut on the pion candidate also favors large decay lengths, so that an additional cut on the decay length itself has only a small impact. Figure 5.6 shows the decay length of Λ taken from HIJING simulations. Due to the high momentum in the forward rapidity region, the distance traveled before decay can reach large values.

Figure 5.7 illustrates the cuts that are used in the analysis. The limited momentum resolution of the FTPCs requires strict cuts to control the background. This leads to

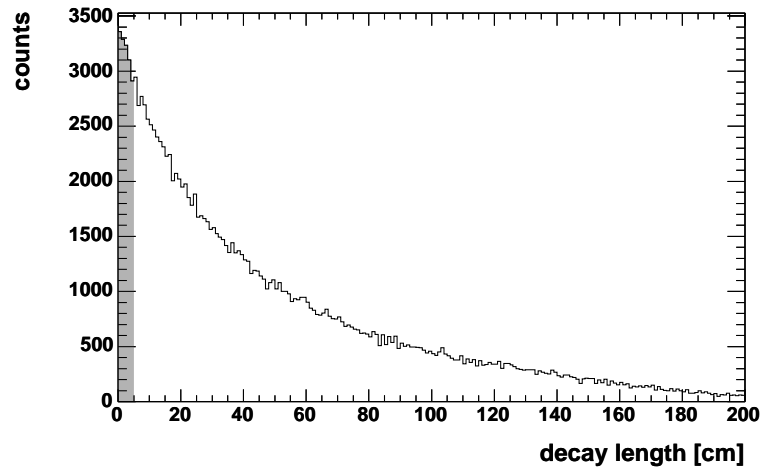


Figure 5.6: Decay length of simulated Λ . Values which are rejected by the cut are shaded.

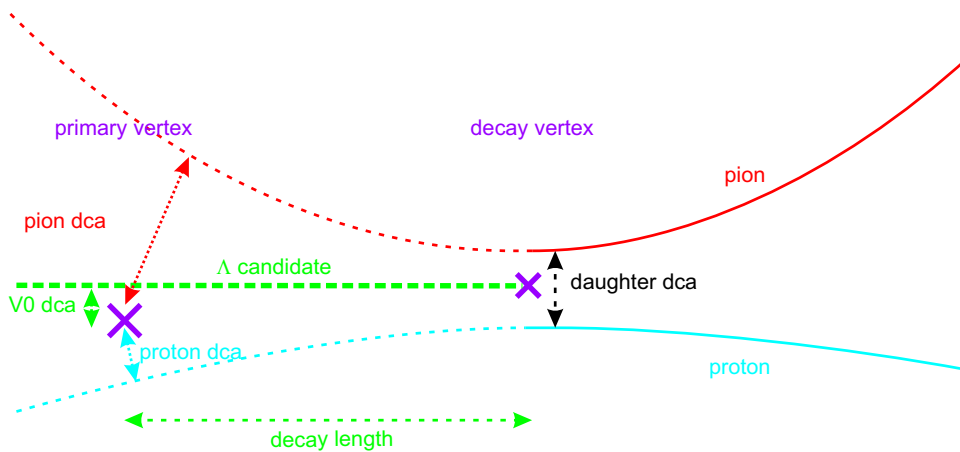


Figure 5.7: Illustration of cut parameters for the Λ decay.

a low overall efficiency that has to be determined from simulations. Taken together, the cuts allow the extraction of a satisfactory signal.

The cuts have been optimized with studies on real data and on HIJING simulations. This was done by varying the cut parameters while observing the effects on the stability of the results. From the simulations, initial values for this process were obtained since there the number of Λ and $\bar{\Lambda}$ is known. Due to the higher particle multiplicity on the East side, a slightly tighter cut on the dca of the pion is used to achieve optimal background rejection. All other cuts are equal for East and West. Table 5.1 summarizes the cut parameters used in the present analysis.

| cut parameter | cut value |
|--------------------------|---------------|
| number of hits per track | > 7 |
| proton dca | < 2.0 cm |
| pion dca | East > 3.0 cm |
| | West > 2.5 cm |
| dca of daughters | < 0.25 cm |
| dca of V0 candidate | < 1.0 cm |
| opening angle | > 0.02 |
| | < 0.1 |
| decay length | > 5.0 cm |

Table 5.1: Cut Parameters for Λ analysis in the forward TPCs.

5.2.2 Background Subtraction

The short-lived species of the neutral Kaon, K_S^0 , possesses similar decay signatures as the Λ . It decays predominantly (branching ratio 69 %) into two charged pions with a $c\tau$ of 2.7 cm.

$$K_S^0 \rightarrow \pi^+ \pi^-$$

The K_S^0 decay also leads to a separated decay vertex with two oppositely charged particles originating from it. Since particle identification is not possible in the FTTPCs, this decay is a priori not distinguishable from a Λ decay. However, due to the shorter lifetime and the symmetry of the decay, many K_S^0 will be rejected by the geometric cuts. The number remaining after application of all cuts can be estimated from simulations with the HIJING event generator and subtracted from the signal. The contributions taken from HIJING are verified on the deuteron side by analyzing the K_S^0 yield, as discussed in section 5.8.

Additional combinatoric background from random track pairs might still be present in the signal. Studies with mixed-event background, which uses tracks from different events to remove the signal but still containing random pairs, and track rotations, where either the positive or the negative tracks in one event are rotated to destroy the correlations, have been performed. Due to the limited mass resolution, given by the momentum resolution of the detector, no reliable background normalization could be performed. The analysis of HIJING-generated events suggests that with the strict cuts employed, the contribution of random pairs to the signal is below 5%. This contribution is included in the systematic errors.

5.3 Expected Performance

From the embedding studies and simulations, the performance of the Λ reconstruction can be estimated, since an unambiguous identification of decay daughters is possible with the matching of reconstructed and simulated tracks discussed in section 4.3.1.

By calculating the invariant mass of fully reconstructed decay daughter pairs an estimate for the invariant mass distribution can be obtained. Figure 5.8 shows the distribution for associated Λ obtained from HIJING simulations without the application of analysis cuts.

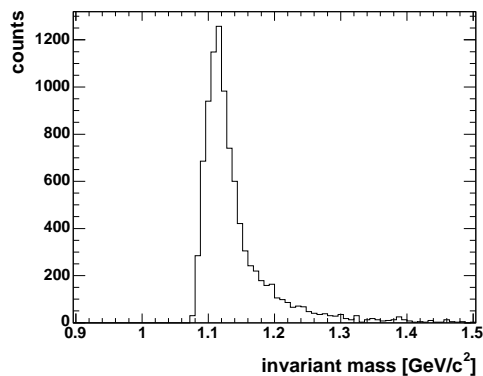


Figure 5.8: Λ invariant mass distribution obtained from HIJING events passed through the full detector simulation.

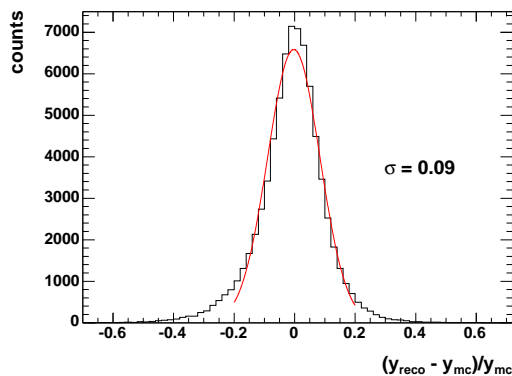


Figure 5.9: Rapidity resolution for reconstructed Λ . Obtained from embedding with a realistic temperature parameter and all analysis cuts.

For the reconstruction of Λ particles track parameterisations that are fitted without the primary event vertex are used. Thus only moderate momentum resolution can be reached. It was determined to be of the order of 20%.

As a strong rapidity dependence of strangeness production in the FTFC region is predicted by some models, a reasonable rapidity resolution is important. It is influenced by the momentum resolution and the determination of the track angle, which is related to the resolution in pseudorapidity. The latter is very good in the FTFCs, so that a sufficient resolution in rapidity of better than ± 0.3 can be achieved at a rapidity of 3, as shown in figure 5.9.

5.4 Acceptance

The geometric acceptance of the FTFCs in pseudorapidity is constant as a function of transverse momentum, since the pseudorapidity depends only on the emission

angle of the particle. However, the rapidity is the real physical variable of interest, and also used in model calculations. Thus, the rapidity will be used in the analysis. Since the rapidity depends not only on the emission angle, but also on the particle momentum, the acceptance in rapidity y of the detectors is not constant as a function of p_t .

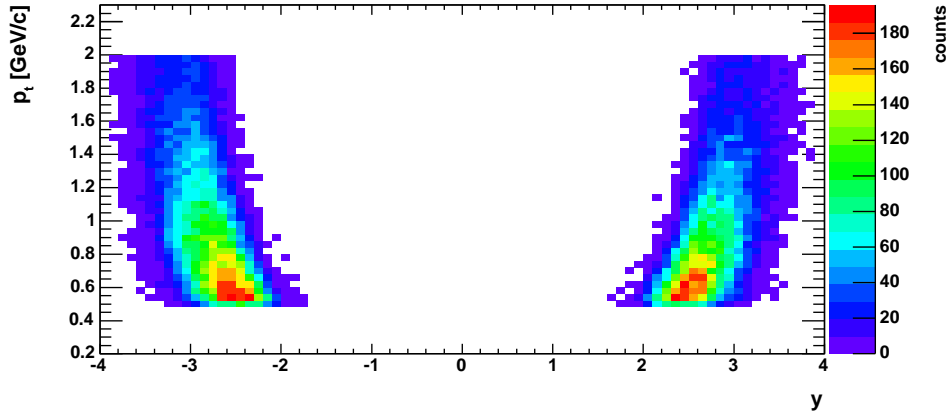


Figure 5.10: Acceptance for Λ candidates in both detectors. For the analysis, the y range $2.5 < |y| < 3.0$ is selected which is covered over the p_t region from 0.5 GeV/c to 2 GeV/c.

Figure 5.10 shows the transverse momentum and the rapidity for all Λ candidates in the FTPCs. Since a strong rapidity dependence of the observables is expected, a limited range in rapidity that is covered at all p_t is used in the analysis. The momentum and charge sign resolution deteriorates at high p_t and high η , so a rapidity range is chosen where the high p_t tracks are mostly in the low η region of the detector, to ensure the best possible resolution. This leads to the choice of $2.5 < y < 3.0$ for the analysis.

The mean of the rapidity distribution within the accepted window changes over the used momentum range. At low p_t , the mean rapidity is lower than the average $\langle y \rangle = 2.75$, while at high p_t it is higher. The variation over the whole range is about 0.12 units in rapidity, from 2.69 to 2.81 for a mean p_t from 0.6 GeV/c to 1.6 GeV/c.

5.5 Invariant Mass Distributions

The invariant mass is a good indicator of signal quality. For the Λ , the width of that distribution is determined entirely by the detector resolution. The expected shape of the distribution is shown in figure 5.8.

Figure 5.11 shows the invariant mass distributions for Λ and $\bar{\Lambda}$ candidates in both FTPC West and FTPC East. The distributions are obtained from the whole d+Au

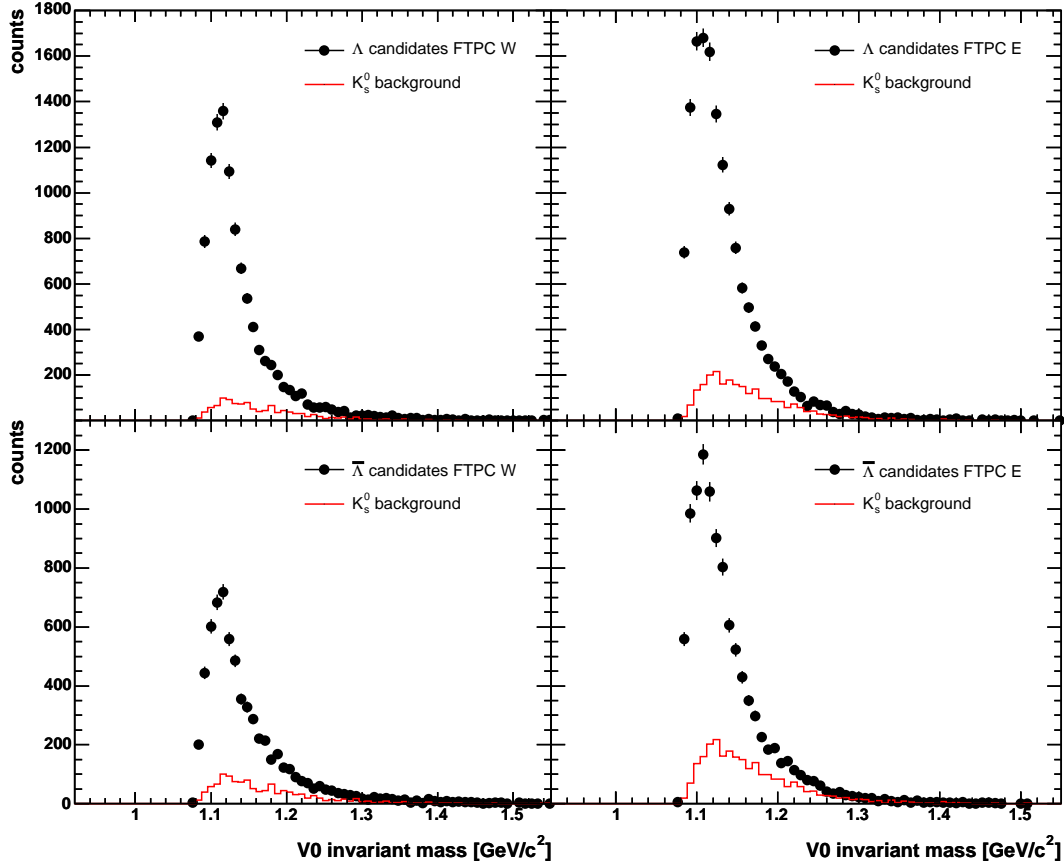


Figure 5.11: Invariant mass distribution for Λ and $\bar{\Lambda}$ candidates in both detectors. The distributions are shown together with the expected K_S^0 background obtained from HIJING simulations.

dataset using the cuts listed in table 5.1. Also shown is the background expected from K_S^0 decays. This contribution is taken from HIJING simulations.

The procedure of subtracting the K_S^0 background is applied to Λ and $\bar{\Lambda}$ candidates in both detectors. The resulting background subtracted distributions are shown in Figure 5.12. In general, the shape of the distribution agrees well with that expected from simulations, demonstrating that effects influencing the mass resolution are well reproduced. For the East FTPC on the Au side of the collision with the higher track multiplicity, the invariant mass distribution is shifted by $\sim 10 \text{ MeV}/c^2$ toward lower values. This shift is most prominent at low transverse momentum. Possible explanations are contributions from remaining background or reconstruction problems at low p_t due to electronics loss on the east side.

By fitting a gaussian in the region $1.08 \text{ GeV}/c^2$ to $1.16 \text{ GeV}/c^2$ and thus ignoring the asymmetry towards high mass, the mass can be determined. This can be used as an indicator of data and calibration quality. Table 5.2 summarizes the results of the fits to the background subtracted invariant mass spectra for both Λ and $\bar{\Lambda}$ in

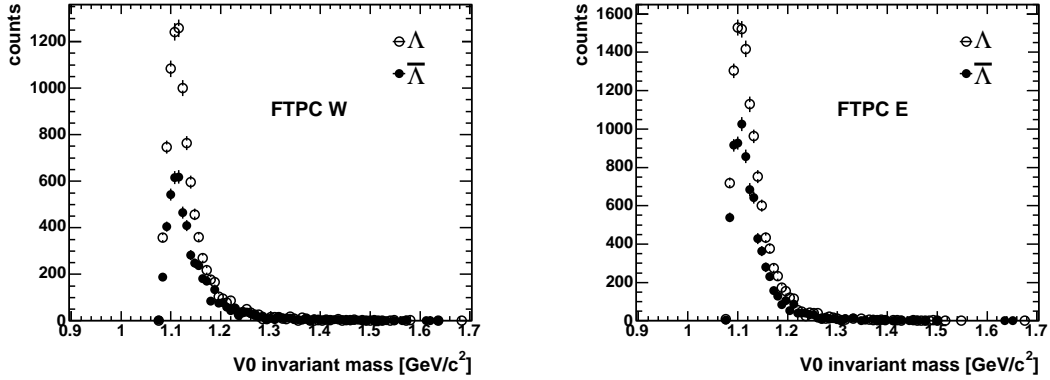


Figure 5.12: Background subtracted invariant mass plots for Λ and $\bar{\Lambda}$ in both forward TPCs.

both detectors.

| | mass [GeV/c ²] | σ [GeV/c ²] |
|-----------------------|----------------------------|--------------------------------|
| Λ West | 1.115 ± 0.001 | 0.023 ± 0.001 |
| $\bar{\Lambda}$ West | 1.115 ± 0.001 | 0.024 ± 0.001 |
| Λ East | 1.111 ± 0.001 | 0.026 ± 0.001 |
| $\bar{\Lambda}$ East | 1.108 ± 0.001 | 0.028 ± 0.001 |
| HIJING Λ West | 1.116 ± 0.001 | 0.022 ± 0.001 |

Table 5.2: Mass and width of Λ and $\bar{\Lambda}$ signals obtained by gaussian fits to the invariant mass distributions. As a comparison, the results of the same fit applied to the invariant mass distribution obtained from HIJING simulations is given. The literature value of the Λ mass is $1.1157 \text{ GeV}/c^2$.

The good overall agreement of the masses in FTFC West with the literature values and the equality of particle and antiparticle mass shows the good quality of the detector calibrations. The discrepancy in FTFC East has been discussed above.

From the background subtracted invariant mass plots, the particle yield can be extracted either by fitting the signal with a function or by summing up the entries in the bins in the signal region. Since the shape of the invariant mass distribution does not follow a simple function, the latter method is chosen here. The yield is determined by summing up all bins from $1.08 \text{ GeV}/c$ to $1.24 \text{ GeV}/c$.

5.6 Corrections

In order to obtain results for physical quantities, the data have to be corrected for the detector and analysis efficiency and for the feeddown from the decay of higher

mass particles. For a measurement of the $\bar{\Lambda}/\Lambda$ ratio, it is sufficient to ensure that the efficiency is equal for $\bar{\Lambda}$ and Λ , as long as feeddown effects are ignored.

In this section, the corrections that are applied to the data are discussed.

5.6.1 Efficiency

The efficiency for the reconstruction of Λ and $\bar{\Lambda}$ is determined by using the embedding framework described in section 4.2. This is done in two steps. First, Λ and $\bar{\Lambda}$ with a flat p_t distribution from 0 to 2 GeV/c are embedded into d+Au minimum bias events. To keep the number of needed events in a reasonable range, 5 particles per detector are embedded into each event. Since the simulated particles are spread in rapidity, azimuth and momentum this does not lead to ambiguities during reconstruction. The decay of the embedded Λ is forced to be into proton and pion, to avoid wasting of resources for particles that cannot be reconstructed. These events are analyzed with the same code that is used for the analysis of real data. The number of reconstructed Λ is then compared with the number of particles extracted from the Monte Carlo input information of the events. From this, the efficiency as a function of p_t can be extracted. This number has to be corrected for the branching ratio of the decay and for deviations of simulations from real data.

The real events that are used for embedding of course also contain Λ and $\bar{\Lambda}$, which will also be reconstructed, and thus lead to an artificial increase in the efficiency. However, the ratio of embedded to original Λ is in the order of 50, so that this effect is negligible within the errors of the efficiency study.

In principle, the real efficiency for a physical momentum distribution of the particles can be determined from the flat p_t embedding. To do this, smearing due to the limited momentum resolution of the detector has to be taken into account. In reality, the number of particles decreases strongly with increasing transverse momentum, so that a finite momentum resolution leads to a flattening of the spectrum. This can be taken into account by bin-by-bin weighting, or by embedding particles with a physical p_t distribution. The latter is done in the second step of the efficiency determination. To do this, the distribution that should be used has to be determined. It can be shown that, based on the boost invariance of the production cross section for hadrons and a thermal p_t distribution, the spectrum is described to a good approximation by an exponential function in transverse mass m_t [39]. Such a distribution is described by a temperature parameter T ,

$$\frac{1}{2\pi m_t} d^2N/dy dm_t = C e^{-m_t/T} \quad (5.1)$$

where $d^2N/dy dm_t$ is the mean double differential particle yield per event and C is a normalization constant.

This temperature T is extracted from the real data by fitting the m_t distribution of all candidates that pass the cuts after correcting this distribution for the efficiency as a function of m_t , extracted from the flat p_t embedding. It is expected that the temperature parameter at forward rapidity in RHIC is comparable to the mid-rapidity temperature at SPS, since it has been observed that the mean transverse momentum of charged particles in Au+Au collisions at forward rapidity at RHIC matches that at mid-rapidity in Pb+Pb collisions at SPS [40]. In d+Au collisions a slightly lower temperature parameter than in Au+Au or Pb+Pb collisions is expected due to the absence of large contributions from collective flow effects. This has to be taken into account when comparing to the NA49 measurement in central Pb+Pb collisions [41]. From the transverse mass spectrum of the Λ candidates in FTPC West, a temperature parameter estimate of 230 MeV is derived.

With this temperature inserted into the distribution in equation 5.1, particles are embedded in the p_t range 0.2 GeV/c to 2.0 GeV/c. The efficiency is determined again and now contains the effects from momentum smearing. These values are then used to determine the particle yields.

Additional Corrections to the Efficiency

The efficiency determined from embedding is only correct if the distributions of variables that are cut on are comparable in simulation and real data. This is not always the case. Especially the dca distributions are wider in data than in simulations, as shown in section 4.4. This is probably due to the imperfect correction for distortions caused by the cathode shift and to an overestimation of cluster quality. This can be corrected for by studying the effect a change in the cuts has on embedded and on real data. Corrections have to be applied for the cut on the daughter dca and the cut on the candidate dca. For the default analysis cuts, this correction factor was determined to be 0.70 ± 0.05 .

Figure 5.13 shows a comparison of the Λ candidate dca obtained from data to the Λ dca in embedding with a realistic temperature parameter for FTPC West. It is apparent that while the cut applied at a dca of 1 cm does not reject a significant fraction of the simulated particles, a sizeable fraction of real data candidates is excluded. A similar effect is observed for the daughter dca distribution. Together, this leads to the correction factor discussed above.

5.6.2 Feeddown

The goal of the measurements is the determination of the yield of Λ particles produced in the collision. However, also Λ that originate from heavier hyperon decays are detected. These contributions are referred to as feeddown and have to be estimated and subtracted. All particles that have a Λ in their decay channel have

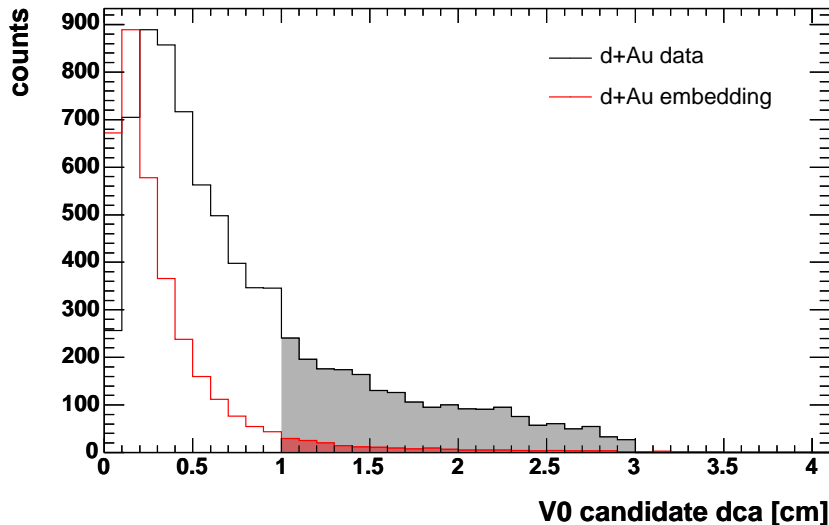


Figure 5.13: Comparison of Λ candidate dca in data with the Λ dca in embedding with a realistic temperature parameter for FTPC West. The embedding histogram is scaled to reach the same maximum as the histogram for data. The region excluded by the cut is shaded.

to be considered. Λ particles originating from strong resonance decays, such as $\Sigma(1385) \rightarrow \Lambda\pi$ are treated as primary Λ .

The biggest contribution is expected to come from the decay of the Σ^0 , which has the same quark content (uds) as the Lambda, but is in a different isospin state. This "heavier Λ particle" decays exclusively into a Λ and a photon,

$$\Sigma^0 \rightarrow \Lambda \gamma.$$

Since this decay is electromagnetic, the lifetime of the Σ^0 is very short ($\tau = 7.4 \times 10^{-20}$ s, $c\tau = 2.2 \times 10^{-11}$ m), so that there is no detectable vertex separation. Also, photons do not yield precise tracks, making a direct Σ^0 measurement very challenging. Based on the isospin of the Σ^0 , its contribution to the total Λ yield is expected to be of the order of 25%. So far, there are no measurements of the yield of this particle in heavy ion collisions, and thus the Σ^0 is counted as a Λ and not corrected for. This has to be taken into account when comparing to models.

A contribution of the order of 5% of the total Λ yield is expected from the doubly strange Ξ baryon. Here, there are two particles that decay into Λ (and their anti particles into $\bar{\Lambda}$), the Ξ^0 with the quark content uss and the Ξ^- with dss . Their decays

$$\Xi^0 \rightarrow \Lambda \pi^0 \qquad \Xi^- \rightarrow \Lambda \pi^-$$

are mediated by the weak interaction, leading to lifetimes comparable to that of the Λ . For the Ξ^0 , the lifetime is 2.9×10^{-10} s, $c\tau = 8.7$ cm, for the Ξ^- it is 1.6×10^{-10} s, $c\tau = 4.9$ cm.

Due to the limited momentum resolution of the FTTPC, the reconstruction of Ξ is not possible. However, at mid-rapidity, Ξ^- can be reconstructed in the main STAR TPC. A measurement of the Ξ^0 yield is not available, since it has the neutral π^0 in its decay channel, which decays into two photons and is hard to reconstruct precisely. Since the yield of the Ξ^0 is assumed to be the same as that of the Ξ^- , the Ξ^0 yield can be inferred from the Ξ^- measurement.

The preliminary yield ratio of Ξ^-/Λ at mid rapidity in d+Au collisions is 0.053 [42]. In p+p collisions, a yield ratio of 0.041 is observed [43].

The efficiency for the reconstruction of Λ originating from the decay of Ξ^- and Ξ^0 are determined from embedding of these particles into d+Au events. Differences to the efficiency for primary Λ are expected from three effects. The secondary particles do not point back to the primary vertex, leading to a lower efficiency caused by the cut on the particle dca. This effect increases with increasing lifetime of the parent particle, and thus is more pronounced for Λ originating from Ξ^0 decays. On the other hand, the additional flight distance of the Ξ increases the apparent decay length of secondary Λ and also increases the number of daughter pions that will pass the dca cut. This increases the efficiency. Since the Ξ^- decays into π^- and Λ , which in turn decays into p and π^- , there are two pions that might fulfill the required cuts and can be combined with the proton track to form a lambda candidate. This can lead to an artificial enhancement of the efficiency for secondary Λ originating from Ξ^- decays. It turns out that the efficiency for Λ originating from Ξ^0 decays is 83 % of the efficiency for primary Λ , while the efficiency for Λ from Ξ^- decays is 111 % of the primary efficiency. Since the number of Ξ^0 is equal to that of Ξ^- , the averaged efficiency is almost the same as for primary Λ .

Still, assumptions have to be made concerning the rapidity dependence of the Ξ/Λ ratio. Measurements of hyperon yields as a function of rapidity are only available at lower energy from the NA49 experiment [44]. Figure 5.14 shows the rapidity dependence of the Ξ^-/Λ and of the Ξ^+/Λ ratio obtained from HIJING calculations. The rapidity acceptance of the main TPC and the FTTPCs is highlighted. Since most of the Ξ s are pair produced, the assumption that the ratio does not change with rapidity works well for the anti-particles. For the particles, there are significant contributions from associated production of Λ , leading to larger uncertainties in the extrapolation. The feeddown corrections are of the order of 10%, so that these uncertainties can be tolerated.

Combining the efficiency studies for Λ originating from Ξ decays with the mid-rapidity yield ratios and the uncertainties due to the rapidity dependence of this ratio, a feeddown contribution to the total Λ yield of 0.1 ± 0.03 is obtained.

There are also feeddown contributions from the triple strange Ω^- , with quark content *sss*. Its yield is about an order of magnitude smaller than the Ξ yield, so its contributions can be neglected in the present analysis.

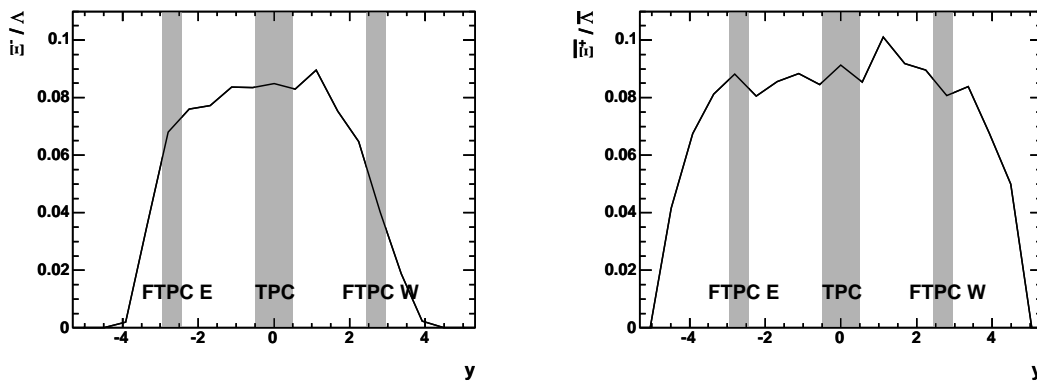


Figure 5.14: Ξ^-/Λ and $\Xi^+/\bar{\Lambda}$ ratios as a function of rapidity, taken from the HIJING event generator. The acceptance of the STAR TPCs is highlighted. This ratio is used to estimate the feeddown contributions at forward rapidity.

5.7 Mean Life

A quantity that demonstrates the signal quality is the reconstructed mean life of the analyzed particle which is derived from the distribution of life times. It can be used to prove that indeed the desired particle is measured, and not random background that produces the same invariant mass distribution due to the applied cuts. The life time has to be calculated in the rest frame of the particle. It is obtained from

$$\tau = \frac{\text{decaylength}}{c\beta\gamma}, \quad (5.2)$$

where the decaylength is the flight distance from the event vertex to the reconstructed decay vertex and β and γ are computed from the reconstructed momentum and the rest mass. Since the distribution of life times is exponential for a particle decay the mean life of the measured particle is obtained by fitting an exponential to the distribution.

The reconstruction efficiency depends strongly on the particle momentum and the decaylength. This has to be corrected for. The efficiency as a function of life time is obtained by dividing the life time distribution of the reconstructed Λ from the embedding with a realistic temperature parameter by the known distribution of life times in the simulation. The corrected life time distribution is obtained by dividing the distribution of Λ candidates by this efficiency.

Figure 5.15 shows the corrected life time of Λ candidates in FTPC West. This distribution contains all background remaining after the geometric cuts. The largest contribution of this background is from K_S^0 decays. Since the K_S^0 has a significantly shorter life time than the Λ a deviation from an exponential is expected at low life

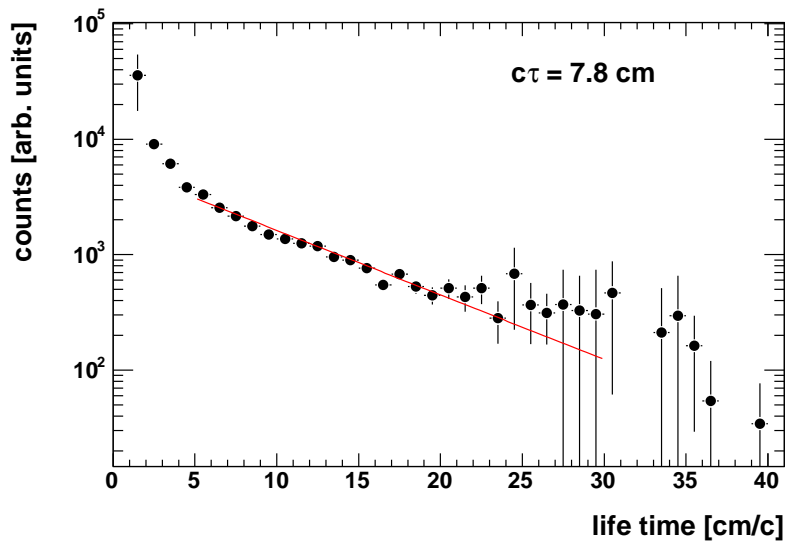


Figure 5.15: Life time of Λ candidates in FTPC W. The distribution is corrected for analysis acceptance and fitted with an exponential function. This yields a $c\tau$ of 7.8 cm, which is in very good agreement with the literature value of 7.9 cm. The excess of entries at low life times corresponds to only a small number of Λ candidates since the efficiency in that region is very low. K_S^0 are expected to contribute to this region.

times. In addition, the necessary corrections are very large below 5 cm/c and above 27 cm/c. Thus, the exponential fit is applied to extract the mean life parameter in a restricted region between 5 cm/c and 27 cm/c. With this fit, a $c\tau$ of 7.8 cm is extracted, which is in very good agreement with the literature value of 7.9 cm. This demonstrates that indeed Λ are reconstructed with the presented analysis.

5.8 K_S^0 Analysis

The main focus of this thesis is on the analysis of Λ and $\bar{\Lambda}$. However, as discussed, K_S^0 decays are very similar in topology to Λ decays, so the same analysis code can be applied to the reconstruction of K_S^0 . The obtained particle yields are compared to the HIJING predictions. The agreement demonstrates that the simulations can be used to estimate the K_S^0 background present in the Λ and $\bar{\Lambda}$ signals.

5.8.1 Kaon Properties and Decay

The neutral Kaon K^0 (mass 497.7 MeV/c², quark content $d\bar{s}$) and its anti-particle \bar{K}^0 (quark content $\bar{d}s$) can both decay into two and three Pions via the weak interaction. This leads to a mixing of both states. While the K^0 and its anti-particle

are both flavor eigenstates with defined strangeness, they are not eigenstates of the weak interaction. It is observed that two types of neutral Kaons exist that have very different life times. Both are linear superpositions of the K^0 and the \bar{K}^0 .

The short-lived kind, referred to as K_S^0 , has a $c\tau$ of 2.68 cm and decays almost exclusively into two Pions. The long-lived species K_L^0 has a $c\tau$ of 15.51 m and has three pion and semi-leptonic decay modes. As STAR uses the charged particle decay signatures to detect neutral particles, the K_L^0 is not accessible.

The K_S^0 is detectable via its decay $K_S^0 \rightarrow \pi^+\pi^-$ which has a branching ratio of 69%. Like the Λ decay, the K_S^0 has the typical V0 signature of a neutral particle decaying into two oppositely charged particles. Since it decays into two π , the decay is symmetric and thus has different kinematics than the Λ decay.

5.8.2 Analysis and Cuts

The analysis method is the same as that for Λ and $\bar{\Lambda}$ which is extensively described in section 5.2. Selection cuts are applied to the same variables. Most cuts can remain unchanged, however, the dca cuts on the decay daughters have to be adapted to the fact that the K_S^0 decay is symmetric. Also, since the mass difference between the Kaon and the final state particles is bigger than in the case of the Λ , more energy is available for the decay daughters, leading to larger opening angles. Thus, no cut on the maximum of the opening angle is applied.

The available energy and the symmetry of the final state leads to a momentum kick for both decay daughters, so that in most cases they do not continue in the original flight direction of the K_S^0 . Both daughters do not point back to the event vertex, therefore background is suppressed by requiring a dca > 2 cm for both decay daughters.

The cuts used to extract a K_S^0 signal from the data are summarized in table 5.3.

| cut parameter | cut value |
|---------------------------------------|-------------|
| number of hits on track | > 7 |
| pion dca to primary vertex | > 2.0 cm |
| dca of daughters at decay vertex | < 0.25 cm |
| dca of V0 candidate to primary vertex | < 1.0 cm |
| opening angle | > 0.02 |
| decay length | > 5.0 cm |

Table 5.3: Cut Parameters for K_S^0 analysis in the forward TPCs.

Since almost half of the K_S^0 mass is available as kinetic energy for the daughter particles, good momentum resolution and reconstruction precision is much more

crucial here than for the reconstruction of Λ . Due to more electronics problems in the East FTPC, the resolution is poorer than in West. This leads to a very wide distribution of the K_S^0 candidate dca distribution. To a certain extent, such effects can be corrected for by the efficiency, as discussed in section 5.6.1. However, the deviations in FTPC East are too large to provide a reliable extrapolation. Thus, no dependable efficiency correction could be performed on that side, so that the K_S^0 analysis is restricted to the deuteron side of the collision, covered by the West FTPC.

5.8.3 Acceptance

Since the K_S^0 is lower in mass than the Λ , it has a higher rapidity at the same pseudorapidity. This leads to a different acceptance of the detector and the analysis.

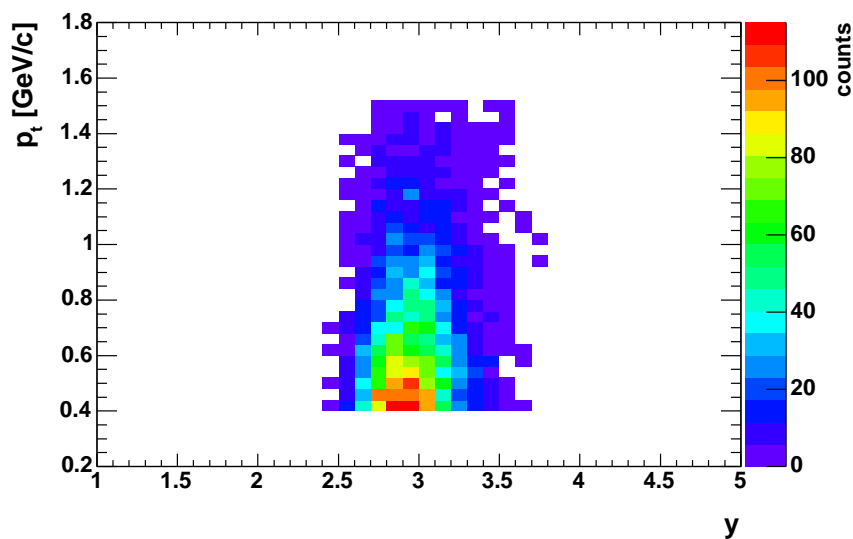


Figure 5.16: Acceptance for K_S^0 candidates in the west FTPC as a function of rapidity and transverse momentum.

Figure 5.16 shows the acceptance for K_S^0 candidates in the west FTPC as a function of rapidity and transverse momentum. To keep the impact of the limited momentum resolution reasonably small, only candidates up to a p_t of 1.5 GeV/c are accepted. Since background from interactions of beam particles with material leads mostly to low p_t tracks, a minimum p_t of 0.4 GeV/c is required. The rapidity window for the analysis is chosen to be $2.75 < y < 3.25$. This range is covered over the full p_t range of the analysis.

5.8.4 Invariant Mass

The invariant mass distributions for the K_S^0 in both detectors together with the expected distribution from simulations is shown in figure 5.17. As in the Λ case, the simulated distribution has been derived from associated K_S^0 without the application of the analysis cuts.

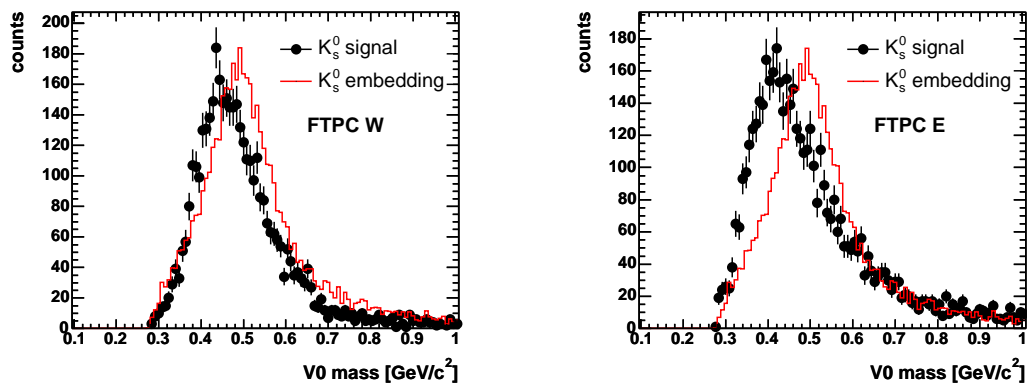


Figure 5.17: Invariant mass distribution of K_S^0 in both detectors compared to the expectation from embedding. A shift of the mass to lower values is apparent. This shift is much more pronounced in FTPC East.

There is a clear shift toward lower mass values. This shift is especially pronounced in FTPC East, and attributed to electronics and calibration problems. A shift in invariant mass was also observed for Λ (see section 5.5) in FTPC East. For Kaons, this shift is more pronounced due to the larger influence of the momentum resolution on the invariant mass caused by the decay properties. The big shift in FTPC East also demonstrates the problems with K_S^0 reconstruction on that side of the collision.

By fitting a gaussian to the invariant mass distribution in the range of 0.2 GeV/c^2 to 0.8 GeV/c^2 , a mass estimate of $475 \pm 2 \text{ MeV}/c^2$ is obtained for K_S^0 in FTPC West, which is about $23 \text{ MeV}/c^2$ below the literature value. The same fit to the simulated distribution yields a mass estimate of $499 \pm 2 \text{ MeV}/c^2$, in agreement with the literature value. The distribution in FTPC East does not follow a gaussian, so a fit to extract a mass estimate is not useful.

The raw particle yield is obtained by summing up all bins from 0.3 GeV/c^2 to 0.7 GeV/c^2 . That way, the determination of the yield is independent of assumptions on the shape of the invariant mass distribution. Due to the extremely tight cuts, the signal is assumed to be basically background free. This assumption is supported by simulation studies. The high dca cut imposed on both decay daughters results in negligible background contributions from Λ and $\bar{\Lambda}$ decays.

5.8.5 Mean Life

As for the Λ , also here the measured life time is a good indicator of data quality. The same method that is described in section 5.7 is applied, using embedded K_S^0 and the K_S^0 mean life.

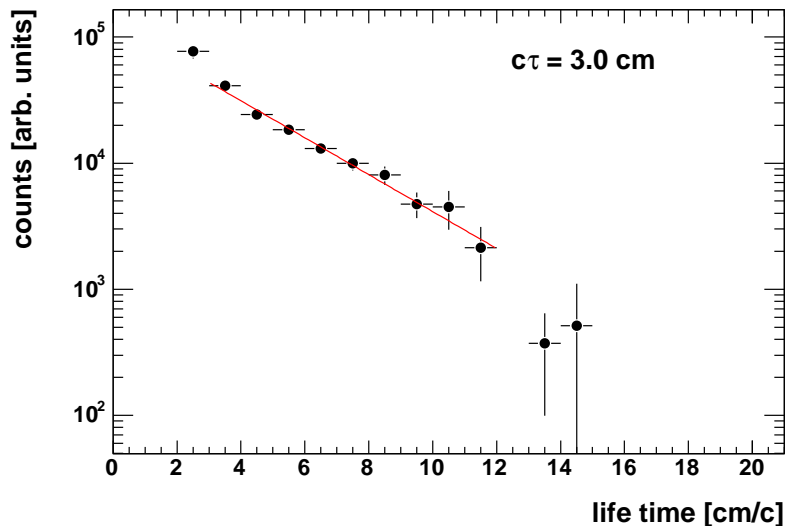


Figure 5.18: Life time of K_S^0 candidates in FTPC West. The distribution is corrected for analysis acceptance. The exponential fit yields a $c\tau$ of 3.0 cm, in good agreement with the literature value of 2.7 cm

Figure 5.18 shows the life time distribution for K_S^0 candidates. As the background distributions from other particles are negligible, no significant deviation due to other decays with different life times are expected. The exponential fit to the data yields a $c\tau$ of 3.0 cm, which is in good agreement with the literature value of 2.7 cm. This demonstrates that K_S^0 are reconstructed with the analysis. Thus, the results can be used to verify the yield estimate for the background subtraction.

5.8.6 K_S^0 yield

To obtain a corrected K_S^0 yield, efficiency corrections and the extrapolation of unmeasured parts of the spectrum have to be performed.

Efficiency Correction

For the efficiency correction, the same method is used as for Λ and $\bar{\Lambda}$. K_S^0 with a realistic transverse momentum distribution are embedded into d+Au minimum bias events and then passed to the analysis software. A temperature parameter of 200

MeV is used, determined by an exponential fit to the transverse mass spectrum of K_S^0 candidates.

For $0.4 \text{ GeV}/c < p_t < 1.5 \text{ GeV}/c$, an average efficiency of 0.01616 ± 0.0005 (stat) is obtained. This efficiency has to be corrected for differences in the dca distributions between data and simulation. For the Λ analysis, this factor was determined to be 0.7 ± 0.05 . To obtain the total yield, an additional factor of 0.69 has to be used to correct for the branching ratio of the decay $K_S^0 \rightarrow \pi^+\pi^-$.

Yield Extrapolation

Due to the limited coverage of the analysis in transverse momentum, the total yield dN/dy can only be obtained by extrapolation. To do this, a specific functional form of the transverse momentum distribution has to be assumed. As for the case of the Λ , a m_t exponential function is used.

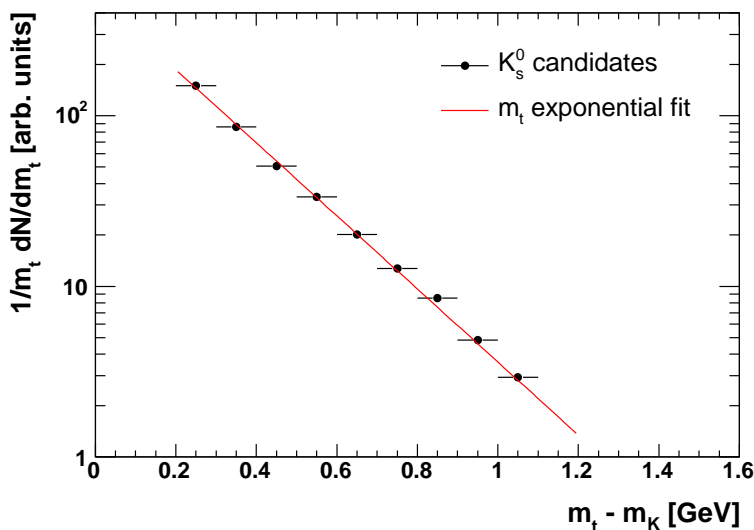


Figure 5.19: Transverse mass distribution of K_S^0 candidates. An exponential function in m_t is fitted to the data. This yields a temperature parameter of $0.203 \text{ GeV} \pm 0.02$ (fit).

Figure 5.19 shows the transverse mass distribution of the K_S^0 candidates in FTPC West. By applying a m_t exponential fit to the data, a temperature parameter of $0.203 \text{ GeV} \pm 0.02$ (fit) is obtained. This leads to a choice of 200 MeV for the embedding simulation.

With these parameters, the fraction of the yield that is covered by the analysis can be determined. With a m_t exponential distribution and a p_t coverage from 0.4 GeV/c to 1.5 GeV/c 49% of the total K_S^0 yield is measured. As a consequence, half

of the yield is extrapolated, compared to only 35% for the Λ . This large contribution from the extrapolation leads to significant systematic uncertainties.

Applying the efficiency corrections discussed above and using the extrapolation based on the m_t exponential distribution, dN/dy is calculated from the raw yield obtained by bin counting. At $y = 3.0$ the K_S^0 yield is $dN/dy = 0.18 \pm 0.01$ (stat). A detailed study of the systematic error was not performed, but it is expected that it is larger than the one determined for the Λ analysis in FTPC West (see section 6.1.3). The estimated systematic uncertainty on dN/dy is therefore of the order of 20%.

The goal of the K_S^0 analysis is the verification of the assumption that HIJING provides a reasonable description of the K_S^0 abundance in d+Au events, and thus can be used as input for the background correction of the Λ and $\bar{\Lambda}$ data.

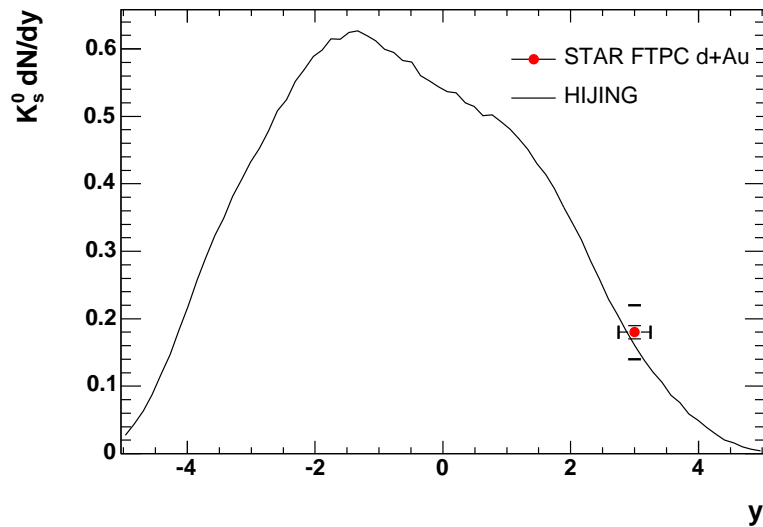


Figure 5.20: dN/dy of K_S^0 in d+Au minimum bias events. Also shown is the HIJING prediction as a function of rapidity. The horizontal error bar is given by the rapidity range of the analysis, the vertical error bars are the statistical error and the estimated systematic error.

Figure 5.20 shows the measured K_S^0 yield together with the results from HIJING calculations. There is a very good agreement of the data with the model expectation. This suggests that the use of HIJING simulations for the estimate of the K_S^0 background contribution to the Λ and $\bar{\Lambda}$ signals is warranted.

Chapter 6

Results on Λ Hyperons

The results presented in this chapter were obtained by analysing the d+Au dataset recorded with the STAR detector in 2003. Using the method described in chapter 5 the rapidity density of Λ , $\bar{\Lambda}$ and $\Lambda - \bar{\Lambda}$ as well as the temperature parameters for both particles and the $\bar{\Lambda}/\Lambda$ ratio is determined for rapidities $y = 2.75$ and $y = -2.75$. As already mentioned in section 5.6.2, Σ^0 particles cannot be distinguished from Λ particles, and no reliable correction exists for these contributions. Here, Λ and $\bar{\Lambda}$ always denote $\Lambda + \Sigma^0$ and $\bar{\Lambda} + \bar{\Sigma}^0$, respectively.

Using the centrality classes defined in section 3.4.3 the centrality dependence of these observables is studied.

If not stated otherwise, all results that are presented are obtained from d+Au minimum bias collisions.

6.1 Particle Yields

The acceptance in transverse momentum is limited at low p_t by increasing background and at high p_t by deteriorating momentum and charge sign resolution. Thus, the total particle yield can not be measured, and the yields in the unmeasured regions have to be extrapolated. This is done by assuming a suitable functional form for the p_t dependence of the particle density.

Based on [39], an m_t - exponential function, already introduced in section 5.6.1 is assumed. To obtain the parameters for the function, the particle yield has to be determined as a function of transverse momentum. Due to the limited statistics and the momentum resolution of the detectors, only four bins in transverse momentum are used: 0.5 GeV/c to 0.7 GeV/c, 0.7 GeV/c to 1.0 GeV/c, 1.0 GeV/c to 1.3 GeV/c and 1.3 GeV/c to 2.0 GeV/c.

For each of these bins, a background subtraction and efficiency correction is performed.

| p_t [GeV/c] | efficiency | |
|---------------|-----------------------|-----------------------|
| | West | East |
| 0.5 – 0.7 | 0.06221 ± 0.00082 | 0.03580 ± 0.00085 |
| 0.7 – 1.0 | 0.07056 ± 0.00081 | 0.04640 ± 0.00090 |
| 1.0 – 1.3 | 0.06548 ± 0.00103 | 0.04354 ± 0.00115 |
| 1.3 – 2.0 | 0.06439 ± 0.00123 | 0.04439 ± 0.00141 |

Table 6.1: Efficiency for Λ and $\bar{\Lambda}$ reconstruction as a function of p_t with the standard cuts summarized in table 5.1. These numbers do not include the branching ratio of the $\Lambda \rightarrow p\pi^-$ decay channel and the additional correction factor of 0.7 for the differences in the dca distributions for real and simulated particles. The errors are statistical errors from the embedding study.

Table 6.1 summarizes the efficiency for the reconstruction of Λ and $\bar{\Lambda}$ as a function of p_t in the rapidity range $2.5 < |y| < 3.0$. The significantly lower efficiency in East is due to the stricter cuts used for FTPC East and to the larger number of faulty electronic channels. For the extraction of corrected yields, these efficiency numbers have to be multiplied by 0.639 for the branching ratio of the $\Lambda \rightarrow p\pi^-$ decay channel and by 0.7 to correct for the too narrow dca distribution in embedding. Simulations have shown that the efficiencies are equal to within 2% for particle and anti-particle, so the above numbers can be used for Λ and $\bar{\Lambda}$ alike.

6.1.1 Yield and Temperature Determination

The particle yield and the temperature parameter of the p_t distribution is determined assuming an exponential function in transverse mass for the particle density,

$$\frac{1}{m_t} \frac{d^2 N}{dy dm_t} = C e^{-m_t/T}, \quad (6.1)$$

where N is the mean number of particles per event, T is the temperature parameter and C is a scaling constant.

Integrating equation 6.1 gives the rapidity density

$$dN/dy = \int_{m_\Lambda}^{\infty} m_t C e^{-m_t/T} dm_t = T (m_\Lambda + T) C. \quad (6.2)$$

The parameters T and C are determined by fitting the particle spectra with the function on the right side of equation 6.1. Using the definition $m_t = \sqrt{p_t^2 + m_\Lambda^2}$ it can be shown that

$$\frac{1}{m_t} \frac{d^2 N}{dy dm_t} = \frac{1}{p_t} \frac{d^2 N}{dy dp_t} \quad (6.3)$$

so that the data can also be plotted as a function of transverse momentum and then fitted with the m_t exponential function. This approach is used here. Since the data cover the p_t range from 0.5 GeV/c to 2.0 GeV/c, the measured yield is approximately 64% of the total yield.

6.1.2 Minimum Bias Spectra

Figure 6.1 shows the transverse momentum spectra $1/p_t dN^2/dydp_t$ for Λ and $\bar{\Lambda}$ in both FTPC West and East.

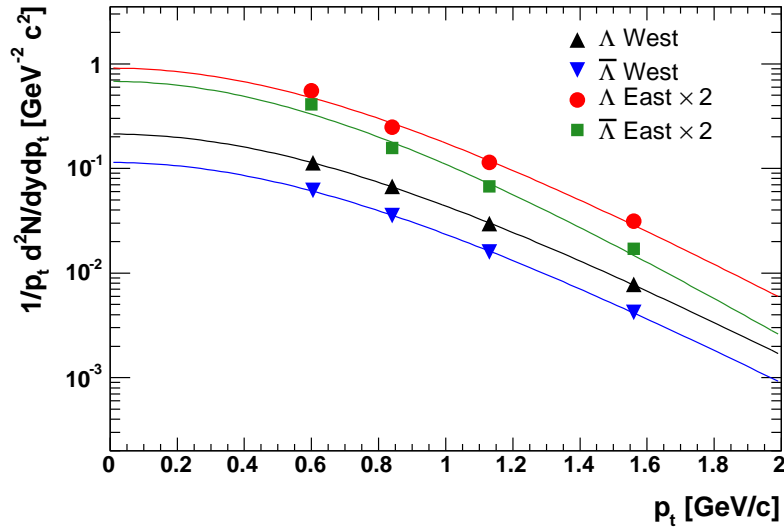


Figure 6.1: Λ and $\bar{\Lambda}$ spectra for d+Au minimum bias events. The data in FTPC E is multiplied by two for better visibility. The curves show an m_t exponential fit (equation 6.1) to the data points. While the spectra on the West side show a good exponential behavior, the lowest point on East deviates from an m_t exponential function.

The numbers are corrected for feeddown from weak decays of higher mass hyperons and for efficiency and detector acceptance. An m_t exponential fit to the data points is also shown. On the West side, the fit describes the data very well, while on the East side, a discrepancy with the point at lowest p_t is apparent.

The reason for this discrepancy could not be fully understood, but there are several possible explanations. The efficiency in FTPC East drops more at low p_t than in FTPC West, due to loss of electronics. Problems with the efficiency determination might lead to an underestimate of the efficiency, and thus to an overestimate of the particle yield at low p_t . Combinatorial background decreases with transverse momentum, so the remaining background will be concentrated in the lowest bin. Simulations show this effect to be quite small with the strict cuts that are applied,

but from noisy areas in the detector there might be additional contributions. Due to the higher particle density on the East side, a higher background level is expected. The shift of the invariant mass distribution towards lower mass already mentioned in section 5.5 is most pronounced in the low p_t bin in FTFC East. All this leads to a sizable uncertainty for that lowest point.

The deviation from a m_t exponential behavior could also indicate that this distribution is not suitable to describe the data in FTFC East at low p_t .

Effects of this deviation of the first point are investigated by excluding this point from the fit as discussed below.

6.1.3 Systematic Errors

For later interpretation of the results, the estimate of systematic errors of the analysis is crucial. For the systematic error of the extrapolated yield, there are several contributions that have been investigated, namely from the cut selection, the cut on the number of hits, the background normalization and the feeddown correction. In addition, a general uncertainty of 10% for the efficiency determination from embedding (including the correction factors) is assumed.

The systematic error from the cut selection, dominated by the cut on the pion dca, was determined by a variation of the cuts within a reasonable range. The cuts on the pion and proton dca were varied within 0.5 cm of the nominal values, the daughter dca cut was varied within ± 0.15 cm. These variations were also applied to the efficiency correction and to the K_S^0 background. From the changes in the corrected yield the errors were obtained. The size of the error depends on the detector and on the particle. The contributions are shown in table 6.2.

| Detector | Particle | positive Error | negative Error |
|----------|-----------------|----------------|----------------|
| West | Λ | 0.06 | 0.04 |
| | $\bar{\Lambda}$ | 0.12 | 0.07 |
| East | Λ | 0.17 | 0.13 |
| | $\bar{\Lambda}$ | 0.20 | 0.16 |

Table 6.2: Systematic error of the particle yield from the analysis cuts. The numbers were obtained by a variation of the cut parameters.

By a comparison of the number of hits on simulated and real candidate tracks, an error of 5% from the requirement of at least 8 FTFC hits has been estimated. The kaon background never exceeds 20% of the signal, so assuming a 20% error from efficiency and normalization leads to a 4% contribution. The feeddown correction is 10 % of the yield and based on the discussion of uncertainties in section 5.6.2 this gives a contribution of 3% to the total systematic error. Excluding the first

point from the fit leads to a 8% reduction of the Λ yield and to a 12% reduction of the $\bar{\Lambda}$ yield in FTPC East. Assuming that the individual error contributions are independent, an estimate of the total systematic error on the particle yield is obtained and summarized in table 6.3.

| Detector | Particle | positive Error | negative Error |
|----------|-----------------|----------------|----------------|
| West | Λ | 0.14 | 0.13 |
| | $\bar{\Lambda}$ | 0.17 | 0.14 |
| East | Λ | 0.21 | 0.20 |
| | $\bar{\Lambda}$ | 0.23 | 0.23 |

Table 6.3: Total systematic error on the particle yields.

The significantly larger errors for FTPC East reflect higher uncertainties due to more electronics problems during data taking and due to the higher particle density and thus higher background contributions. By treating the upper and the lower half of the detectors separately, the influence of the different problematic detector regions can be investigated. For FTPC West, differences of the order of 1% were observed, while for FTPC East, the yield differences between top and bottom half of the detector are around 10%. This illustrates that the systematics in FTPC W are better under control, reflected in smaller errors.

In addition to the individual particle yields, the net Λ yield, i.e. the difference of Λ and $\bar{\Lambda}$ yield, is an interesting quantity, as it is related to baryon transport and associated production of Λ particles. The systematic error is determined using the same method as for the particle yields.

Since the background is equal for particle and anti-particle, uncertainties from background normalization cancel. This reduces the systematic errors especially on the Au side since the backgrounds in the Λ and $\bar{\Lambda}$ signals are affected in the same way by cut changes. The systematic error on the yield of net Λ was determined to be 13% for both FTPC East and West.

6.1.4 Minimum bias yields

From the m_t exponential fit to the particle spectra, the yield is determined by integration. The statistical error is given by the fit error, since the statistical errors of the individual points are used in the fit. The systematic error of the yield is calculated using the results described in section 6.1.3.

Table 6.4 summarizes the minimum bias particle yields with both statistical and systematic errors. For model comparisons and a discussion of these results refer to chapter 7.

| Detector | Particle | dN/dy |
|----------|-----------------|--|
| West | Λ | 0.070 ± 0.002 (stat) $^{+0.010}_{-0.009}$ (syst) |
| | $\bar{\Lambda}$ | 0.037 ± 0.002 (stat) $^{+0.006}_{-0.005}$ (syst) |
| | Net Λ | 0.033 ± 0.003 (stat) ± 0.004 (syst) |
| East | Λ | 0.142 ± 0.006 (stat) $^{+0.030}_{-0.028}$ (syst) |
| | $\bar{\Lambda}$ | 0.094 ± 0.005 (stat) ± 0.022 (syst) |
| | Net Λ | 0.048 ± 0.008 (stat) ± 0.006 (syst) |

Table 6.4: Minimum bias particle yields from both FTPCs at rapidity $y = -2.75$ (East) and $y = 2.75$ (West).

6.2 Temperature Parameter

From the m_t exponential fit to the particle spectra (figure 6.1) the inverse slope parameter, usually called temperature parameter (parameter T in equation 6.1), can be extracted. It is a measure for the slope of the transverse momentum distribution of the particles, and thus of interest for the study of the particle production dynamics.

The systematic error of the temperature parameter is determined by assuming a 10% point-to-point systematic error on the individual p_t points, and then extracting the error from the fit. For FTPC East, the deviation of the lowest p_t point from the m_t exponential behaviour has to be taken into account. This has a significant influence on the temperature determination. When excluding the first point from the fit the temperature parameter is higher by around 20 MeV.

| Detector | Particle | Temperature Parameter [GeV] |
|----------|-----------------|--|
| West | Λ | 0.241 ± 0.004 (stat) ± 0.011 (syst) |
| | $\bar{\Lambda}$ | 0.242 ± 0.005 (stat) ± 0.015 (syst) |
| East | Λ | 0.232 ± 0.005 (stat) $\pm 0.014^{+0.018}$ (syst) |
| | $\bar{\Lambda}$ | 0.210 ± 0.004 (stat) $\pm 0.014^{+0.023}$ (syst) |

Table 6.5: Temperature parameter of the minimum bias p_t spectra of Λ and $\bar{\Lambda}$ in both FTPCs. The change in temperature when the first point is ignored in the fit is added as additional systematic error for FTPC East.

Table 6.5 summarizes the inverse slope parameters for the minimum bias p_t spectra with statistical and systematic errors. The deviating first bin in FTPC East introduces a large error, and makes the East temperature parameters problematic to use for interpretation. The results show good agreement with the initial estimate of 0.23 GeV used for the embedding of particles for the efficiency determination and confirm this choice. This validates the efficiency correction.

6.3 $\bar{\Lambda}/\Lambda$ Ratio

The anti-baryon to baryon ratio is sensitive to the amount of stopping in the collision. It is governed by the relative rates of the two production channels for the Λ . The associated production $N + N \rightarrow N + \Lambda + K$ moves the baryon number of the beam nuclei to lower rapidity, while the pair production $N + N \rightarrow N + N + \Lambda + \bar{\Lambda}$ does not contribute to the net baryon number, since it produces Λ and $\bar{\Lambda}$ in equal number.

The influence of these two production mechanisms on the $\bar{\Lambda}/\Lambda$ ratio is illustrated by the following equation,

$$\bar{\Lambda}/\Lambda \equiv \frac{N_{\bar{\Lambda}}}{N_{\Lambda}} = \frac{N_{pair}}{N_{pair} + N_{ass}}, \quad (6.4)$$

where N_{pair} and N_{ass} are the average number of Λ particles per event originating from pair production and associated production, respectively. By subsequent rescattering processes, the hyperons produced via associated production can also be moved towards lower rapidity.

Since the efficiency for $\bar{\Lambda}$ is equal to that for Λ systematic uncertainties from the efficiency determination cancel in the ratio. The ratio can either be determined by dividing the corrected yields, obtained in section 6.1.4 or by dividing the number of reconstructed particles, extracted from the invariant mass plots shown in figure 5.12. Differences between the two, due to the fit and the extrapolation that is done with the fit results, are of the order of 5% and are used as a contribution to the systematic error.

To be consistent with the quoted yields, the ratio obtained from the total particle yields is quoted here. The results for both detectors together with the systematic error obtained by a variation of the cuts are summarized in table 6.6.

| Detector | $\bar{\Lambda}/\Lambda$ |
|----------|--|
| West | 0.54 ± 0.03 (stat) ± 0.04 (syst) |
| East | 0.66 ± 0.04 (stat) ± 0.05 (syst) |

Table 6.6: $\bar{\Lambda}/\Lambda$ for d+Au minimum bias events for both detectors.

To exclude that the particle ratio is strongly influenced by local effects in the detector, such as defective electronics or noisy areas, it was calculated for the top and bottom half of both detectors separately. The difference is around 2% for both East and West, and thus well within the errors, indicating no influence from localized detector problems on the physics result.

6.4 Centrality Dependence

In this section, the centrality dependence of the yield, the temperature parameter and the $\bar{\Lambda}/\Lambda$ ratio is investigated by using the three centrality classes introduced in section 3.4.3. With changing impact parameter of the collision, the number of participating nucleons and the number of collisions each nucleon suffers changes. Differences between the deuteron and the gold side are expected since the number of participants from the gold nucleus increases strongly with increasing centrality, while for the nucleons from the deuteron, the number of collisions each nucleon suffers goes up. For each of the three used centrality classes, the corrected spectra for Λ and $\bar{\Lambda}$ on both sides of the collisions are extracted. Here, the corrections obtained for minimum bias events are applied to all centrality classes. This yields dN/dy for Λ , $\bar{\Lambda}$ and net Λ as well as the temperature parameters for both particles and the $\bar{\Lambda}/\Lambda$ ratio.

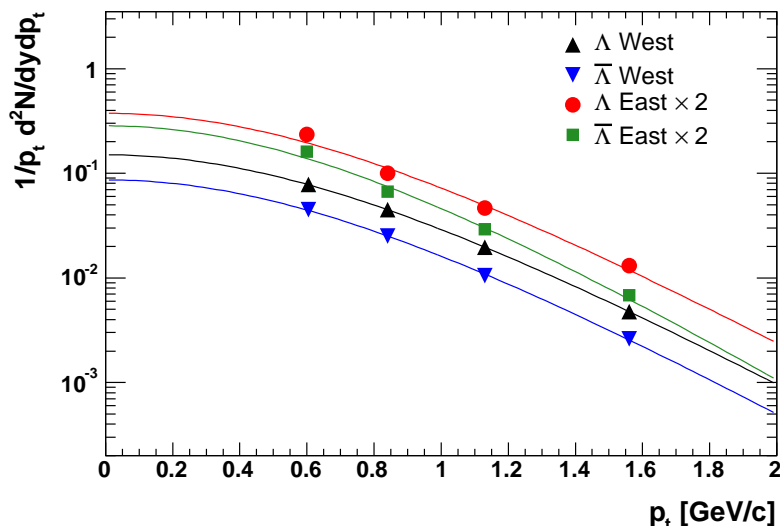


Figure 6.2: Λ and $\bar{\Lambda}$ spectra for the peripheral d+Au collisions (40% – 100% most central). The data in FTPC East is multiplied by two for better visibility. The curves show an m_t exponential fit (equation 6.1) to the data points.

Figures 6.2, 6.3 and 6.4 show the spectra for peripheral, mid-central and central d+Au collisions, respectively. In all centrality classes, the deviation of the lowest p_t point in FTPC East from the m_t exponential behavior is observed. This effect has already been discussed with the minimum bias spectra. From m_t exponential fits to the spectra, the extrapolated yields and the temperature parameters of Λ and $\bar{\Lambda}$ are obtained. With these results, the net Λ dN/dy and the $\bar{\Lambda}/\Lambda$ ratio is calculated. These results are summarized for all three centrality classes in tables 6.7, 6.8 and 6.9.

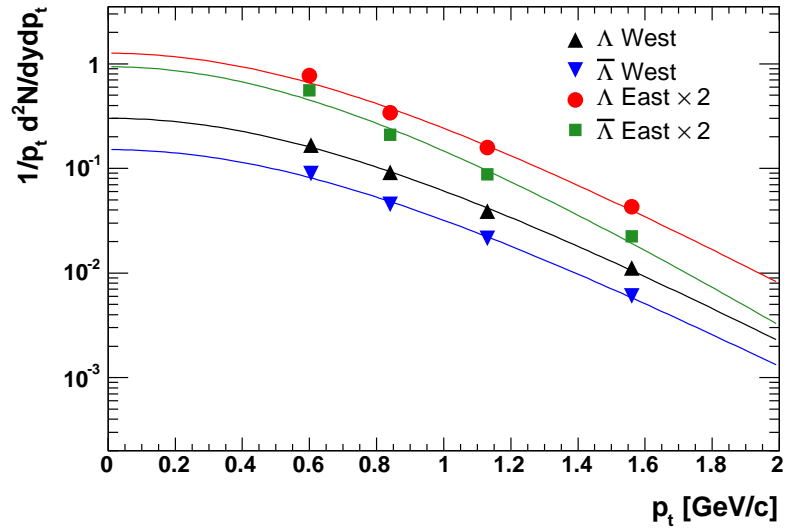


Figure 6.3: Λ and $\bar{\Lambda}$ spectra for mid-central d+Au collisions (20% – 40% most central). The data in FTPC East is multiplied by two for better visibility. The curves show an m_t exponential fit (equation 6.1) to the data points.

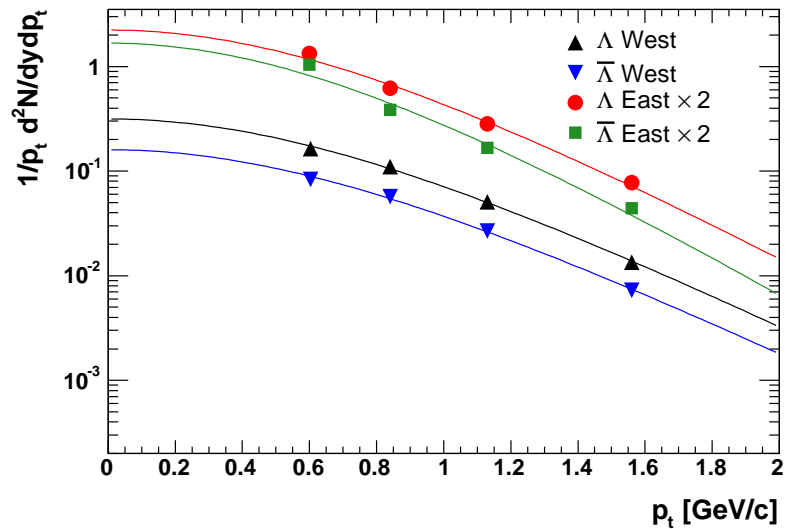


Figure 6.4: Λ and $\bar{\Lambda}$ spectra for central d+Au collisions (20% most central). The data in FTPC East is multiplied by two for better visibility. The curves show an m_t exponential fit (equation 6.1) to the data points.

| Peripheral (40% — 100%) | | | |
|-------------------------------|----------|-----------------|--|
| | Detector | Particle | dN/dy |
| Yield | West | Λ | 0.047 ± 0.002 (stat) $^{+0.007}_{-0.006}$ (syst) |
| | | $\bar{\Lambda}$ | 0.026 ± 0.002 (stat) ± 0.004 (syst) |
| | | Net Λ | 0.021 ± 0.003 (stat) ± 0.003 (syst) |
| | East | Λ | 0.059 ± 0.004 (stat) ± 0.012 (syst) |
| | | $\bar{\Lambda}$ | 0.040 ± 0.003 (stat) ± 0.009 (syst) |
| | | Net Λ | 0.019 ± 0.005 (stat) ± 0.003 (syst) |
| | Detector | Particle | Temperature Parameter [GeV] |
| Temperature | West | Λ | 0.232 ± 0.005 (stat) ± 0.010 (syst) |
| | | $\bar{\Lambda}$ | 0.228 ± 0.007 (stat) ± 0.013 (syst) |
| | East | Λ | 0.232 ± 0.007 (stat) $\pm 0.014^{+0.022}$ (syst) |
| | | $\bar{\Lambda}$ | 0.210 ± 0.007 (stat) $\pm 0.014^{+0.018}$ (syst) |
| | Detector | | $\bar{\Lambda}/\Lambda$ ratio |
| $\bar{\Lambda}/\Lambda$ ratio | West | | 0.56 ± 0.05 (stat) ± 0.05 (syst) |
| | East | | 0.67 ± 0.10 (stat) ± 0.05 (syst) |

Table 6.7: Results summary for peripheral d+Au events (40% – 100% most central) at $y = -2.75$ (East) and $y = 2.75$ (West).

| Mid-central (20% — 40%) | | | |
|-------------------------------|----------|-----------------|--|
| | Detector | Particle | dN/dy |
| Yield | West | Λ | 0.098 ± 0.005 (stat) $^{+0.014}_{-0.013}$ (syst) |
| | | $\bar{\Lambda}$ | 0.051 ± 0.004 (stat) $^{+0.009}_{-0.007}$ (syst) |
| | | Net Λ | 0.047 ± 0.006 (stat) ± 0.006 (syst) |
| | East | Λ | 0.197 ± 0.012 (stat) $^{+0.041}_{-0.039}$ (syst) |
| | | $\bar{\Lambda}$ | 0.128 ± 0.010 (stat) ± 0.029 (syst) |
| | | Net Λ | 0.069 ± 0.016 (stat) ± 0.009 (syst) |
| | Detector | Particle | Temperature Parameter [GeV] |
| Temperature | West | Λ | 0.239 ± 0.006 (stat) ± 0.015 (syst) |
| | | $\bar{\Lambda}$ | 0.246 ± 0.009 (stat) ± 0.022 (syst) |
| | East | Λ | 0.232 ± 0.006 (stat) $\pm 0.013^{+0.019}$ (syst) |
| | | $\bar{\Lambda}$ | 0.206 ± 0.007 (stat) $\pm 0.014^{+0.025}$ (syst) |
| | Detector | | $\bar{\Lambda}/\Lambda$ ratio |
| $\bar{\Lambda}/\Lambda$ ratio | West | | 0.52 ± 0.05 (stat) ± 0.05 (syst) |
| | East | | 0.65 ± 0.06 (stat) ± 0.05 (syst) |

Table 6.8: Results summary for mid-central d+Au events (20% — 40% most central)

| Central (Top 20%) | | | |
|-------------------------------|----------|-----------------|--|
| | Detector | Particle | dN/dy |
| Yield | West | Λ | 0.111 ± 0.006 (stat) $^{+0.016}_{-0.014}$ (syst) |
| | | $\bar{\Lambda}$ | 0.057 ± 0.004 (stat) $^{+0.010}_{-0.008}$ (syst) |
| | | Net Λ | 0.054 ± 0.007 (stat) ± 0.007 (syst) |
| | East | Λ | 0.351 ± 0.018 (stat) $^{+0.074}_{-0.070}$ (syst) |
| | | $\bar{\Lambda}$ | 0.235 ± 0.015 (stat) ± 0.054 (syst) |
| | | Net Λ | 0.116 ± 0.023 (stat) ± 0.015 (syst) |
| | Detector | Particle | Temperature Parameter [GeV] |
| Temperature | West | Λ | 0.257 ± 0.006 (stat) ± 0.013 (syst) |
| | | $\bar{\Lambda}$ | 0.261 ± 0.009 (stat) ± 0.019 (syst) |
| | East | Λ | 0.233 ± 0.006 (stat) $\pm 0.016^{+0.017}$ (syst) |
| | | $\bar{\Lambda}$ | 0.212 ± 0.006 (stat) $\pm 0.018^{+0.025}$ (syst) |
| | Detector | | $\bar{\Lambda}/\Lambda$ ratio |
| $\bar{\Lambda}/\Lambda$ ratio | West | | 0.51 ± 0.05 (stat) ± 0.05 (syst) |
| | East | | 0.67 ± 0.05 (stat) ± 0.05 (syst) |

Table 6.9: Results summary for central d+Au events (20% most central).

6.5 ZDC Neutron Tagged Events

The study of d+Au collisions offer the interesting possibility to select a class of events in which only one of the two nucleons in the deuteron participated in the reaction. With the STAR zero degree calorimeters (see section 3.2.3), a single beam momentum neutron can be detected. This allows the identification of events where only the proton from the deuteron participated in the reaction. Such events give access to the study of peripheral p+Au collisions in the d+Au data sample. The cross section for this process with a spectator neutron is $(19.2 \pm 1.3)\%$ of the d+Au hadronic cross section [10].

Due to the low multiplicity in these events, the statistics of reconstructed Λ and $\bar{\Lambda}$ particles are not sufficient to extract particle spectra. However, by determining the number of reconstructed particles after background subtraction in the momentum range from 0.5 GeV/c to 2.0 GeV/c, dN/dy can be extrapolated by comparing this number to the same number in other centrality classes. Figure 6.5 shows the background subtracted invariant mass distributions for both particle species for these events.

For the extrapolation of the yield, a comparison with the peripheral bin is used, since around two thirds of the peripheral events are events with either a neutron or a proton spectator from the deuteron. Thus, the temperature parameters should be comparable, and the extrapolation to all p_t possible with the same correction

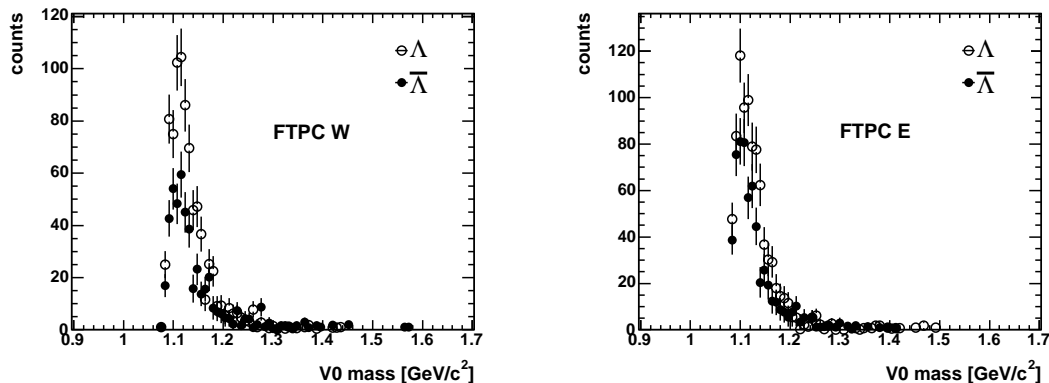


Figure 6.5: Background subtracted invariant mass distributions for Λ and $\bar{\Lambda}$ in both detectors using ZDC neutron tag events. The limitations caused by low count statistics are apparent from the fluctuations in the distributions.

factors. To allow for the additional uncertainties introduced by this extrapolation, an additional 10% systematic error is assumed.

Table 6.10 shows the particle density for ZDC neutron tag events obtained by using the extrapolation based on peripheral events.

| Detector | Particle | dN/dy |
|----------|-----------------|--|
| West | Λ | 0.031 ± 0.002 (stat) ± 0.005 (syst) |
| | $\bar{\Lambda}$ | 0.017 ± 0.002 (stat) ± 0.003 (syst) |
| | Net Λ | 0.014 ± 0.003 (stat) ± 0.002 (syst) |
| East | Λ | 0.052 ± 0.003 (stat) $^{+0.012}_{-0.011}$ (syst) |
| | $\bar{\Lambda}$ | 0.038 ± 0.003 (stat) ± 0.010 (syst) |
| | Net Λ | 0.014 ± 0.004 (stat) ± 0.003 (syst) |

Table 6.10: Particle yields from both FTPCs at rapidity $y = -2.75$ (East) and $y = 2.75$ (West) for ZDC neutron tag events.

With these extrapolated values, the $\bar{\Lambda}/\Lambda$ ratio can be determined to be 0.55 ± 0.05 (stat) ± 0.06 (syst) on the deuteron side and 0.73 ± 0.05 (stat) ± 0.07 (syst) on the gold side.

Chapter 7

Discussion

The discussion of the results on forward Λ and $\bar{\Lambda}$ production proceeds in three steps. As a first step, the influence of the nuclear matter on particle production is investigated via the well-known nuclear modification factor. A possible enhancement of strange particle yields in central d+Au collisions with respect to peripheral reactions and the centrality dependence of the inverse slope parameters is studied. The minimum bias data are confronted with model calculations to identify the processes that contribute to stopping and baryon transport. On the deuteron side, an estimate of the mean rapidity loss of incoming baryons as a function of collision centrality is given.

7.1 The Influence of the Medium

To investigate the influence of the medium in nucleus–nucleus collisions, the nuclear modification factor is used. It is defined as the ratio of the differential yields in A+B and p+p reactions normalized by the number of binary collisions,

$$R_{AB} \equiv \frac{1}{n_{bin}} \frac{d^2 N^{A+B}/dp_t d\eta}{d^2 N^{p+p}/dp_t d\eta}. \quad (7.1)$$

The value of R_{AB} is unity in the case of a scaling with the mean number of binary collisions. This is expected for hard processes and thus will only be valid above a certain transverse momentum. In d+Au collisions an enhancement of R_{dAu} above unity for $p_t > 2$ GeV/c is observed at mid-rapidity [10, 45], as shown in figure 7.1. This enhancement of particle production at intermediate transverse momentum with respect to binary collision scaling is attributed to collective effects of the nucleons in the nucleus. Such an enhancement, referred to as the Cronin effect, was first observed in fixed-target proton–nucleus collisions [46]. In Au+Au collisions at RHIC, an increasing suppression of R_{AA} (the ratio of n_{bin} scaled Au+Au to p+p spectra, included in figure 7.1) with increasing transverse momentum is observed. This

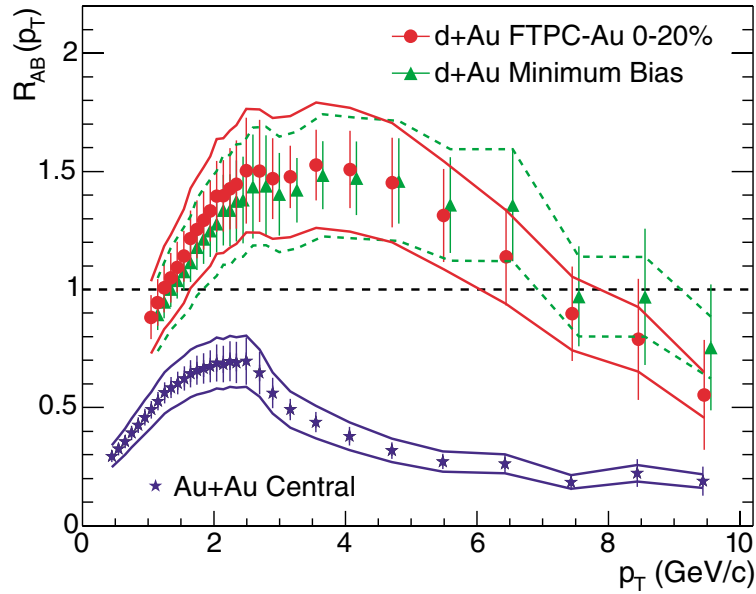


Figure 7.1: Nuclear modification factor for d+Au and Au+Au collisions at mid-rapidity taken from [10]. While a clear enhancement above unity due to the Cronin effect is apparent in d+Au reactions there is a suppression of particles with high transverse momentum in central Au+Au collisions.

behavior is linked to the suppression of jets with high transverse momentum, as discussed in section 2.4.3.

With the FTPCs, the nuclear modification factor can only be studied at low p_t . As there is no p+p data available, a related quantity that uses the ratio of central to peripheral differential yields is introduced,

$$R_{cp} \equiv \frac{n_{bin,p} d^2 N^c / dp_t d\eta}{n_{bin,c} d^2 N^p / dp_t d\eta}. \quad (7.2)$$

In the ratio systematic errors from efficiency determination and common corrections cancel, since the same dataset with the same detector parameters is used.

Measurements by the BRAHMS experiment [45] show that R_{cp} for charged hadrons decreases with increasing rapidity toward the deuteron side. It was also observed that at forward rapidity this suppression is stronger for more central events. On the other hand at mid-rapidity R_{cp} for central events lies above the mid-central values.

Figure 7.2 shows R_{cp} for Λ on both sides of the collision. The ratio was calculated for central (top 20%) and mid-central (20% — 40%) events. Since the centrality dependence of the $\bar{\Lambda}$ yield and temperature parameter matches that of the Λ , the $\bar{\Lambda}$ nuclear modification factor behaves like that of the Λ and is omitted here. As a reference, R_{cp} for non-identified charged hadrons h_{ch} measured with the FTPCs for central d+Au events on both collision sides [21] is included in the figure. Since the

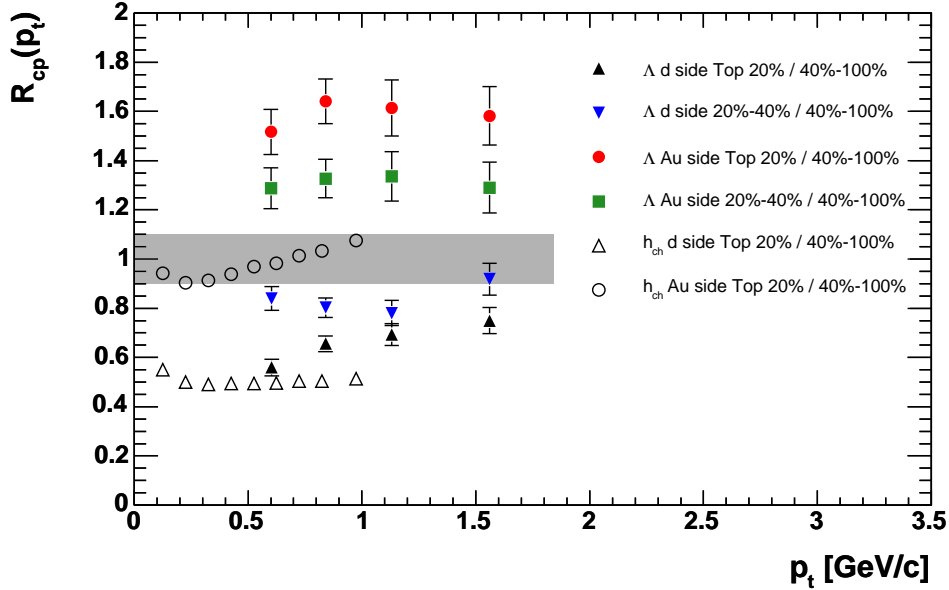


Figure 7.2: R_{cp} for Λ for central and mid-central events on both sides of the collision. As a reference, R_{cp} for charged hadrons at $\eta = 3.1$ and $\eta = -3.1$ [21] is included. An estimate of the systematic error, mostly given by the uncertainty in the number of collisions, is indicated by the gray band.

majority of the produced particles are pions, the h_{ch} distribution approximates the distribution for $\pi^+ + \pi^-$.

Clearly, the Λ data in figure 7.2 show the same trend that was already observed by BRAHMS for charged hadrons. On the deuteron side, R_{cp} is below unity in the whole measured p_t range. The values for more central events are below the mid-central events. On the gold side, where no measurements from BRAHMS are available, the picture is reversed. R_{cp} is above unity, with the more central events showing values above those of the mid-central events.

The comparison of the Λ R_{cp} to the charged hadron R_{cp} shows that on the deuteron side the values at low transverse momentum are compatible. However, in the case of Λ a rise of the nuclear modification factor with increasing transverse momentum is observed, while no p_t dependence is apparent for non-identified hadrons. On the gold side on the other hand, the Λ values are significantly above those for charged hadrons. While the h_{ch} R_{cp} exhibits a rise with p_t , no significant transverse momentum dependence in the Λ case is apparent. The difference in transverse momentum dependence of Λ and non-identified hadron R_{cp} is not understood. It might be due to different influences of multiple initial collisions and final state rescattering on baryons and mesons. The p_t dependence of the nuclear modification factor is linked to the centrality dependence of the temperature parameter of the Λ spectra,

discussed in the next section.

The suppression of the yield at forward rapidity with respect to binary collision scaling has been suggested as a possible signature for gluon saturation which implies a limit on the number of small- x gluons (accessible at forward rapidity) by gluon-gluon correlations in the gold nucleus. This might lead to the formation of a state called the color glass condensate (CGC) [28]. This would lead to a suppression of particle production in nucleon-nucleus collisions with respect to nucleon-nucleon collisions.

In the low transverse momentum region covered by the FTPCs, the scaling with the number of binary collisions expected for hard processes should not be valid. The discussion in section 7.2.1 suggests that the Λ and $\bar{\Lambda}$ particle production on the deuteron side scales with the number of deuteron participants, in agreement with the wounded nucleon model. Since the number of binary collisions is very similar to the number of gold participants (see table 3.1), the enhancement observed on the gold side is apparently not due to a wrong choice of scaling. It appears to be caused by nuclear effects that gain in importance with increasing centrality. Since this effect is not observed for charged hadrons, this points to an enhancement of strangeness production due to the presence of the Au nucleus.

7.2 Strangeness Production

In this section, the implications of the dependence of strange particle production on the collision centrality are investigated. The evolution of the strange particle yields with the number of reaction participants is linked to a possible enhancement of strangeness production in nuclear collisions, while the inverse slope parameters contain information about the reaction dynamics.

7.2.1 Centrality Dependence of the Particle Yields

The centrality dependence of the Λ and $\bar{\Lambda}$ particle yields, obtained in section 6.4, is shown in figures 7.3 and 7.4. Also shown are the predictions from HIJING calculations. For Λ there is a fairly good agreement in the most peripheral bin, but the yield on the gold side is underpredicted at higher centralities. This is related to the insufficient baryon transport discussed in the following section. On the deuteron side, the HIJING calculations reproduce the trend of the data. For $\bar{\Lambda}$ there appears to be an overprediction of the yield on the gold side in the most peripheral bin, while the central bin is slightly underpredicted. Again, the deuteron side is quite well reproduced.

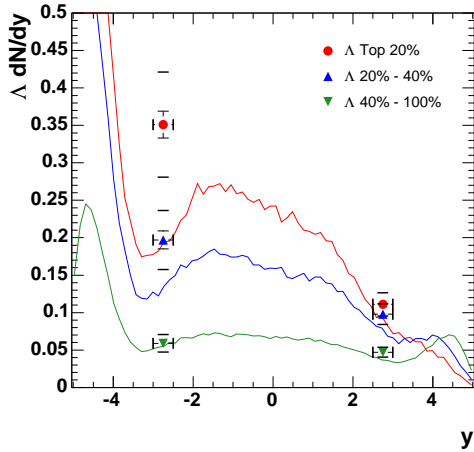


Figure 7.3: Centrality dependence of Λ particle yields at forward and backward rapidity. Also shown are results obtained from HIJING.

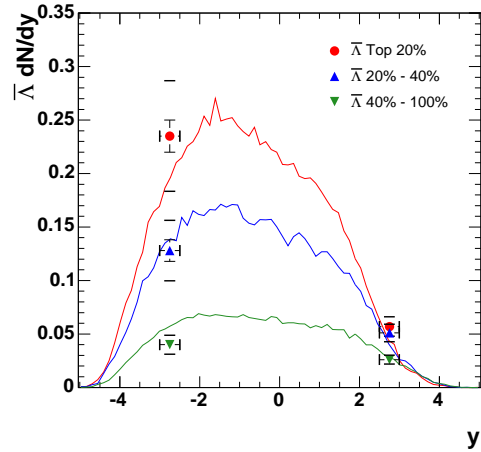


Figure 7.4: Centrality dependence of $\bar{\Lambda}$ particle yields at forward and backward rapidity. Also shown are results obtained from HIJING.

At SPS energies, it was observed that the yield of strange particles in p+Pb collisions increases more with centrality on the Pb side than would be expected from a wounded nucleon model [47]. The wounded nucleon model (WNM) [48] predicts that the particle multiplicity near target and projectile rapidity should scale with the number of wounded target and projectile nucleons, respectively.

Figure 7.5 shows the ratio of the Λ yields in central and mid-central to peripheral events, together with the results from HIJING calculations. A universal systematic error of 10% is assumed for all yield ratios. The same ratio for $\bar{\Lambda}$ is not shown, since the centrality dependence of the Λ and $\bar{\Lambda}$ yield is identical. Thus, the $\bar{\Lambda}$ ratio plot is almost identical to the shown Λ ratio plot. Using the parameters of the different centrality classes summarized in table 3.1, the expectations from the WNM for extreme forward and backward rapidity are calculated. At forward rapidity, the WNM expectation is given by the ratio of the mean number of deuteron participants, while at backward rapidity, the ratio of the mean number of gold participants is expected. These expectations are indicated in figure 7.5 by arrows. Especially on the gold side, the HIJING results are identical to the WNM expectations. This is due to the fact that HIJING uses a superposition of nucleon–nucleon collisions to describe nucleus–nucleus collisions, and thus the wounded nucleon scaling of soft particle production is an inherent feature of the model in d+Au collisions.

On the deuteron side, the data agree well with the HIJING calculations. The ratio at $y = 2.75$ is higher than the WNM limit for the projectile side, which is expected since away from very forward rapidities the number of wounded Au nucleons also contributes. On the gold side, the HIJING calculations do not match the data, especially for the most central bin. The particle yield is also significantly enhanced

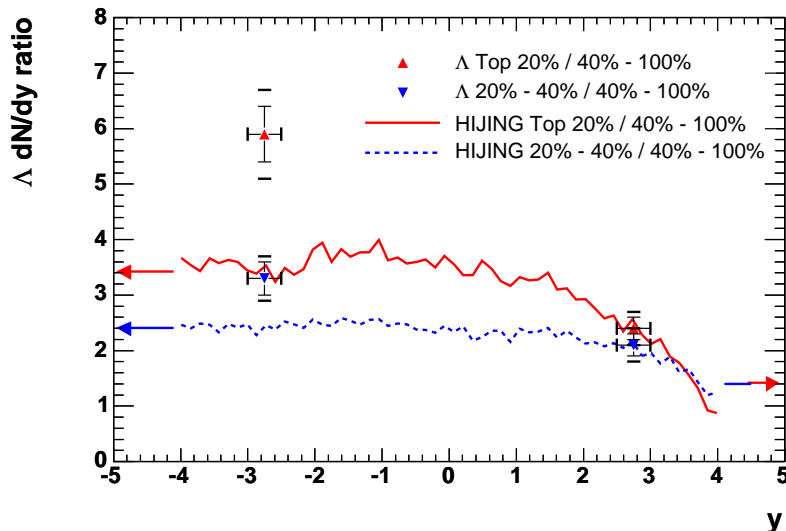


Figure 7.5: Λ yield ratio of central to peripheral and mid-central to peripheral events. Also drawn are the predictions from HIJING. The expectations for extreme forward and backward rapidity from the wounded nucleon model are indicated by the arrows.

with respect to the WNM expectation. Thus, the same behavior that was already observed at the SPS is also observed at RHIC.

The enhancement of the production of strange particles in nucleus–nucleus collisions with respect to nucleon–nucleon and nucleon–nucleus reactions has been proposed as a possible signature for Quark Gluon Plasma formation [9]. Typically, this enhancement is calculated using the number of wounded nucleons in the elementary and in the nucleus–nucleus process. High enhancement factors, especially for multi-strange baryons, have been observed in central Pb+Pb collisions at the SPS [49]. The results at RHIC energies presented here and the SPS results [47] show that a thorough study of the influence of multiple collisions and the influence of target contributions on strange particle production is necessary before an enhancement with respect to the WNM can be attributed to the formation of a QGP.

7.2.2 Centrality Dependence of the Temperature Parameter

From the spectra for the different centrality bins presented in section 6.4, the temperature parameter is extracted with an m_t exponential fit. Based on the previous discussions on differences between the deuteron and the gold side of the collision, differences in the centrality dependence of the temperature parameter on both sides are expected.

Since $\bar{\Lambda}$ are only produced via Λ – $\bar{\Lambda}$ pair production, and Λ are also produced by

associated production, differences in the inverse slope parameter for the two particle species might be expected. On the gold side, the measurements indicate a slightly lower temperature parameter for the $\bar{\Lambda}$ albeit with large systematic errors. On the deuteron side, the temperatures for Λ and $\bar{\Lambda}$ agree within the statistical errors for all centralities.

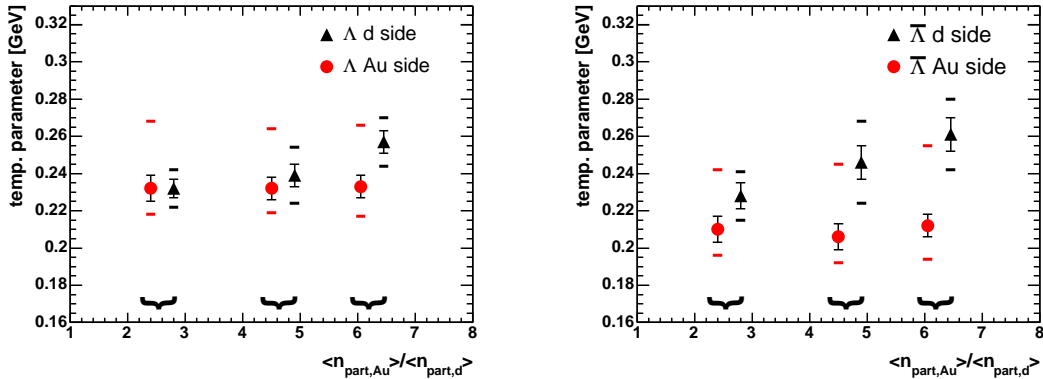


Figure 7.6: Temperature parameter of Λ and $\bar{\Lambda}$ as a function of the ratio of the numbers of mean gold and deuteron participants. The data points are shifted in x direction by ± 0.2 for better visibility.

While the temperature parameter on the gold side does not show a centrality dependence, an increase with centrality is seen on the deuteron side for both particle species. This suggests that the rise in the temperature parameter is driven by the increasing number of collisions the deuteron participants undergo with increasing centrality. Figure 7.6 shows the inverse slopes for Λ and $\bar{\Lambda}$ on both sides as a function of $\langle n_{part,Au} \rangle / \langle n_{part,d} \rangle$, the mean number of gold participants divided by the mean number of deuteron participants. This variable is chosen since it approximates the average number of collisions each deuteron participant suffers in the collision. By applying a constant and a linear fit to the Λ data, the statistical significance of the observed increase was determined. While the constant fit has a χ^2/NDF of 5.2, for a linear rise a χ^2/NDF of 1.0 was obtained.

Qualitatively, HIJING reproduces the behavior of the temperature parameters of the Λ . While there is no significant centrality dependence on the gold side, there is an increase with centrality on the deuteron side. However, the absolute values for the temperature parameter are significantly below the data. On the deuteron side, the HIJING inverse slope parameter increases from ~ 170 MeV to ~ 220 MeV from peripheral to central events. Since the slope parameter changes with transverse momentum, the p_t range of the analysis is used. Contrary to the observation, HIJING predicts a significantly lower and centrality independent temperature parameter for the $\bar{\Lambda}$ on the deuteron side. On the gold side, the $\bar{\Lambda}$ temperature is similar to the

Λ temperature, which is expected since in HIJING the gold side in the acceptance region of FTPC East is dominated by pair production.

7.3 Baryon Transport and Stopping

Since the Λ particle is a singly strange baryon and contains a ud quark pair like the proton and the neutron, it is sensitive to mechanisms of baryon transport which imply the strip-off of one, two or three quarks from the incoming baryon, as described in section 2.4.2. By comparing to model calculations, the contributions of different processes can be investigated. The constraint of baryon number conservation in the reaction can be exploited to estimate the mean rapidity loss of baryons on the deuteron side of the collision.

7.3.1 Model Comparisons

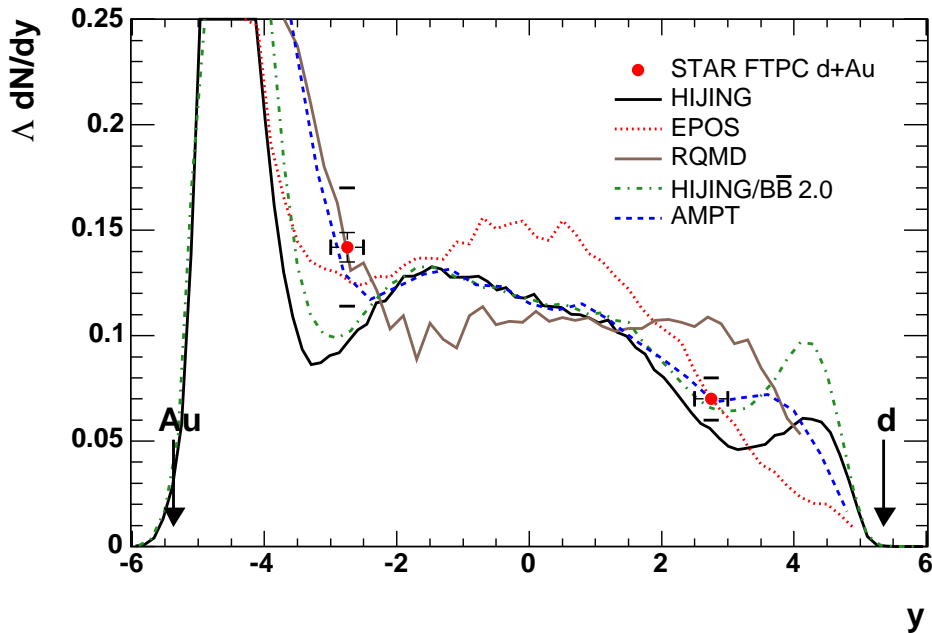


Figure 7.7: Λ particle yield dN/dy as a function of rapidity for d+Au minimum bias events. The horizontal bar denotes the width of the rapidity bin used in the analysis. The vertical error bars show the statistical and systematic errors. Beam rapidities are indicated by arrows.

Figure 7.7 shows dN/dy for Λ on both sides of the collision together with the model calculations. It is apparent that the different models show qualitatively different behavior. The HIJING models have a distinct peak around $y \sim 4$ originating from

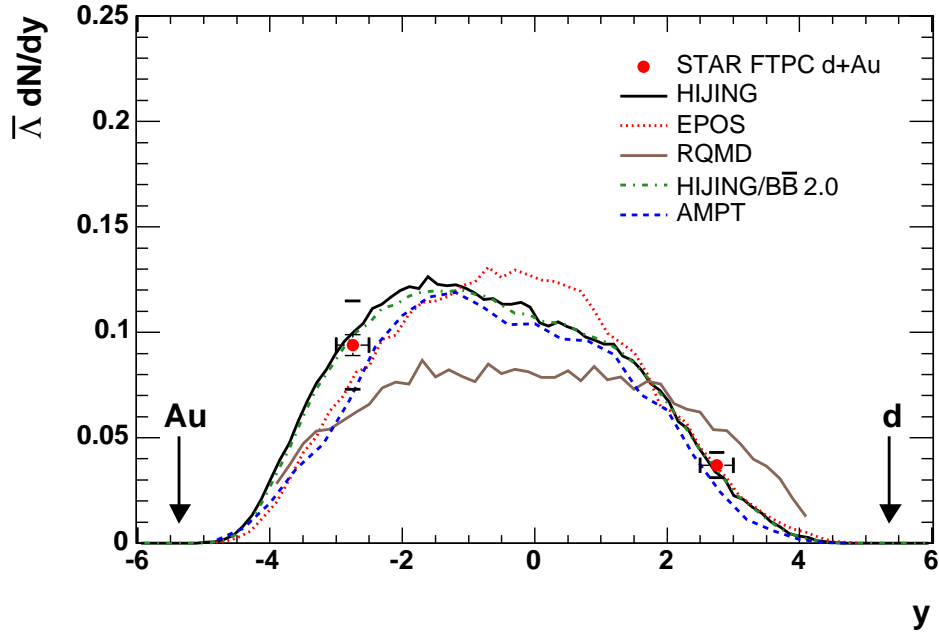


Figure 7.8: $\bar{\Lambda}$ particle yield dN/dy as a function of rapidity for d+Au minimum bias events. Beam rapidities are indicated by arrows.

the baryon content of the deuteron, while this is less pronounced in AMPT and not present in EPOS and RQMD. On the Au side, all models show a rise in dN/dy for Λ caused by the baryon content of the nucleus, albeit at different rapidities. This reflects differences in the mechanisms for baryon transport employed in the models.

On the gold side of the collision, AMPT, EPOS and RQMD are in agreement with the data, while the HIJING models underpredict the yield. On the deuteron side, RQMD clearly overpredicts the data, while HIJING appears to be too low. The three other models are in good agreement with the measurement.

The yield dN/dy for $\bar{\Lambda}$ with the model results is shown in figure 7.8. In general, there is good agreement between the models especially on the deuteron side. However, RQMD does not agree with the other models nor with the measurement. The data agree with EPOS, AMPT, HIJING and HIJING/B \bar{B} .

By studying the net Λ yield ($\Lambda - \bar{\Lambda}$), the contributions from pair production are removed. Figure 7.9 shows the net Λ yield and model calculations. Here, the differences in baryon transport between the different models are clearly visible. In both HIJING models, the net Λ yield goes to zero at $y \sim -3$. A consequence of this is that in HIJING there is no baryon transport from the gold side to mid-rapidity. This is in clear contradiction to the data. AMPT and EPOS have significant baryon transport from the Au side to mid-rapidity and give a good description of the data.

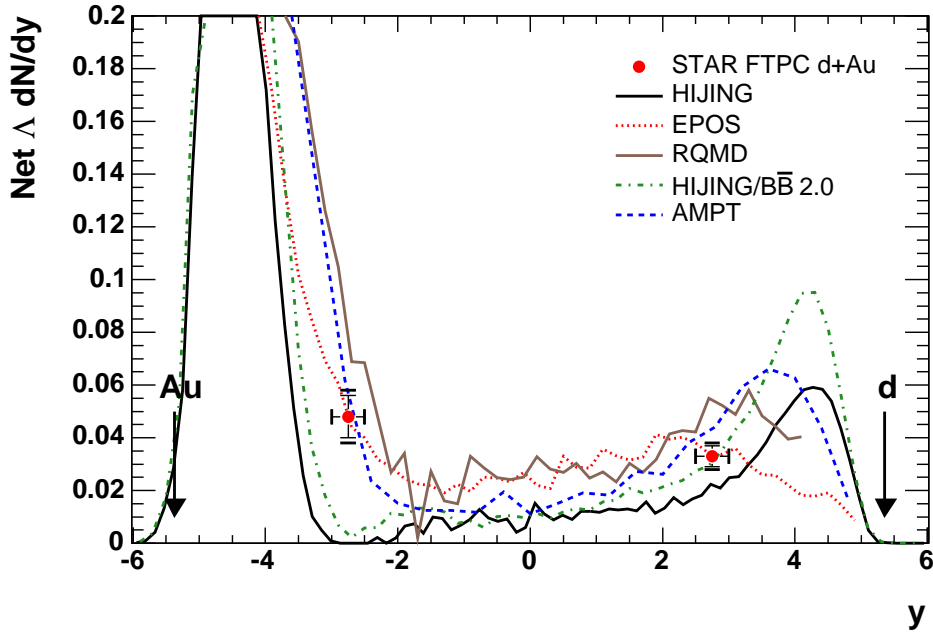


Figure 7.9: Net Λ yield ($\Lambda - \bar{\Lambda}$) dN/dy as a function of rapidity for d+Au minimum bias events. The rapidity of both beams is also indicated as a reference.

The deuteron side of the collision is reproduced by EPOS and HIJING/ $B\bar{B}$. AMPT slightly overpredicts the net Λ yield on the deuteron side.

The $\bar{\Lambda}/\Lambda$ ratio together with the model predictions is shown in figure 7.10. For this ratio a preliminary mid-rapidity result is already available. The work on the efficiency corrections for the mid-rapidity results was not completed by the time this thesis was written. Thus, no mid-rapidity yields are presented here. However, it is already known that the efficiency for Λ and $\bar{\Lambda}$ is almost equal, so the $\bar{\Lambda}/\Lambda$ ratio can be determined without the knowledge of the absolute efficiency. The preliminary number is 0.84 ± 0.01 (stat) ± 0.03 (syst) [42].

The model comparisons show that the measurement on the deuteron side is reasonably reproduced by all used models with HIJING slightly above and AMPT slightly below the data point. On the gold side, only AMPT and EPOS reproduce the data. The lacking baryon transport from the gold side toward mid-rapidity in HIJING is also apparent here. The HIJING models reach a $\bar{\Lambda}/\Lambda$ ratio of 1 at $y \sim -3$, corresponding to the predicted vanishing of the net Λ yield in that region. Since there are considerable differences between EPOS and AMPT predictions for the mid-rapidity net Λ yield, this number will be able to decide between the two models.

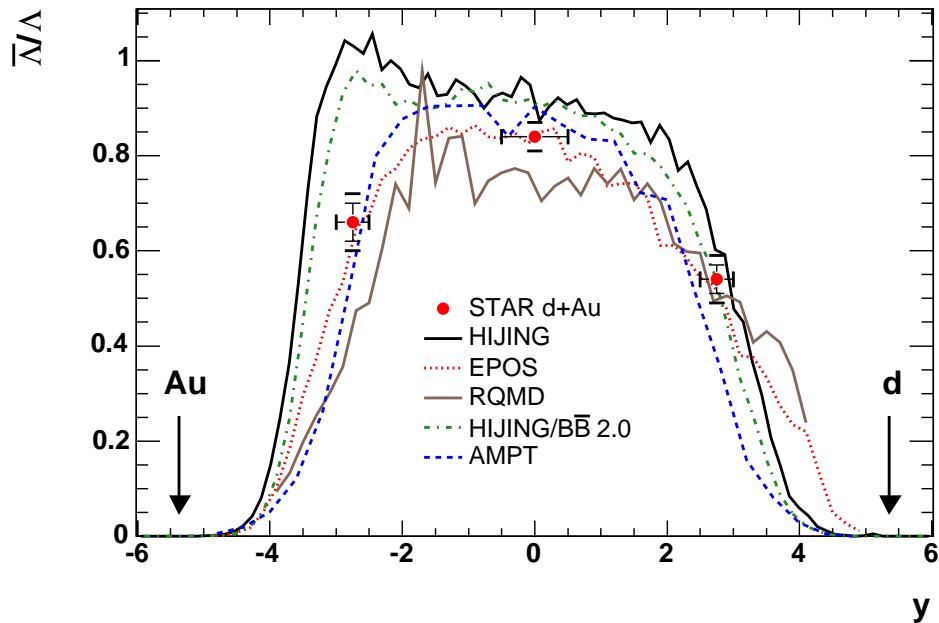


Figure 7.10: $\bar{\Lambda}/\Lambda$ ratio as a function of rapidity. The mid-rapidity point of 0.84 is a preliminary number from STAR [42]. The rapidity of both beams is also indicated as a reference.

7.3.2 Mechanisms of Baryon Transport

By comparing to a range of model calculations, different mechanisms of baryon transport are investigated. The asymmetry of d+Au collisions is used to investigate the contribution of different processes to baryon stopping. Multiple collisions of projectile nucleons with target nucleons as well as not directly participating cold nuclear matter and rescattering in the final phase of the reaction will contribute to baryon transport.

On the deuteron side the participants have suffered several collisions, but no cold nuclear matter is present for later rescattering of the produced particles. On the gold side, each participating nucleon only underwent one collision, but the surrounding hadronic matter can lead to further stopping and particle production. The models used for comparisons include different mechanisms, so the observations from section 7.3.1 can be used to disentangle the different contributions.

The employed models have been thoroughly introduced in section 3.4.4. Here, the important features that govern their description of nuclear stopping are summarized. HIJING uses a superposition of individual nucleon–nucleon collisions to describe nucleus–nucleus collisions. Baryon transport is the consequence of the string model mechanism of diquark preserving and diquark breaking processes. In HIJING/B \bar{B} , the inclusion of baryon junctions in addition to baryon number transport via string

breaking leads to higher stopping. AMPT combines the HIJING approach with a hadronic transport stage in the final state of the reaction. EPOS is also based on a string model approach. It has no rescattering stage, but in addition to the individual nucleon–nucleon interactions, projectile and target nucleon excitations take the influence of the nuclei into account. RQMD provides a thorough treatment of hadronic transport, but is lacking a complete description of the initial collisions.

The comparison of the net Λ yield and the $\bar{\Lambda}/\Lambda$ ratio to the model calculations show that the deuteron side is best reproduced by EPOS and HIJING/B \bar{B} , while the gold side is described by AMPT and EPOS. While AMPT is quite close to the data also on the deuteron side, the HIJING models fail completely in reproducing the gold side results. RQMD does not reproduce the asymmetry of the data and thus deviates from the measurements on both sides of the collision. However, the Λ yield on the gold side is reasonably described.

This suggests that stopping on the deuteron side is caused by multiple independent collisions of the deuteron participants with the gold constituents. The addition of baryon junctions to the pure HIJING model improves the performance of the model. This indicates that baryon number transport can also be associated to gluonic structures without slowing down valence quarks of the incoming nucleons. As expected, hadronic transport and rescattering do not play important roles on the deuteron side of the collision.

The baryon transport on the gold side has a different origin. The failure of the HIJING models, even with additional stopping through baryon junctions, shows that the nucleon–nucleon collisions of participants alone are not sufficient to describe the observed baryon transport. Here, effects from the target nucleus or later hadronic rescattering are needed to explain the observations.

7.3.3 Rapidity Loss and Stopping

The energy loss of colliding nuclei determines the amount of energy that is available for particle production in the collision. The energy deposited by nuclear stopping is essential for the formation of a quark gluon plasma in collisions of heavy nuclei.

The BRAHMS experiment obtained a mean rapidity loss of $\delta y \sim 2$ in central Au+Au collisions at $\sqrt{s_{NN}} = 200$ GeV [50]. This corresponds to an energy loss of around 70 GeV per participant. Contrary to full transparency and an extended boost invariant region suggested in [5], no net baryon free central rapidity region is observed.

The average rapidity loss of incoming baryons in nuclear collisions can be used as a measure of the stopping power of nuclear matter. In principle, this requires a full reconstruction of all baryons in any given event, which is usually not possible. However, the measurement of baryon distributions over a limited range already provides strong constraints on the overall net baryon distribution and can thus be

used to obtain an estimate of the nuclear stopping power. This measurement is only possible on the deuteron side, as discussed below.

To use the measurement of the net Λ yield presented here for a quantitative study of baryon stopping, a relation between the net Λ yield and the net baryon yield has to be established. This is done using preliminary Λ data [42] as well as proton and anti-proton data [51, 52] obtained with the TOF detector at mid-rapidity. With these results, a net Λ to net proton ratio of ~ 0.25 is obtained. The total net baryon number is given by the sum of net protons, neutrons, Λ , Σ^+ , Σ^- and higher mass hyperons. It is assumed that the number of net protons is equal to the number of net neutrons, since the deuteron consists of one proton and one neutron. Since all unstable baryons decay with either a proton or a neutron in the decay channel, the inclusive net proton yield (not corrected for feeddown) measured by the TOF detector is half of the total net baryon yield. The feeddown contribution in the TOF detector is around 20% [51]. Thus the total net baryon yield at mid-rapidity is given by

$$\text{net baryons} = 2.5 \text{ net protons} = 10 \text{ net } \Lambda. \quad (7.3)$$

It is assumed that this relation holds over all rapidity, which is supported by HIJING simulations.

In order to extract the average rapidity loss of incoming baryons, additional assumptions have to be made. It is not necessary that all baryons from the deuteron end up with a positive rapidity while no baryons from the gold get transported into that region. Since gold nucleons only suffer one collision each, it is unlikely that many baryons do not only lose a significant amount of their initial energy but even get reflected and travel into the deuteron direction after the reaction. On the other hand, this scenario might be significantly more likely on the deuteron side, where the participating nucleons suffer multiple collisions. However, the number of available baryons is much higher on the Au side. It is not possible to distinguish which baryon originated from which projectile, so here it is assumed that all baryons are confined to their respective side in rapidity. Thus the integral of the net baryon rapidity distribution from mid-rapidity to deuteron rapidity should correspond to the number deuteron participants. Using the relation 7.3 and the integral of the model predictions for the net Λ yield shown in figure 7.9, this assumption is confirmed to a precision of 20%. In addition, it is assumed that the net baryon distribution is a linear function of rapidity in the covered rapidity range from 0 to 2.75. This assumption is supported by the model calculations shown in figure 7.9.

Figure 7.11 shows the minimum bias net baryon yields obtained from the mid-rapidity TOF proton results and the net Λ yields at forward rapidity presented in this thesis. The distribution is fitted with a six order polynomial (pol6) which has the integral of the mean number of deuteron participants $n_{part,d} = 1.6$ and is 0 at a rapidity of 5.2, the rapidity of a Λ particle with a longitudinal momentum of 100

GeV/c. A smooth behavior of the fit in the region between the two measurements is ensured by adding interpolated values that are included in the fit.

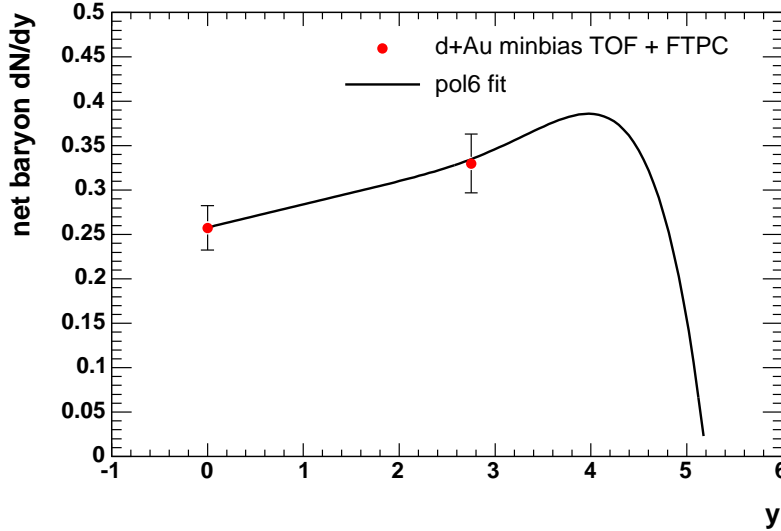


Figure 7.11: Net baryon yield in d+Au minimum bias events at mid-rapidity and $y = 2.75$ fitted with a 6th order polynomial.

From the fit, the mean rapidity of the net baryons after the collision can be extracted by integration. The average rapidity loss of incoming nucleons of the deuteron is given by the difference of the rapidity of a 100 GeV/c Λ and the obtained mean rapidity. The mean rapidity given by the fit is 2.6, corresponding to a mean rapidity loss $\delta y = 2.6$. An estimate of the errors is discussed below.

The number of net baryons in the range from mid-rapidity to 2.75 is 0.8, which is half of the total baryon number present on the deuteron side of minimum bias d+Au collisions. This shows that with a measurement over a limited rapidity range, a significant constraint on the total distribution is possible. On the gold side on the other hand, the stopping is significantly lower, and thus only a small fraction (around 10% to 15%) of the total available number of baryons is measured in the range from -2.75 to mid-rapidity. In addition, a linear interpolation is probably not warranted there. This restricts the quantitative analysis of the rapidity loss to the deuteron side, which is sensitive to the stopping power of heavy nuclei.

Using the centrality dependent analysis of the net Λ yield in the FTPCs and the proton and anti-proton yield at mid-rapidity, the centrality dependence of the stopping power of a gold nucleus is investigated. Figure 7.12 shows the centrality dependent net baryon yields at mid-rapidity and at $y = 2.75$ together with pol6 fits. The integrals of the fit functions are set to 1.4 for peripheral, to 1.9 for mid-central and to 2.0 for central events, corresponding to the number of participating deuteron

nucleons in the respective centrality classes. Analogous to the method used for the minimum bias events, a mean rapidity loss δy of 2.1, 2.9 and 3.3 is determined from the fit for peripheral, mid-central and central events, respectively.

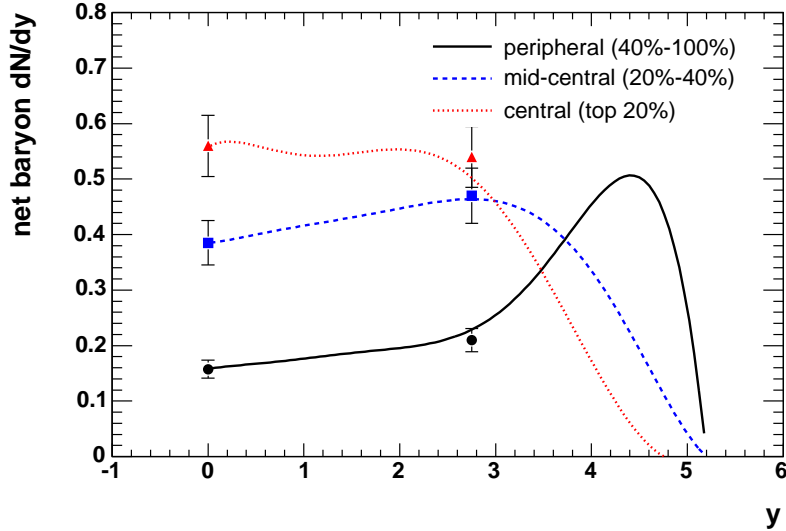


Figure 7.12: Net baryon yield on the deuteron side and pol6 fit as a function of centrality. An interesting feature of the distribution of net baryons suggested by the fit is the absence of a peak in the deuteron fragmentation region in mid-central and central events. This indicates a very high degree of stopping.

A surprising feature of the fitted curves in the figure is that no peak in the fragmentation region is present in the mid-central and especially in the central events. This is due to the constraint of the integral of the fit to the number of deuteron participants. The distribution of the net baryon density suggested by the fitted curves implies significant stopping in central d+Au collisions and consequently very little transparency, which is in contradiction to previous expectations [5] and to the observed saturation of the stopping in central Au+Au collisions at $\sqrt{s_{NN}} = 200$ GeV [50]. It is possible that the stopping in d+Au collisions is overestimated if a significant number of baryons from the gold side gets transported to positive rapidity. This would require baryon transport over more than 5 units of rapidity with only a single initial collision and subsequent final-state interactions. All models used in this thesis point to a minimum of the net baryon density at a rapidity of less than -1.5 in minimum bias events, which would rule out this scenario. The net Λ yields predicted by EPOS and RQMD (see figure 7.9) show a behavior which is consistent with the absence of a peak in the deuteron fragmentation region.

There are sizable uncertainties in the determination of the mean rapidity loss. The major contributions are expected to originate from the uncertainty in the determination of the net baryon yield in the range from mid-rapidity to $y = 2.75$ and from

the extrapolation of the distribution in the region above $y = 2.75$. The uncertainty stemming from the yield determination is estimated by assuming a 25% error on the net baryon yield in the covered rapidity region. This includes the uncertainties introduced by the conversion of the measured net Λ yield to the net baryon yield. This error is referred to as the yield contribution. The uncertainty introduced by the extrapolation of the net baryon yield beyond $y = 2.75$ is estimated by assuming two extreme possibilities. The not measured baryons are assumed to be located either all at a rapidity of 3 or all at a rapidity of 5. This contribution is referred to as the distribution error.

Table 7.1 summarizes the mean rapidity loss together with the errors determined via the above methods. Also included is the mean number of collisions n_{coll} that a deuteron nucleon suffers in the given centrality class, determined by the ratio of binary collisions and the number of deuteron participants. These numbers were calculated within the Glauber model included in the HIJING event generator and are summarized in table 3.1.

| centrality class | n_{coll} | mean rapidity loss δy |
|------------------|------------|--|
| minimum bias | 4.7 | 2.6 ± 0.3 (yield) ± 0.5 (dist) |
| top 20% | 7.5 | 3.3 ± 0.5 (yield) ± 0.2 (dist) |
| 20% – 40% | 5.4 | 2.9 ± 0.4 (yield) ± 0.4 (dist) |
| 40% – 100% | 2.9 | 2.1 ± 0.2 (yield) ± 0.6 (dist) |

Table 7.1: Mean rapidity loss of deuteron baryons for minimum bias events and all three centrality classes.

These results show that the mean rapidity loss per participating baryon increases with increasing centrality, as expected from the increasing number of collisions. A comparison to the result obtained by BRAHMS for central Au+Au collisions shows that the stopping measured in the nucleus–nucleus system appears to be similar to the stopping in peripheral d+Au collisions. This is unexpected since the average number of collisions per participant n_{coll} in central Au+Au collisions is around 6, which is similar to that in mid–central d+Au collisions.

This behavior can be explained by a reduction of the stopping power of nucleons that have already participated in at least one collision. While the nucleons from the deuteron in a d+Au collision collide with nucleons from the gold nucleus that have not participated in a previous reaction, this is not true in Au+Au collisions. In a central Au+Au collision, on average 5 out of the 6 interactions per participant will be with a nucleon that has suffered previous collisions, and thus might have changed its properties. The results presented here indicate that the stopping in these reactions is reduced with respect to collisions of two unhurt nucleons. This would also explain why a distinct peak of the net baryon distribution in the fragmentation region is

present in central Au+Au collisions [50], while no such peak is observed in central d+Au collisions in the deuteron fragmentation region.

The fact that the stopping in nucleon–nucleus collisions is larger than the stopping in nucleus–nucleus collisions at comparable energies is also apparent in earlier measurements. In the first measurement of nuclear stopping power at relativistic energies a mean rapidity loss of 2.5 ± 0.5 was observed in central p+Pb collisions with a proton energy of 100 GeV on a stationary target [53]. The NA49 experiment obtained a mean rapidity loss of 1.76 ± 0.05 in central Pb+Pb collisions with a beam energy of 158 GeV per nucleon on a fixed target [54]. A comparison of the net proton distributions in p+Pb and Pb+Pb collisions by NA49 also indicates significantly more stopping in the asymmetric system [55].

Chapter 8

Conclusion and Outlook

In the course of preparing this thesis, the Forward Time Projection Chambers of the STAR experiment at the Relativistic Heavy Ion Collider were maintained and operated during two running periods. A simulation framework for the determination of detector properties was developed. This embedding procedure merges simulated particle tracks with real data to provide a realistic environment including detector background for the study of tracking efficiency and momentum resolution.

Using the dataset of deuteron–gold collisions at an energy of $\sqrt{s_{NN}} = 200$ GeV recorded in 2003, the production of Λ particles at forward rapidity was studied. The FTPCs in STAR provide the unique possibility to measure neutral strange particles at high forward and backward rapidity at RHIC.

An analysis procedure based on the detection of displaced decay vertices and background rejection with geometric cuts was developed to extract Λ and $\bar{\Lambda}$ signals. Using the embedding framework, the efficiency for the reconstruction of these particles was determined and used in the determination of corrected particle spectra.

The nuclear modification factor of Λ particles shows an increasing suppression with centrality on the deuteron side, consistent with expectations in the case of color glass condensate formation. In the low p_t region covered by the FTPCs, this suppression can also be explained by the fact that scaling with the number of binary collisions is not applicable and a scaling with the number of deuteron participants is more appropriate. On the gold side, an enhancement is seen which cannot be explained by the scaling implied in the calculation of the modification factor. This increase with collision centrality is directly linked to the enhancement of the Λ and $\bar{\Lambda}$ yield on the gold side with respect to the wounded nucleon model expectations. On the deuteron side, the centrality dependence of the particle yields is consistent with the wounded nucleon model. This demonstrates that a thorough understanding of nuclear effects on the particle production is necessary before an enhancement of strange particle production with respect to wounded nucleon scaling in nucleus–nucleus collisions can be used as an unambiguous indicator of Quark Gluon Plasma

creation.

The centrality dependence of the inverse slope parameter of the Λ and $\bar{\Lambda}$ spectra show that the increasing number of collisions of the deuteron participants leads to an increase of the temperature parameter on the deuteron side. On the gold side, where the number of participants increases with centrality, but the number of collisions per participant stays approximately constant, the temperature parameter is independent of the collision centrality.

The $\bar{\Lambda}/\Lambda$ ratio and the net Λ yield suggest significant stopping in d+Au collisions at RHIC energies. The asymmetries between the gold and the deuteron side of the collision point to contributions from different processes of baryon transport. The comparison to a range of models indicates that the baryon transport on the deuteron side is caused by multiple independent collisions of the deuteron participants with gold nucleons. On the gold side, a superposition of individual nucleon–nucleon processes is not sufficient to explain the observed amount of stopping. Here, the inclusion of nuclear effects, either as target nucleon excitations or as hadronic rescattering in later stages of the collision, is necessary.

A first measurement of the rapidity loss of baryons on the deuteron side in d+Au collisions indicates that transparency is not reached in these reactions. The stopping power of the nucleus increases with collision centrality. The rapidity loss is larger in nucleon–nucleus collisions than in nucleus–nucleus collisions, possibly due to the modifications nucleons experience in multiple collisions.

To further strengthen the studies of the influence of nuclear effects on the strange particle production at forward rapidities, the analysis of proton–proton collisions would be very useful. This requires a sizable minimum bias dataset recorded with fully operational FTPCs. Currently, such a dataset is not available, but might become so in the near future.

The study of forward Λ production in nucleus–nucleus collisions would complete the picture. However, given the large combinatoric background in these events, it is unclear whether such an analysis can be performed reliably. This can be investigated with the big Au+Au dataset taken in 2004 and the Cu+Cu dataset anticipated for 2005. Measurements with d+Au collisions at different energies could be used for a thorough study of nuclear stopping power in asymmetric collisions.

Appendix A

Kinematic Variables

For the discussion of phenomena related to heavy ion collisions, a set of kinematic variables is used that is introduced here. In this discussion the speed of light will be set to unity, a common approach in high energy physics. Particles are characterized by their mass m and their momentum \vec{p} . Of special interest are often the momentum in beam direction, p_z , and the transverse momentum p_t ,

$$\vec{p} = (p_x, p_y, p_z) \qquad p_t = \sqrt{p_x^2 + p_y^2}. \qquad (\text{A.1})$$

In discussions on particle dynamics, the transverse mass m_t is often used since a thermal particle spectrum follows an exponential distribution in transverse mass. It is defined as

$$m_t = \sqrt{p_t^2 + m_0^2}. \qquad (\text{A.2})$$

The rapidity is a measure of the forward momentum of a particle. In the non-relativistic limit, it is equal to the particle velocity divided by the speed of light. An advantage of the rapidity is that it is additive under Lorentz transformations along the beam direction, making it easy to use. Rapidity is defined as

$$y = \frac{1}{2} \ln \left(\frac{E + p_z}{E - p_z} \right), \qquad (\text{A.3})$$

where E is the particle energy.

To determine the rapidity of a particle, its energy (or mass) and momentum have to be known. Often, an identification of a particle is not possible experimentally, so that only its momentum is known. In that case, the pseudorapidity can be used, which is defined as

$$\eta = \frac{1}{2} \ln \left(\frac{p + p_z}{p - p_z} \right). \qquad (\text{A.4})$$

In the limit of vanishing particle mass, rapidity y is equal to pseudorapidity η . That means that for $p \gg m$ η is a good approximation for y . The pseudorapidity depends

only on the emission angle Θ of the particle with respect to the beam direction,

$$\eta = -\ln [\tan(\Theta/2)]. \quad (\text{A.5})$$

It is thus a purely geometrical variable. The pseudorapidity is often used to describe the acceptance of detectors.

Appendix B

The STAR Coordinate System

The global STAR coordinate system used in this thesis has its origin in the nominal interaction point, in the center of the interaction region of the two beams. The z axis is given by the beam direction. In the STAR experimental area, this coincides with the East–West direction. The two RHIC accelerator rings are labeled "blue" and "yellow". Positive z is towards west, which is the direction of the "blue" beam. In the 2003 deuteron–gold beam time, the deuterons were accelerated in the "blue" while gold was accelerated in the "yellow" ring. The two forward TPCs are east and west of the nominal interaction vertex, and thus labeled "FTPC East" and "FTPC West". Figure B.1 illustrates the geometry in the STAR experimental hall.

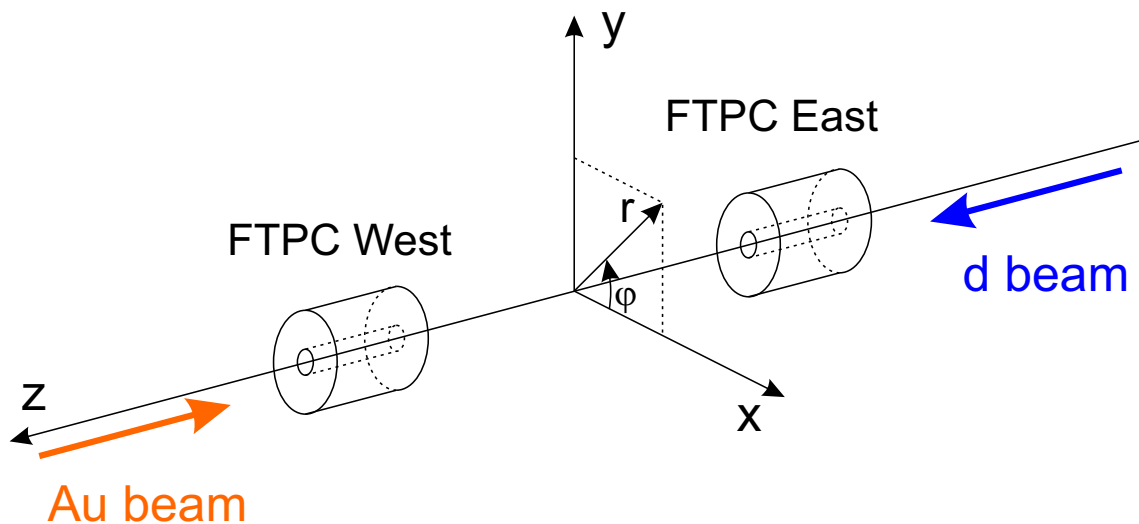


Figure B.1: The STAR coordinate system, with the beam setup used for the 2003 deuteron–gold run.

Bibliography

- [1] D. J. Gross and F. Wilczek, *Ultraviolet behavior of non-abelian gauge theories*, Phys. Rev. Lett. **30**, 1343 (1973).
- [2] D. H. Politzer, *Reliable perturbative results for strong interactions*, Phys. Rev. Lett. **30**, 1346 (1973).
- [3] K. G. Wilson, *Confinement of quarks*, Phys. Rev. **D10**, 2445 (1974).
- [4] K. Rajagopal, *The phases of QCD in heavy ion collisions and compact stars*, Acta Phys. Polon. **B31**, 3021 (2000).
- [5] J. D. Bjorken, *Highly relativistic nucleus-nucleus collisions: The central rapidity region*, Phys. Rev. **D27**, 140 (1983).
- [6] PHOBOS, B. B. Back *et al.*, *The significance of the fragmentation region in ultrarelativistic heavy ion collisions*, Phys. Rev. Lett. **91**, 052303 (2003).
- [7] A. Capella, *Can one understand stopping in heavy ion collisions without an anomalous mechanism?*, Phys. Lett. **B542**, 65 (2002).
- [8] D. Kharzeev, *Can gluons trace baryon number?*, Phys. Lett. **B378**, 238 (1996).
- [9] J. Rafelski and B. Müller, *Strangeness production in the quark - gluon plasma*, Phys. Rev. Lett. **48**, 1066 (1982).
- [10] STAR, J. Adams *et al.*, *Evidence from d+Au measurements for final-state suppression of high p_t hadrons in Au+Au collisions at RHIC*, Phys. Rev. Lett. **91**, 072304 (2003).
- [11] C.-Y. Wong, *Introduction to High-Energy Heavy-Ion Collisions* (World Scientific, 1994).
- [12] J. Letessier and J. Rafelski, *Hadrons and Quark-Gluon Plasma* (Cambridge University Press, 2002).
- [13] M. Harrison, T. Ludlam and S. Ozaki, *RHIC project overview*, Nucl. Instrum. Meth. **A499**, 235 (2003).

-
- [14] H. Hahn *et al.*, *The RHIC design overview*, Nucl. Instrum. Meth. **A499**, 245 (2003).
- [15] BRAHMS, F. Videbaek, *The BRAHMS experiment at RHIC*, Nucl. Phys. **A566**, 299c (1994).
- [16] PHOBOS, B. Wyslouch, *The PHOBOS experiment at RHIC and AGS*, Nucl. Phys. **A566**, 305c (1994).
- [17] PHENIX, J. C. Gregory *et al.*, *The PHENIX experiment at RHIC*, Nucl. Phys. **A566**, 287c (1994).
- [18] STAR, J. W. Harris, *The STAR experiment at the relativistic heavy ion collider*, Nucl. Phys. **A566**, 277c (1994).
- [19] STAR, K. H. Ackermann *et al.*, *STAR detector overview*, Nucl. Instrum. Meth. **A499**, 624 (2003).
- [20] CERES, G. Agakishiev *et al.*, *First results from the CERES radial TPC*, Nucl. Phys. **A661**, 673 (1999).
- [21] J. H. Putschke, *Teilchenproduktion und anisotrope Flussmessungen in den Vorwärts-Spuredriftkammern des STAR Experimentes*, PhD thesis, TU München, 2004.
- [22] M. D. Oldenburg, *Schnelle Spurrekonstruktion und Messung von anisotropem Fluss mit den Vorwärts-Spuredriftkammern des Experimentes STAR*, PhD thesis, TU München, 2001.
- [23] K. H. Ackermann *et al.*, *The forward time projection chamber (FTPC) in STAR*, Nucl. Instrum. Meth. **A499**, 713 (2003).
- [24] A. Huber *et al.*, *Hydrogen-deuterium 1s-2s isotope shift and the structure of the deuteron*, Phys. Rev. Lett. **80**, 468 (1998).
- [25] L.-W. Chen, C. M. Ko and B.-A. Li, *Light cluster production in intermediate energy heavy-ion collisions induced by neutron-rich nuclei*, Nucl. Phys. **A729**, 809 (2003).
- [26] PHOBOS, B. B. Back *et al.*, *Pseudorapidity distribution of charged particles in d+Au collisions at $\sqrt{s_{NN}} = 200$ GeV*, Phys. Rev. Lett. **93**, 082301 (2004).
- [27] M. L. Miller, *Measurement of Jets and Jet Quenching at RHIC*, PhD thesis, Yale University, 2003.
- [28] D. Kharzeev, E. Levin and M. Nardi, *QCD saturation and deuteron nucleus collisions*, Nucl. Phys. **A730**, 448 (2004).

- [29] X.-N. Wang and M. Gyulassy, *HIJING: A Monte Carlo model for multiple jet production in $p+p$, $p+A$ and $A+A$ collisions*, Phys. Rev. **D44**, 3501 (1991).
- [30] S. E. Vance and M. Gyulassy, *Anti-hyperon enhancement through baryon junction loops*, Phys. Rev. Lett. **83**, 1735 (1999).
- [31] PHENIX, K. Adcox *et al.*, *Measurement of the lambda and antilambda particles in Au+Au collisions at $\sqrt{s_{NN}} = 130$ GeV*, Phys. Rev. Lett. **89**, 092302 (2002).
- [32] V. Topor–Pop *et al.*, *Baryon junction loops in HIJING/Banti-B v2.0 and the baryon/meson anomaly at RHIC*, nucl-th/0407095 (2004).
- [33] B. Zhang, C. M. Ko, B. A. Li and Z. W. Lin, *A multi-phase transport model for nuclear collisions at RHIC*, Phys. Rev. **C61**, 067901 (2000).
- [34] Z. W. Lin and C. M. Ko, *Deuteron-nucleus collisions in a multi-phase transport model*, Phys. Rev. **C68**, 054904 (2003).
- [35] H. J. Drescher, M. Hladik, S. Ostapchenko and K. Werner, *A unified treatment of high energy interactions*, J. Phys. **G25**, L91 (1999).
- [36] K. Werner, F. M. Liu and T. Pierog, *Proton proton and deuteron gold collisions at RHIC*, hep-ph/0405274 (2004).
- [37] H. Sorge, *Flavor production in Pb(160 AGeV) on Pb collisions: Effect of color ropes and hadronic rescattering*, Phys. Rev. **C52**, 3291 (1995).
- [38] H. Hümmeler, *Development of a Detector and Data Analysis for Particles in the Rapidity Range $2.5 < |y| < 4$ at the Relativistic Heavy Ion Collider in Brookhaven*, PhD thesis, TU München, 2000.
- [39] R. Hagedorn, *Multiplicities, pt distributions and the expected hadron \rightarrow quark-gluon phase transition*, Riv. Nuovo Cimento **6**, 10 (1983).
- [40] STAR, F. Simon, *Mean transverse momentum at forward rapidity in STAR*, Prog. Part. Nucl. Phys. **53**, 261 (2004).
- [41] NA49, A. Mischke *et al.*, *Lambda production in central Pb+Pb collisions at CERN-SPS energies*, J. Phys. **G28**, 1761 (2002).
- [42] STAR Strangeness Physics Working Group, *Preliminary mid-rapidity d+Au results*, private communication, 2004.
- [43] STAR, J. Adams and M. Heinz, *Neutral strange particle production at mid unit rapidity in $p+p$ collisions at $\sqrt{s_{NN}} = 200$ GeV*, nucl-ex/0403020 (2004).
- [44] NA49, T. Susa, *Cascade production in $p+p$, $p+A$ and $A+A$ interactions at 158 AGeV*, Nucl. Phys. **A698**, 491 (2002).

-
- [45] BRAHMS, I. Arsene *et al.*, *On the evolution of the nuclear modification factors with rapidity and centrality in d+Au collisions at $\sqrt{s_{NN}} = 200$ GeV*, Phys. Rev. Lett. **93**, 242303 (2004).
- [46] J. W. Cronin *et al.*, *Production of hadrons at large transverse momentum at 200, 300 and 400 GeV*, Phys. Rev. **D11**, 3105 (1975).
- [47] K. Kadija, *Strange particle production in p+p, p+Pb and Pb+Pb interactions from NA49*, J. Phys. **G28**, 1675 (2002).
- [48] A. Bialas *et al.*, *Multiplicity distributions in nucleus-nucleus collisions at high energies*, Nucl. Phys. **B111**, 461 (1976).
- [49] WA97, E. Andersen *et al.*, *Strangeness enhancement at mid-rapidity in Pb+Pb collisions at 158 AGeV/c*, Phys. Lett. **B449**, 401 (1999).
- [50] BRAHMS, I. Bearden *et al.*, *Nuclear stopping in Au+Au collisions at $\sqrt{s_{NN}} = 200$ GeV*, Phys. Rev. Lett. **93**, 102301 (2004).
- [51] STAR, J. Adams *et al.*, *Pion, kaon, proton and anti-proton transverse momentum distributions from p+p and d+Au collisions at $\sqrt{s_{NN}} = 200$ GeV*, nucl-ex/0309012 (2003).
- [52] STAR Spectra Physics Working Group, *Proton and anti-proton yields in d+Au collisions obtained with the TOF detector*, private communication, 2004.
- [53] W. Busza and A. S. Goldhaber, *Nuclear stopping power*, Phys. Lett. **B139**, 235 (1984).
- [54] NA49, H. Appelshäuser *et al.*, *Baryon stopping and charged particle distributions in central Pb+Pb collisions at 158 GeV per nucleon*, Phys. Rev. Lett. **82**, 2471 (1999).
- [55] NA49, S. V. Afanasev *et al.*, *New results from NA49*, Nucl. Phys. **A698**, 104 (2002).

Acknowledgements

I thank Prof. Norbert Schmitz for giving me the opportunity to work in the Munich group of the STAR experiment in its final years in the collaboration and for supervising my thesis. Volker Eckardt and Peter Seyboth offered guidance in both the hardware-oriented and the analysis phases of my thesis work. I owe thanks to Janet Seyboth for her invaluable assistance with the STAR computing framework, and without Jörn Putschke and Markus Oldenburg the FTPCs would still be uncalibrated.

While many people in STAR made my participation in the experiment a most enjoyable and beneficial experience I am particularly indebted to the Strangeness working group. Lee Barnby, Rene Bellwied, Gene van Buren, Helen Caines, Matt Lamont and Camelia Mironov supported my analysis and engaged me in many fruitful email discussions. I am indebted to Eric Hjort for his help with the testing of the FTPC embedding framework and for producing the necessary data for my efficiency corrections. Special mention goes as well to Alexei Lebedev on whose expertise with hardware-related FTPC issues I could always rely; he has now assumed responsibility for the detectors. Outside STAR, I thank Lie-Wen Chen, Che-Ming Ko, Vasile Topor-Pop and Klaus Werner for providing me with model programs and results. Finally, I'm grateful to Angelika Drees for her explanations of the inner workings of RHIC.